ULTIMATE
Instrument Concept
and
Prototyping Plan
(December 2015)

REVISION 1

Simon Ellis

Ross Zhelem, David Brown, Nick Staszak,

Chris Lidman, David M. Nataf, Andrew R. Casey

Pascal Xavier, Andrew Sheinis, Peter Gillingham, Julia Tims,

Jon Lawrence, Julia Bryant, Rob Sharp

Rev. No.	Author	Approved for Issue		
		Name	**Signature**	**Date**
1	Simon Ellis	Andrew Sheinis		11 December 2015

ACRONYMS

AAO	Australian Astronomical Observatory
AAT	Anglo-Australian Telescope
GLAO	Ground layer adaptive optics
FRD	Focal ratio degradation
IFU	Integral field unit
PV	Peak-to-valley
WFC	Wide field corrector

REFERENCE DOCUMENTS

	Allen, J. et al. 2015, MNRAS, 451, 2780
	Allen, J. et al. 2015, MNRAS, 446, 1567
	Bloom et al. 2015, submitted to MNRAS
	Brown, A.G.A. 2014, EAS Publications Series, 67, 307
	Bryant, J. et al. 2015, 447, 2857
	Croom, S. et al. 2012, MNRAS, 421, 872
	De Silva, G. M., Freeman, K.~C., Bland-Hawthorn, J., et al. 2015, MNRAS, 449, 2604
	Epstein, C.R., Elsworth, Y.~P., Johnson, J.~A., et al. 2014, ApJL, 785, L28
	Ho et al., 2015, submitted to MNRAS
	Gonzalez, O.~A., Rejkuba, M., Zoccali, M., et al. 2012, A&A, 543, A13
	Gilmore, G., Randich, S., Asplund, M., et al. 2012, The Messenger, 147, 25
	Gould, A., Huber, D., Penny, M., & Stello, D. 2015, Journal of Korean Astronomical Society, 48, 93
	Henderson, C.B., Gaudi, B.S., Han, C., et al. 2014, ApJ, 794, 52
	Kewley, L. et al. 2004, ApJ, 127, 2002
	Kewley, L. et al. 2013, ApJL, 774, 10
	Kim, S.-L., Park, B.-G., Lee, C.-U., et al. 2010, Proc. SPIE, 7733, 77333F
	Kunder, A., Koch, A., Rich, R.~M., et al. 2012, AJ, 143, 57

	LSST Science Collaboration, Abell, P.A., Allison, J., et al. 2009, arXiv:0912.0201
	Nataf, D.M., Gonzalez, O.A., Casagrande, L., et al. 2015, arXiv:1510.01321
	Ness, M., Freeman, K., Athanassoula, E., et al. 2012, ApJ, 756, 22
	Nishiyama, S., Nagata, T., Tamura, M., et al. 2008, ApJ, 680, 1174
	Perryman, M.A.C. 2005, Astrometry in the Age of the Next Generation of Large Telescopes, 338, 3
	Portail, M., Wegg, C., Gerhard, O., & Martinez-Valpuesta, I. 2015, MNRAS, 448, 713
	Schönrich, R., & Binney, J. 2009 MNRAS, 396, 203
	Sharp, R. et al. 2015, MNRAS, 446, 1551
	Silva Aguirre, V., Davies, G.R., Basu, S., et al. 2015, MNRAS, 452, 2127
	Spergel, D., Gehrels, N., Baltay, C., et al. 2015, arXiv:1503.03757
	Thompson, T.A. 2013, MNRAS, 431, 63
	Wisnioski et al. 2014, ApJ, 799, 209
	Yuan, T.-T. et al. 2013, ApJ, 767, 106
	Zasowski, G., Johnson, J.A., Frinchaboy, P.~M., et al. 2013, AJ, 146, 81

1 EXECUTIVE SUMMARY

This document presents the Stage 1 proposal for the Ultimate Instrument for Subaru. The instrument represents a phased approach to developing a NIR Multi-IFU capability for the Cassegrain focus of Subaru fed by the new Ultimate GLAO system. This first phase is a method to provide high-efficiency, moderate resolution multi-IFU capability in the J, H and possibly K bands using the existing and recently upgraded NuMOIRCS spectrograph.

The instrument consists of a fibre positioner based on the AAO-developed Starbugs technology (also being developed for the GMT). The positioner will position a complement of 8-13 individual IFU systems each of which contains 61 spaxels subtending 0.15 arcseconds on the sky. The total filed coverage will be 1.2 arcseconds per IFU. The fibre positioner will feed the upgraded NuMOIRCS system at an R=500-3000. During this stage we will evaluate the efficacy of feeding the PFS spectrographs as well.

In the document we present two science cases that have the possibility of acquiring high-impact data both before and after GLAO comes online, i.e. both with the seeing-limited and AO-corrected imaging of Subaru. The first science case expands on the very successful SAMI survey at the AAT. This first science case will allow us to better understand galaxy evolution: feedback and gas-infall a well as the role of environment by complementing the visible, low-redshift (z=0.05), SAMI survey with a similar extra-galactic dataset from Subaru in the NIR at redshifts z=0.5, 1.0 and 1.5. The instrument will be designed such that the spaxel size on the sky and FOV are similar between the two surveys and it will be faster with smaller spaxel size than its nearest competitor, VMOS on the VLT. The second science case will be a NIR stellar survey whose goal is to map the dark matter distribution of the Milky Way for the inner 2 Kpc. By combining parallaxes and proper motions from WFIRST with radial velocities from Ultimate this survey will lead to a deeper understanding of the history and evolution of our own galaxy.

The proposal for this stage is to develop the conceptual design and detailed instrument cost and schedule for the ULTIMATE/NuMOIRCS instrument. In addition, this stage will retire the most difficult technical risks by prototyping the high-risk components of the instrument and producing on-sky testing of the critical components. These high-risk items are:

a) The new larger starbug required for Ultimate, which will be prototyped and tested in the AAO labs.

b) The NIR IFU, foreoptics and fiber system for J and H band compatible fibres, to be built up and tested in the AAO Labs, then at the AAT and/or Subaru.

c) The K-band compatible ZBLAN fibre, which will be tested for throughput, FRD and noise characteristics at various temperatures in the lab.

The deliverable at the end of this stage is a completed CoDR report containing cost and schedule information for the next stage, test results and data from the prototype testing

and all design and modeling information produced as part of the Conceptual Design stage.

2 SCIENCE CASE

2.1 Science Case A - Galaxy evolution

Galaxy evolution is an unsolved problem in astrophysics. Many of the processes that are thought to sculpt galaxies into the forms that we see today, e.g., feedback, gas infall, and the role of the environment, are not well understood theoretically, and are poorly constrained observationally. Nevertheless, there are reasons to believe that we can make progress over the next decade.

Over the last few years, there has been an enormous increase in the volume, quality and complexity of observational data. At the same time, computer simulations of galaxies have become larger (more particles and better resolution) and more sophisticated (better treatment of the processes that cannot yet be tackled through direct simulation). We have learned a lot about galaxy evolution by comparing galaxy simulations with observations and vice-versa.

As computer simulations become larger, more sophisticated and more detailed in their predictions, it is becoming clear that observations also need to become more detailed. Currently, the largest spectroscopic surveys (SDSS, for example) are biased: they only measure the integrated properties of galaxies, and due to the finite size of the fibres used in such surveys, only the central part of the galaxy is measured. Observations are therefore incomplete, which leads to a restricted and perhaps misleading understanding of how galaxies evolve.

In the local universe, these limitations are now being tackled through multi-object IFU surveys, such as MaNGA and SAMI, that resolve the gas and stellar populations across each galaxy. This has led to a flood of new results, some of which are discussed below. In the distant universe, where galaxies are much younger, progress is much slower, because existing instruments either lack the spatial resolution (KMOS/VLT) to match what can be done in the local universe, or can only target one object at a time (SINFONI/VLT, MUSE/VLT, OSIRIS/Keck). ULTIMATE is an instrument that overcomes both of these limitations.

Here, we describe the ULTIMATE galaxy survey, which will target galaxies that are between 6 and 9 billion years younger than the galaxies we see today. At these early times, the Universe itself was between 4 and 7 billion years old. The ULTIMATE galaxy survey will provide a detailed view of large numbers of galaxies that is only currently possible for galaxies in the local Universe through surveys like SAMI. The ULTIMATE galaxy survey will enable us to understand how these distant cousins evolved to become the galaxies that we see today.

We start with a description of the SAMI survey, and then examine what an instrument like ULTIMATE will enable us to do in the field of galaxy evolution. In preparing this case, we have assumed that some of the IFUs will feed nuMOIRCS, However it is also

possible to feed the planned Prime Focus Spectrograph (PFS, see Appendix B), or a new near-IR spectrograph, using the same technology. Science cases using both nuMOIRCS and PFS are discussed. We have also assumed that the ground-layer adaptive optics (GLAO) system will be operational. We have not assumed that K band fibres will be available (see section 4.4.1.1); however, we note that incorporating them into ULTIMATE would enable some of the studies described in the document to be extended up to galaxies that are 11 billion years younger than today, which is only 2 billion years after the big bang.

2.1.1 The SAMI survey

The SAMI Galaxy Survey (Croom et al. 2012, Bryant et al. 2015) is collecting integral field spectroscopy on a sample of 3,400 local galaxies over a range of stellar masses and a wide range of environments, from the field to dense cores of rich galaxy clusters. The survey started in March 2013, and has observed over 1,200 galaxies to date. The median redshift of the SAMI survey is z=0.05.

The SAMI survey uses the SAMI instrument, a multi-object IFU at the prime focus of the AAT. The characteristics of the instrument are listed in Table 1. SAMI feeds the AAOmega spectrograph, which consists of two arms (red and blue) split by a dichroic, and variety of VPH gratings that allow coverage of the entire 370-880nm wavelength range at low resolution, or smaller wavelength ranges at higher resolution. The SAMI survey uses a low resolution grating (R=1,700) in the blue arm and higher resolution grating (R=4,500) covering H-alpha, [NII] and [SII] in the red-arm.

In Table 1, we list the angular coverage of the SAMI IFUs and compare it to the angular coverage of the IFUs that are planned for ULTIMATE. We note that the physical area covered by the IFUs of ULTIMATE at z~0.5 is smaller than that of SAMI at z~0.05.

Table 1. A comparison between the physical characteristics of the IFUs used by SAMI and the IFUs that are currently planned for ULTIMATE. For selected redshifts, angular scales are converted to spatial scales in the second table

	Spaxel	Number of Spaxels	FoV	Number of IFUs	Patrol Field	Minimum separation	Spectral Resolution
SAMI	1.6"	61	15"	13	1 degree diameter	30"	1,700 (blue) and 4,500 (red)
ULTIMATE	0.15"	61	1.2"	7-13	14'x8'	25"	3,000 to 5,000

Survey	Spaxel (1.6" vs 0.15")	FoV (15" vs 1.35")
SAMI @ z=0.05	1.56 kpc	14.7 kpc
ULTIMATE @ z=0.5	0.92 kpc	8.2 kpc
ULTIMATE @ z=1.0	1.20 kpc	10.8 kpc
ULTIMATE @ z=1.5	1.27 kpc	11.4 kpc

In Figure 1, we show the spectral coverage of the SAMI survey and compare it to the spectral coverage that would be provided by ULTIMATE. In this plot, we have used the grisms that are currently available with MOIRCS, and have assumed that the PFS spectrograph can be fed by the fibres of ULTIMATE. It should be noted that PFS could cover all the main diagnostic lines up to z~0.8. It would be the instrument of choice for a SAMI-like survey at z~0.5. Covering all the lines at higher redshifts would require the targets to be observed with both PFS and nuMOIRCS separately.
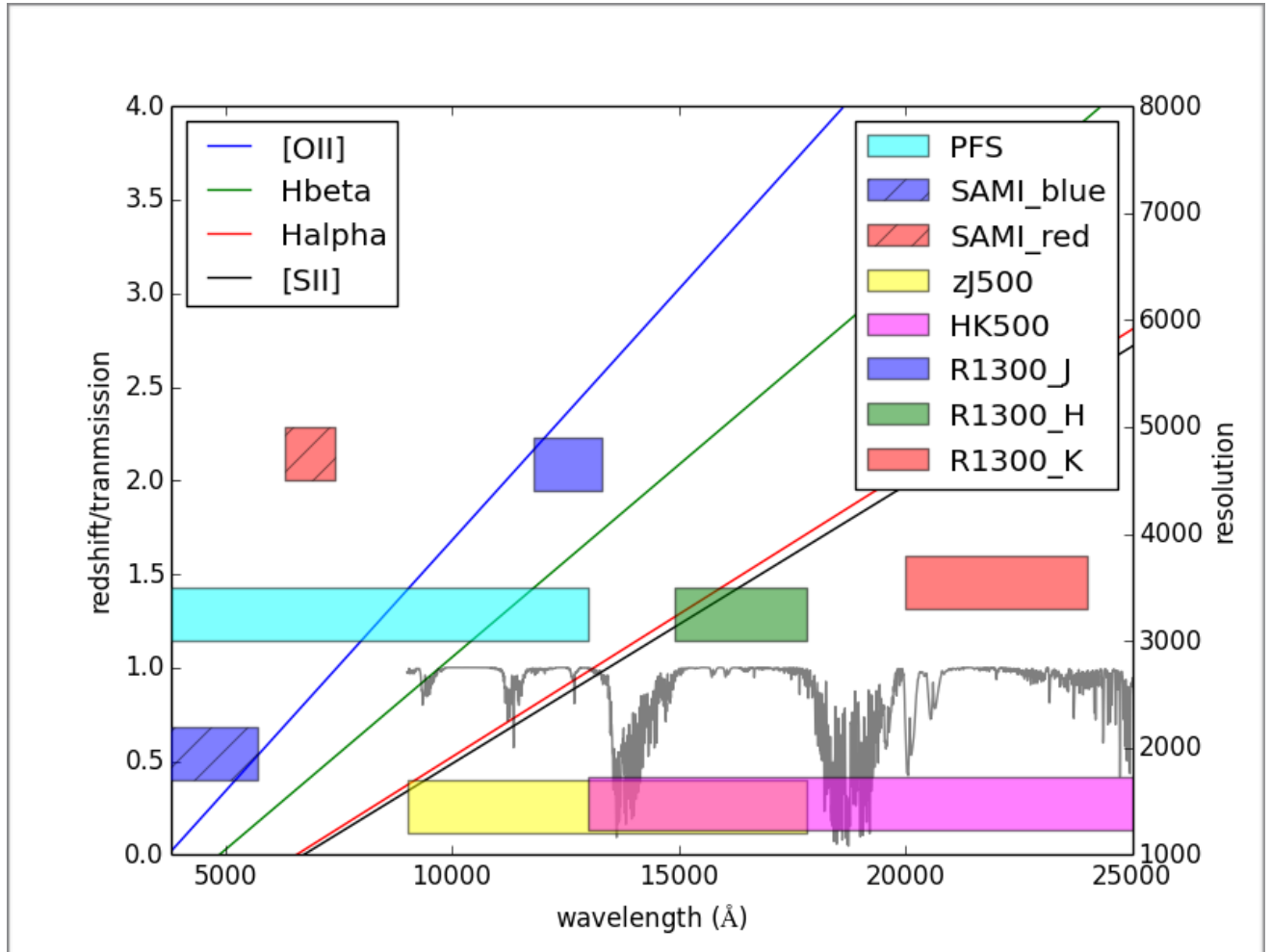
Figure 1. The spectral coverage of SAMI (cross hatched region) and ULTIMATE as a function of resolution (right hand axis). Also shown is the transmission spectrum of the Earth's atmosphere (grey line) and wavelength of several key emission lines as a function of redshift. The resolution that is shown for PFS is the resolution for PFS fibres, which are 138 micron in diameter. The ULTIMATE fibres are almost four times smaller. Assuming that PSF of PFS is two pixels, the resolution using the ULTIMATE fibres will be about a factor of two higher than shown here.

2.1.2   The ULTIMATE galaxy survey

The ULTIMATE galaxy survey will observe 3,000 galaxies, spread over three redshifts (z=0.6, 0.9 and 1.4) corresponding to look-back times of 6, 7 and 9 billion years. The number of galaxies has been chosen to match the number of galaxies in the SAMI survey, which has been designed to build statistically significant samples that cover a range of masses and environments. Assuming, that one can observe 13 objects at a time and that exposure times will be of the order of 2 hours, the entire survey will take of the order of 50 nights. If one can double the number of IFUs then the survey would take half this time or one would be able to double the number of objects.

Targets will be selected from the COSMOS and SXDF-UDS fields, each of which covers 1 sq. deg. Both fields are within the HSC Ultra-deep survey region. Likely target densities are discussed later. We now focus on science that will be done with the ULTIMATE galaxy survey.

We structure the scientific justification for the ULTIMATE galaxy survey as a series of questions. We limit the questions to the ones that can be answered by studying emission lines. With an 8-m class telescope, measuring absorption line strengths and widths will only be possible for the brightest sources at the lowest redshifts. Studying large numbers of such galaxies at high redshifts will need to wait for AO-fed IFU spectrographs on 30-m class telescopes.

In addition to spatial resolution, wavelength coverage and spectral resolution are important considerations. Some studies (for example, measuring the kinematics of the gas, or examining where star-formation has been quenched) can be done with just a single line, and do not need high spectral resolution. Other studies (e.g., identifying shocked regions) need broad wavelength coverage in order to cover multiple lines and high spectral resolution to properly model the board and narrow components.

2.1.2.1 How does feedback work and how does it change with cosmic time?

The shape of the galaxy stellar mass function is very different to the shape of the halo mass function. Galaxies at both low and high stellar mass are much less common than what one would infer by scaling the halo mass function to match the density of galaxies at intermediate stellar masses. In order to explain the deficit at both ends of the stellar mass function, semi-analytic models of galaxy evolution invoke a number of mechanisms (generally termed feedback) that expel gas from a galaxy or prevent the gas that is in the galaxy or its halo from forming into stars. In high-mass galaxies, AGN are thought to be the engine driving the feedback. In low-mass galaxies, the feedback is thought it be driven by supernovae and/or star formation.

At z=1, AGN were 100 times more common than they are today, and the amount of star formation (and hence the number of supernovae) was an order of magnitude higher. Galaxies were also less massive. In short, one would expect feedback to be much more common and efficient at z=1 than it is now. Hence feedback must have played an important role (perhaps the central role) in providing the galaxies that we see today.

While semi-analytic models of galaxy evolution have successfully used feedback mechanisms to explain the global statistical properties of the galaxy population, there is a need to verify that these mechanisms actually work in the way that they are implemented in the semi-analytic models.

Understanding the importance of AGN or supernova driven feedback, how they work, and how the relative importance of the two mechanisms evolves with time requires one to separate both, and this requires good spatial resolution (of the order of 1-2 kpc), good spectral resolution (of the order of a few thousand) and broad wavelength coverage (to enable coverage of the major diagnostic lines). An example of a galaxy with a strong feedback is show in the figure below. These data were taken with SAMI.

ULTIMATE is the ideal instrument to extend these studies to higher redshifts. At z=1.0, 1 kpc corresponds ~0.12 arc-seconds on the sky, and galaxies are around an arc-second in size. At this redshift, H-alpha is shifted to the end of the J-band, and [OII] is in the R-band. This study would make use of both PFS and nuMOIRCS.
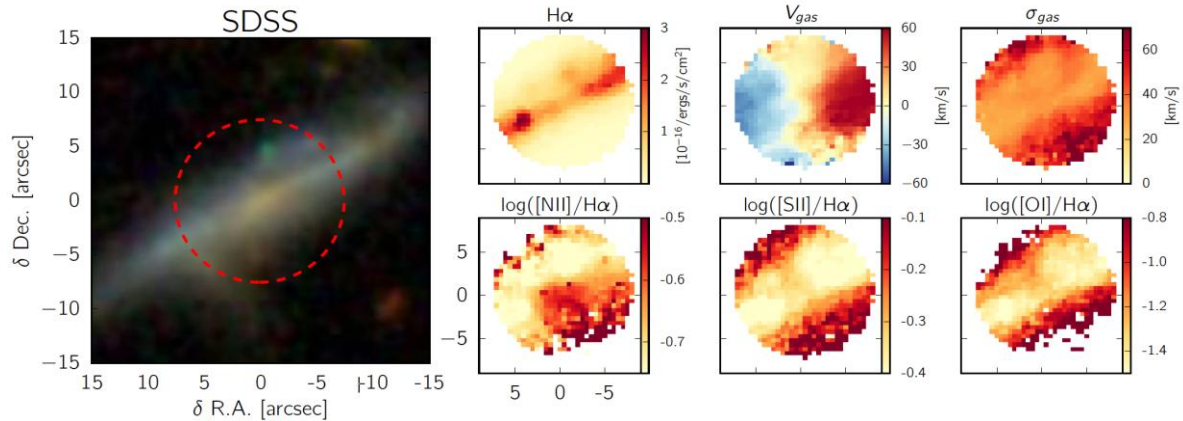
Figure 2. SAMI observations of an edge-on disk galaxy. An SDSS image of the galaxy is shown on the left. The dashed red circle corresponds to the SAMI FoV. Results from the SAMI observations are shown on the right. In the top row, the intensity of H-alpha emission, and the velocity and velocity dispersion of the H-alpha-emitting gas are plotted. Note the twisted rotation curve and the increasing size of the velocity dispersion as one moves away from the disk. Note also the change in line ratios in the bottom row. Both are indicative of a turbulent outflow of material that is, in this case, being driven by star formation in the disk of the galaxy. Figure taken from Ho et al. 2015.

2.1.2.2 What causes quenching in dense environments?

In the local universe, dense environments (such as rich groups and clusters) are dominated by early-type galaxies that are no longer forming stars. Before falling into these environments, these galaxies would have been forming stars as vigorously as galaxies in the field. Hence, at some point in time, probably soon after these galaxies entered the cluster for the first time, star formation in these galaxies was quenched.

Numerous quenching mechanisms are possible in the cluster environment. Ram pressure stripping of gas from the galaxy as it passes through the hot intra cluster medium is one mechanism. Another is the disruption of the supply of pristine gas from

the galaxy halo (strangulation). Galaxy mergers, which could lead to rapid consumption of the gas reservoir and possibly to AGN activity, which can further inhibit star formation, is another.

All of these mechanisms leave specific signatures. For example, ram pressure stripping might be detectable as a decrease in the star formation rate in the outer parts of a disk galaxy (see Figure 3), or as star formation in material that is swept away from the galaxy. Both signatures have been detected in galaxies at low redshift, for example, the anaemic spirals in Virgo and the jellyfish-shaped galaxies in several Abell clusters. At higher redshifts, where clusters are smaller, dynamical timescales are shorter, and the intra-cluster medium is less developed, other factors may be at play. Given that the angular size of these signatures will typically be smaller than the seeing disk, these studies have to be done from space, or from the ground with an AO fed system such as ULTIMATE.

This study would make use of PFS up to z~0.8 and nuMOIRS at higher redshifts. At z~1.7, H-alpha reaches the end H-band. At this redshift, galaxy clusters are in a very active phase, and there are now many examples of galaxies in the cores of these clusters with strong H-alpha, presumably because they are vigorously forming stars. If K-band fibres became available, these studies could be extended to higher redshifts.
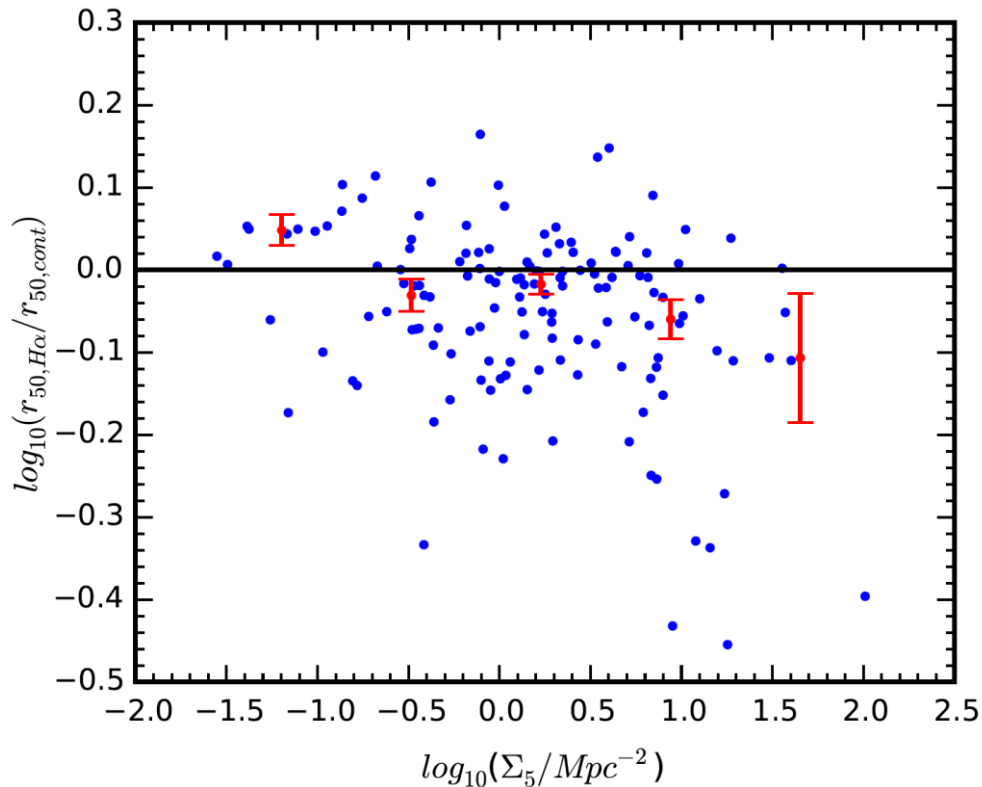
Figure 3. The relative size of the H-alpha emitting region against size of the continuum emitting region plotted against density. Note the progressive decrease in the ratio with increasing galaxy density. The data are from the SAMI survey and the plot has been taken from Schaefer et al. 2015, in prep.

### 2.1.2.3 How does gas accretion change with time?

In current theories of galaxy evolution, it is thought that galaxies are continuously fed by in-falling streams of pristine gas. Without this supply, most galaxies, like our own Milky Way, would have already stopped forming stars. This gas is difficult to observe as it is cold and tenuous. Hence, there are almost no observational constraints on this key theoretical idea.

A handle on the how gas accretion works can be gained from metallicity gradients. According to the inside-out theory of disk formation, we expect higher metallicity gas to be in the centre of disks, as there has been more time for enrichment there. When pristine gas from the IGM accretes on to a galaxy or enriched gas is pushed outwards, this can flatten metallicity gradients.

Though metallicity gradients have been well characterised at low-redshift, it has been difficult to extend these studies to higher redshifts, because low spatial resolution has the effect of flattening gradients, even if they are steep (Yuan et al. 2013). The GLAO correction of ULTIMATE is key for providing the needed spatial resolution to study this tracer of gas flows at these redshifts.

As shown in Kewley et al. (2013), the gas-phase metallicity (and the hardness of the ionising photons) can be determined from the location of objects on the Baldwin-Phillips-Terlevich (BPT) diagram (see Fig. 4), which uses [OIII] 4959,5007, H-beta, H-alpha and [NII] 6583. At z=0.6, [OIII] 4959,5007, H-beta and [OIII] land in the i band, whereas H-alpha and [NII] 6583 land in the near-IR Y band, which means that both PFS and nu-MOIRCS would be required. At higher redshifts, e.g., z=1.4, all four lines would land in the near-IR J and H bands.

Adequate spatial resolution is crucial to these studies. Even with the spatial resolution provide by ULTIMATE, it may be necessary to study galaxies that are strongly lensed by massive clusters if one is to reach a spatial resolution of 500 pc, which is the resolution needed to resolve the most massive star forming regions in high-redshift galaxies. The multiplex advantage of ULTIMATE, means that several lensed galaxies behind a single lensing cluster can be studied simultaneously.
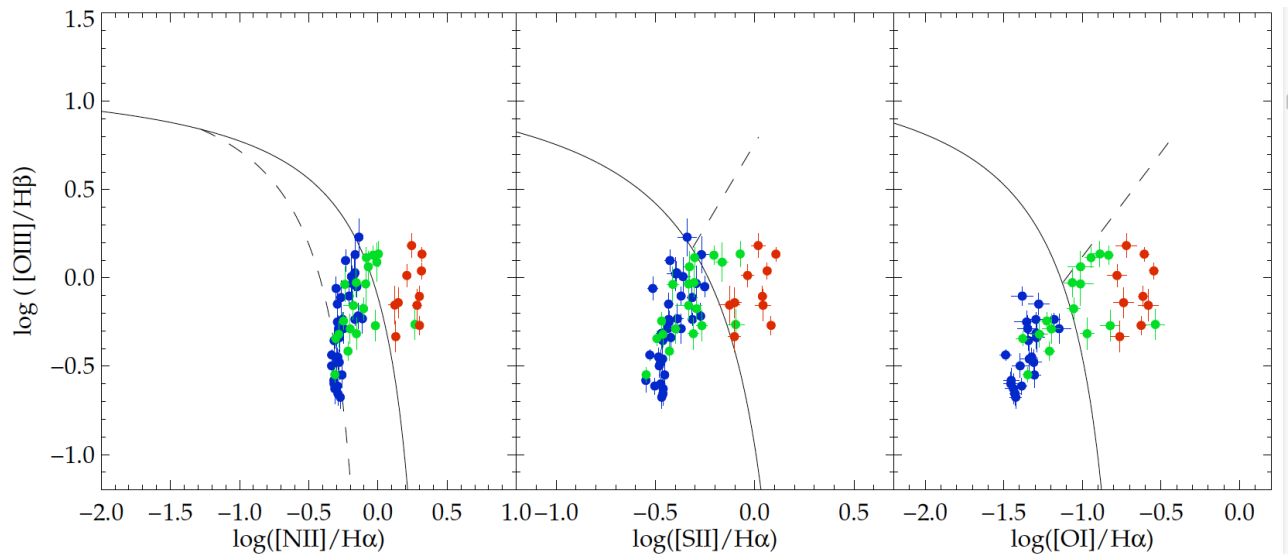
Figure 4. The location of the line emitting components of a single SAMI galaxy in the BPT and other similar diagnostic diagrams. The continuous and broken lines split objects according to the source of ionising photons, e.g. star formation, AGN and shocks. ULTIMATE provides the necessary spatial and spectral resolution to isolate these three components. The plot was taken from Leslie et al. (in preparation).

2.1.2.4 What drives galaxy transformations?

As galaxies become older, they transform from star-forming to passive, disk to spheroid, and blue to red. Much of this transformation occurs between z=1 and today, so the best place to study this transformation is in this redshift interval, a redshift interval that is accessible to ULTIMATE.

What are the main drivers of this transformation? As noted earlier, environment has an impact, but the impact of the environment is most keenly felt at low stellar masses. At higher stellar masses, galaxies have already transformed themselves before they become a satellite in a more massive halo.

In addition to environment and stellar mass, other factors may be at play, such as the accretion history, the stability of disks, the mass of the halo, and whether not the galaxy in question is a satellite or a central.

Some of these factors work on the scales of 1-2 kpc. For example, the presence of kinematic instabilities can only be inferred by examining the kinematics of galaxies with a resolution approaching 1 kpc, which at z=1, subtends an angle 0.12 arc-seconds. An example of how the kinematics of the gas is correlated with the location of star formation in nearby galaxies is show in Figure 5. This study was done with SAMI. Extending these study to z=1, will require ULTIMATE.
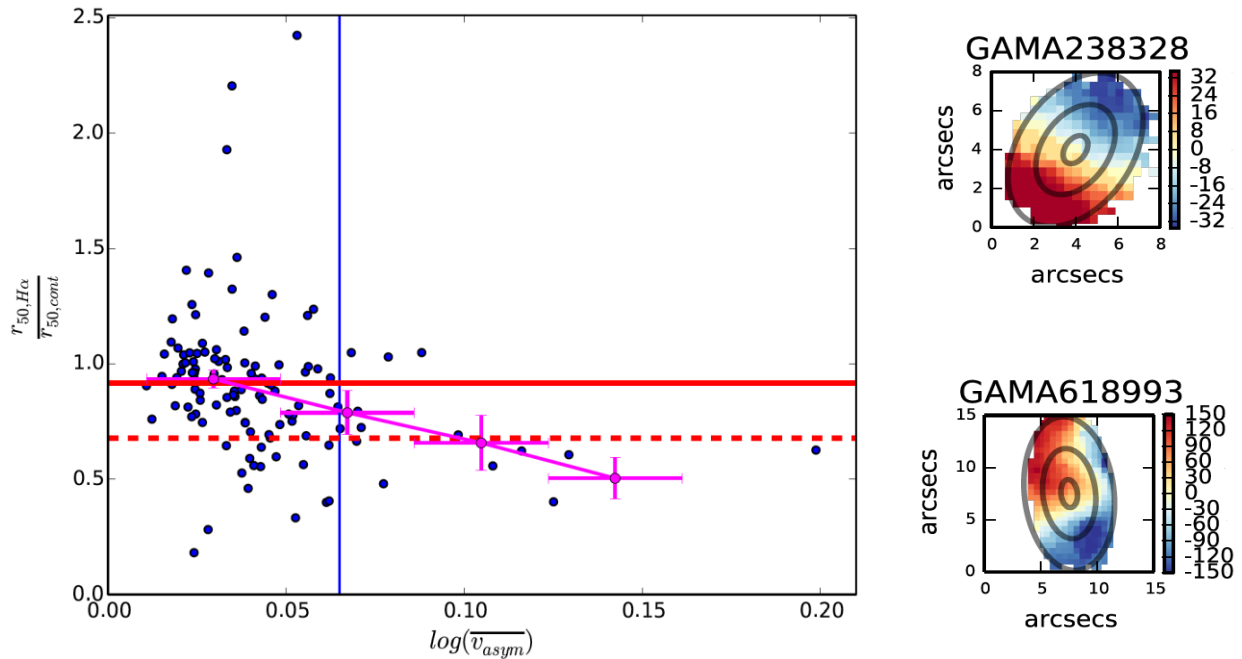
Figure 5. On the left, the concentration of star formation relative to the continuum versus the asymmetry in the gas kinematics. On the right, examples of SAMI galaxies, one with symmetric velocity contours and another with asymmetric contours. As can be seen in the plot, star formation becomes more concentrated as the gas in the galaxy becomes more disturbed.The data are from the SAMI survey and the plots have been taken from Bloom et al. 2015.

2.2 Science Case B - Dark Matter in the Inner 2 Kiloparsecs of the Milky Way

The question of the Milky Way's dark matter potential is evolving from one of speculation and order-of-magnitude estimates to being that of a precision science. As is well-known, LSST will study the gravitational potential at large distances, and Gaia at the scale of the solar neighbourhood. Closer to the inner Milky Way, a 4% measurement of the enclosed baryonic+dark mass has recently been achieved by modelling large-scale conventional radial velocity survey data along with spatial density data from photometric surveys. The degeneracy between baryonic mass and dark matter mass will not be an issue due to efforts currently underway to precisely measure the IMF.

We propose to complete the mapping of the dark matter potential from R_{GC} = 2.0 kpc down to R_{GC} = 0.1 kpc, by combining parallaxes and proper motions from the upcoming WFIRST Galactic bulge microlensing campaign with radial velocities from ULTIMATE. Under the assumption of 13 fibres per pointing, we will require ~400 hours of observing time (50 nights) to obtain spectra of 10,000 stars.

We discuss how this effort requires a large aperture telescope, infrared spectroscopy, and low seeing. A byproduct of this campaign will be an accurate star-formation history of the Milky Way as a function of Galactocentric radius, all the way to the inner bulge.

2.2.1 Introduction

The current state-of-the-art in spectroscopic surveys of the Milky Way galaxy are unquestionably the Gaia-ESO survey (Gilmore et al., 2012), the Apache Point Observatory Galactic Evolution Experiment (APOGEE; Zasowski et al., 2013), and the Galactic Archaeology with HERMES (GALAH; De Silva et al., 2015) survey.

These three surveys will yield a combined assay of millions of stellar spectra, each with informative diagnostics such as the relative abundances for up to ~30 elements as well as 10% distance estimates and 20% age estimates. The result of these surveys will provide unparalleled characterization of the solar neighbourhood, i.e. the Galactic disk within ~ 2 kpc of the Sun.

There will, in contrast, be relatively scant mapping of the inner Milky Way and the outer halo, and zero study of the disk at the other side of the Galaxy, and the inner regions of star clusters and dwarf galaxies. These archaeologically pertinent stellar populations are more challenging to study because they are more distant, more crowded, and in many cases more extincted.

Fortuitously, the general specifications of ULTIMATE for Subaru are exactly what one needs to target these populations for spectroscopic follow-up. The larger mirror aperture increases the signal of more distant (and thus fainter) targets, whereas the smaller seeing decreases the sky noise that currently limits infrared spectroscopy. The smaller seeing and smaller fibres enables targeting of stars in crowded fields, typical of the inner Milky Way and the cores of globular clusters and dwarf galaxies. Finally, the infrared aspect reduces the impact of dust by a factor of ~5-15 depending on the specifics of the region studied.

The Gaia-ESO and GALAH surveys fail in each of these three criteria, which is why their survey yields will be completely orthogonal and complementary to what we can learn from an ULTIMATE survey of the Galaxy. APOGEE does benefit from infrared imagine, and thus has a more significant Galactic plane component. However, the large fibre size (~2") of the APOGEE spectrograph, and the small aperture of its telescope (~2.5m) limit APOGEE to stars brighter[1] than H ≈ 12.5, rendering most of the Galactic bar, the inner Galactic bar, and the disk at the other side of the Galaxy out of reach. The large fibres also means it cannot target crowded fields, compounding the previous limitation.

Throughout this text, we assume the following specifications for ULTIMATE:

- Fibres with 0.5" diameters;
- Seeing of 0.4";
- An 8.2 meter mirror aperture;
- Low-resolution spectroscopy over the JHK range;

Low resolution spectra (~ 2000) in the JHK bands is sufficient for a robust determination of radial velocity, stellar effective temperature, surface gravity, and mean abundance. Given the large aperture and narrow fibre size, low- resolution infrared spectra with ULTIMATE will facilitate high-impact galactic astrophysics that would be otherwise unachievable.

2.2.2 Spectroscopy of the WFIRST Field

2.2.2.1 Description of WFIRST

The Wide-Field Infrared Space Telescope (WFIRST) is a ~2.5 billion dollar NASA mission scheduled to launch in 2024 (Spergel et al., 2015). As part of its core mission, WFIRST will spend 357 days observing 10 contiguous fields toward the bulge spanning a total surface area of 2.81 deg^2.

The primary purpose of this bulge component will be the discovery and characterization of ~3,000 planets for planet-star separations greater than 1 AU, extending all the way to free-floating planets, and thus completing the mapping of the ``planet function'' begun by Kepler.

---

[1] All apparent magnitudes discussed in this document are in the Vega magnitude system.

The observing seasons are expected to be 72 days each, one per year over six years. During that period, each field will be observed every 15 minutes, with 24/7 cadence during that time span. This yields a total of ~35,000 photometric measurements.

In the following subsections, we briefly discuss why the spectroscopic follow-up of the WFIRST window needs to be done in the infrared, at low seeing (and large aperture), and then follow with the case for follow-up.

2.2.2.2 Why WFIRST Spectroscopic Follow-up Needs to be in the Infrared

The typical extinction toward the field is $A_V \approx 6.5$, reaching values as high as $A_V \approx 22$ (Gonzalez et al., 2012; Nishiyama et al., 2008). In contrast, the extinction toward those sightlines are typically ~ 5× smaller in J-band, ~ 9× smaller in H-band, and ~ 16× smaller in K-band (Nishiyama et al., 2008; Nataf et al., 2015). Thus, proper spectroscopic follow-up of these fields require infrared spectroscopy.

2.2.2.3 Why WFIRST Spectroscopic Follow-up Needs to be From Large Aperture}

In Figure 1, we show the predicted the distance distribution of stars toward the WFIRST field using the same colour selection as APOGEE does toward the bulge (Zasowski et al., 2013), accounting for the extinction toward this field (Gonzalez et al., 2012), and assuming a simple Galactic model (Ness et al., 2012). We place the Galactic centre at a distance of $R_0 = 8.33$ Kpc.
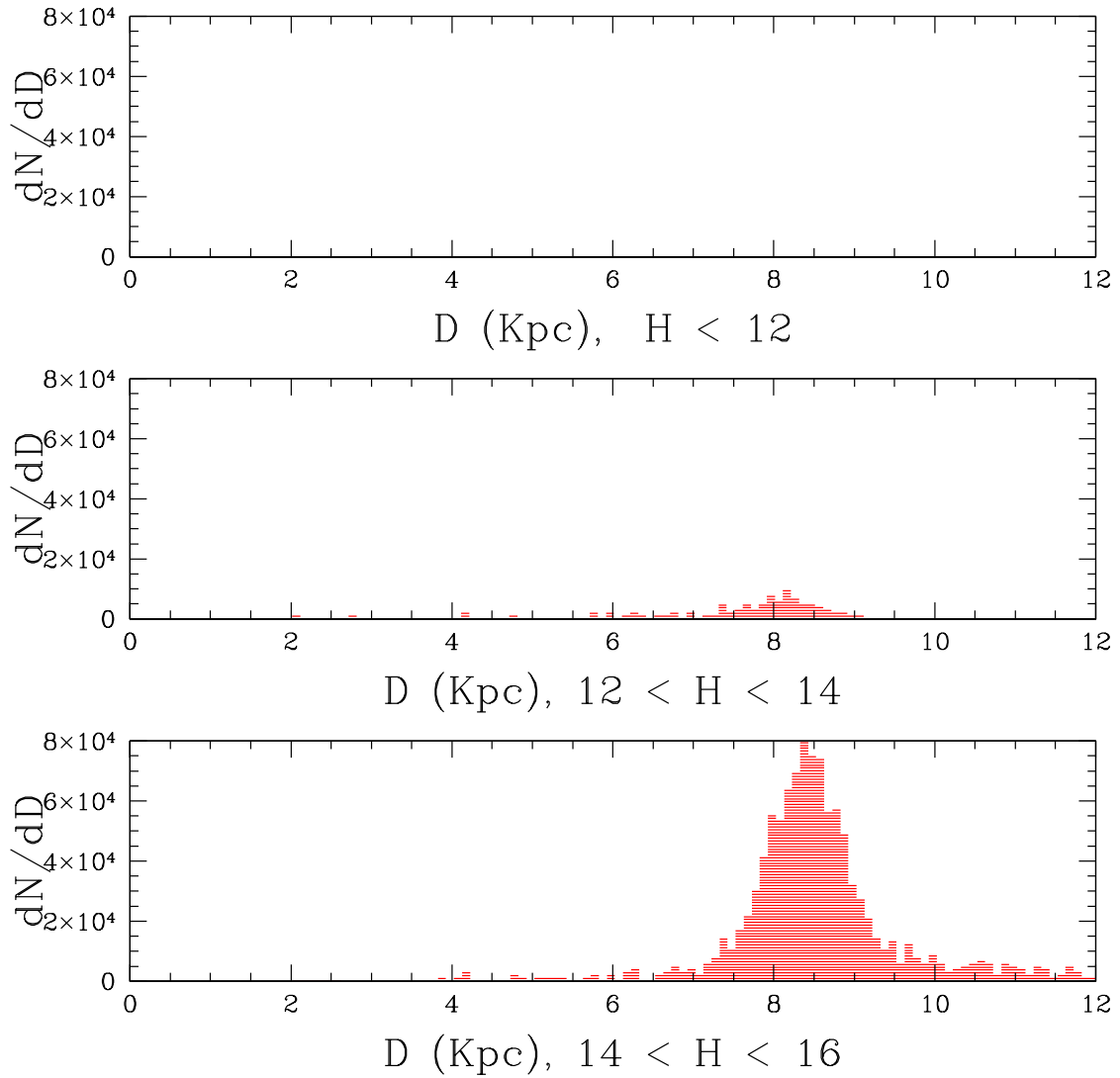
Figure 6. Predicted distance modulus toward the WFIRST field as a function of apparent magnitude cut in *H*-band. More stars are available at fainter magnitudes, and they span a broader distribution in Galactocentric radii.

If one selects stars $H \leq 12$, there are so few stars that upon setting the histogram scale to be the same for all three panels, it appears as zero stars. The mean distance to the stars is 2.7 kpc, in other words the sample does not even reach the inner Milky Way. If one selects stars satisfying $12 \leq H \leq 14$, the sample expands to a tolerable size, but the mean dstance is 7.5 kpc, it remains biased to nearby stars. Finally, for a sample of stars satisfying $14 \leq H \leq 16$, the mean distance probed is 8.6 kpc, with a mode closer to 8.4 kpc. In other words, stars on both sides of the Galactic centre probed, including the interesting stars in the Galactic disk at the other side of the Galaxy, a region now totally unprobed. Thus, to have a sample of stars symmetric about the Galactic centre, and large, we will need to target stars ~ 25× fainter than those currently targeted by APOGEE. The ULTIMATE instrument will benefit from a telescope surface area that is ~ 12× larger, recovering most of the offset so as to conserve exposure times. Further,

the PSF will have a surface area ~ 4x smaller at least, and thus signal-to-noise in the infrared should rise by a factor of ~50 for equal exposure times, or be conserved for exposure time cut by one half.

At 36 stars per configuration, this works out to 72 stars per hour of observing. One can thus acquire 10,000 bulge stars in ~140 hours of observations, equivalent to 21 nights. This would put the sample on par with ARGOS (Ness et al., 2012) and BRAVA (Kunder et al., 2012) in numbers, but with the benefit of accurate and precise parallaxes, and thus superior diagnostic power.

2.2.2.4 Why WFIRST Spectroscopic Follow-up Needs to be at Sharp Seeing

We state two reasons for the sharp seeing requirement.

The first, already alluded to in the previous paragraph, is that it decreases sky noise, and thus allows shorter exposure times at fixed signal-to-noise requirements.

The second, is that the many of the most interesting fields not targeted by Gaia-ESO, APOGEE, and GALAH are crowded fields. This includes the inner Galactic bulge discussed in this work, but also the Galactic disk, and the inner regions of globular clusters and dwarf galaxies.

2.2.2.5 The Case for Spectroscopic Follow-Up of WFIRST I: The Milky Way's Dark Matter Profile

The stellar populations in the WFIRST Galactic bulge fields will have a wealth of information including parallax, proper motion, colour, and sometimes asteroseismic mass and gravity.

For stars brighter than $H = 19$, the expected precision on parallaxes will be greater than 10%, in addition to an expected precision of 0.3% or better in the proper motions (Gould et al., 2015; Spergel et al., 2015). This means five dimensions of kinematics for a huge sample of stars densely spanning the Galactocentric distance range $0.1 \leq R_{GC} \leq 4.0$ Kpc. The missing kinematic component is radial velocity, which can easily be measured with spectra.

Radial velocities (Kunder et al., 2012) and directions – without proper motions and parallaxes – have already yielded a ~4% measurement of the mass content of the Galactic bulge within a rectangular box of ($\pm 2.2 \times \pm 1.4 \times \pm 1.2$ kpc) (Portail et al., 2015). This measurement of the mass content is at relatively large distances since it is constrained by radial velocities measured at separations of 4-10 degrees from the plane, and not the 1-3 degrees from the plane of the WFIRST field. Radial velocity mapping of stars in this window will complete the gravitational potential map (and thus dark matter profile) of the Milky Way, measured by the Gaia mission (Perryman, 2005) at the galactocentric scale of the solar neighbourhood and LSST proper motions to large distances traced by halo stars (LSST Science Collaboration et al., 2009).

We note that WFIRST parallaxes will be the only means of precisely mapping the gravitational mapping of the inner Milky Way: the expected accuracy of Gaia parallaxes in this region is ~30% at best (Brown, 2014), typically worse toward regions of high

extinction. Thus, the addition of spectroscopic information (from ULTIMATE) will complete the kinematic mapping of these stars and thus also complete the mapping of the Milky Way's dark matter profile.

2.2.2.6 The Case for Spectroscopic Follow-Up of WFIRST II: The Milky Way's Star-Formation History

For the red giant stars, brighter than H = 14, WFIRST will obtain precise asteroseismic values of the masses and radii of the stars (Gould et al., 2015). It's been shown that asteroseismic masses can yield reliable age estimates for red giant stars (Silva Aguirre et al., 2015) – but only in the Kepler fields and other specialized sightlines, where there is high-cadence, high-precision, long-baseline photometry available. However, the mapping from stellar mass to stellar age is metallicity-dependent.

Spectroscopy of these stars, and thus metallicities, will not only yield the age- metallicity relation and star-formation history of bulge stars, but also the same for Galactic disk stars between the Sun and the bulge, and even on the other side of the Galactic disk. This will complement age-determinations from Gaia-ESO (Gilmore et al., 2012), APOGEE (Zasowski et al., 2013), and GALAH (De Silva et al., 2015) which are surveys of bright stars, dependent on Gaia parallaxes for precise ages, and thus will only yield robust ages in the solar neighbourhood.

Solving for the Milky Way's age-metallicity relation not just for the solar neighbourhood, but also for the full range of Galactocentric radii interior to the solar neighbourhood, could resolve the issue of radial migration (Schönrich & Binney, 2009).

2.2.2.7 The Case for Spectroscopic Follow-Up of WFIRST III: Fixing the Asteroseismic Scaling Relations

When combined with ULTIMATE spectra, the asteroseismic oscillations detected by WFIRST will be crucial for improving determinations of stellar masses and radii. While giant star masses are derivable from asteroseismic scaling relations for near-solar metallicity stars, there is theoretical and empirical evidence that suggest those scaling relations should have a metallicity dependence (Epstein et al., 2014). The full impact of any metallicity dependence is currently unknown due to the paucity of bonafide metal-poor giant stars with astero- seismic oscillations. Given the wide metallicity distribution of giant stars in the disk and bulge, obtaining ULTIMATE spectra for giant stars observed by WFIRST provides an unparallelled opportunity to understand the dependence of metallicity with asteroseismic oscillations, and unambiguously answer this outstanding problem.

2.2.3 Other Science

We have not presented the other Galactic science possibilities with ULTIMATE due to scarcity of time. We plan on developing them further down the road, as well as verifying which are the most available.

The strength of ULTIMATE remains the possibility to target crowded fields, and in a Galactic context this mostly means dark matter: the cores of globular clusters, and the cores of dwarf galaxies.

Another issue is that of exoplanets. The WFIRST microlensing window we discussed here heavily overlaps with that of the Korean Microlensing Telescope Network (Kim et al., 2010; Henderson et al., 2014), which will automatically detect thousands of transiting planets due to high precision, cadence, and base- line. These transiting planets will have different properties than those of current surveys, since they will be located in the inner Galaxy, where stars have substantially higher mean metallicities and formed in denser and higher-temperature clusters (Thompson, 2013). As these sightlines are crowded and highly extincted, a survey instrument like ULTIMATE would be ideal to measure the metallicity distribution of the host stars. This can be easily accomplished by dedicating a few fibres per field from the dark matter campaign to the transiting planet host stars.

2.2.4 Conclusion

In this preliminary science case we have outlined a fundamental astrophysics problem that a wide-aperture, infrared, and low-seeing spectrograph (such as ULTMATE) would be uniquely suited to solve: the distribution of dark matter in the inner Milky Way, in the Galactocentric distance range $0.1 \leq R_{GC} \leq 2.0$ kpc. This will complete the census that will be undertaken by Gaia at intermediate Galactocentric distance regions, and LSST at the largest distances.

2.3 Competing facilities

Here we review the capabilities of facilities, both in operation and planned, that will compete with ULTIMATE.

In Table 2, we list the current IFU facilities based on 8-10m class telescopes. It includes facilities with and without adaptive optics and facilities that have multiple IFUs or just a single one. Also listed are a couple of facilities that may become available in 2020-2025.

Table 2. Comparison of ULTIMATE to existing and planned integral field spectrographs

Instrument	AO	# of IFUs	Spaxel (")	IFU FoV	Number or Elements[2]	Spectral coverage (nm)	Resolution
ULTIMATE / Subaru	GLAO	8-13	0.15	1.19	61	380-1800[1]	500-3000
KMOS / VLT	non AO	24	0.2	7.84	14x6	800-2500	2800-4500
OSIRIS / Keck	NGSAO, LGSAO	1	0.02-0.10	0.32x1.28, 4.8x6.4	16x64, 48x64	1000-2400	4000
SINFONI / VLT	non AO, NGSAO, LGSAO	1	0.025, 0.1, 0.25 (AO and non AO)	0.64, 9, 64 (AO and non AO)	32x16	1100-2450	1500-4000
NIFS /Gemini	SCAO, LGSAO	1	0.04	9	30x30	900-2400	5000

Instrument	AO	# of IFUs	Spaxel (")	IFU FoV	Number or Elements[2]	Spectral coverage (nm)	Resolution
MUSE/VLT	non AO and GLAO	1	0.025, 0.2 (AO and non AO)	56, 3600 (AO and non AO)	300x120	470-930	1700-3500
GMTIFS /GMT	GLAO,NGS AO,LTAO	1	0.006 to 0.05	0.25x0.5 to 2.1x4.2 (NGSAO and GLAO)	40x20 and 20x10 (LTAO and GLAO)	1000-2400	5000-10000
HECTOR/A AT	non AO	100	1.6	15-28.5" diameter	61(?)	372-776	3000-5000

1. We have assumed that PFS can be fed by the ULTIMATE IFUs. If K band fibres become available, this range could extend out to 2500 nm.

2. For image slices, the number of elements is the number or slices times the number of spatial resolution elements.

It is clear that programs that need sample sizes of several 10s of objects are best done, object-by-object, by single-object, AO-fed spectrographs like SINFONI, NIFS, MUSE, and OSIRIS. These spectrographs have larger or comparable FoVs, better spectral and/or spatial resolutions, and broader wavelength coverage than ULTIMATE.

On the other hand, programs that do not need high spatial resolution but do need sample sizes of several hundreds are best done with KMOS.

ULTIMATE occupies an area of parameter space that none of the current instruments cover. This is shown in Figure 7. The number of IFUs versus spatial resolution. The preferred location in this plot is the upper right hand corner.where we plot the number of IFUs versus resolution. Wavelength coverage, spectral resolution, IFU FoV and the number of elements in the IFU are not considered in this plot.
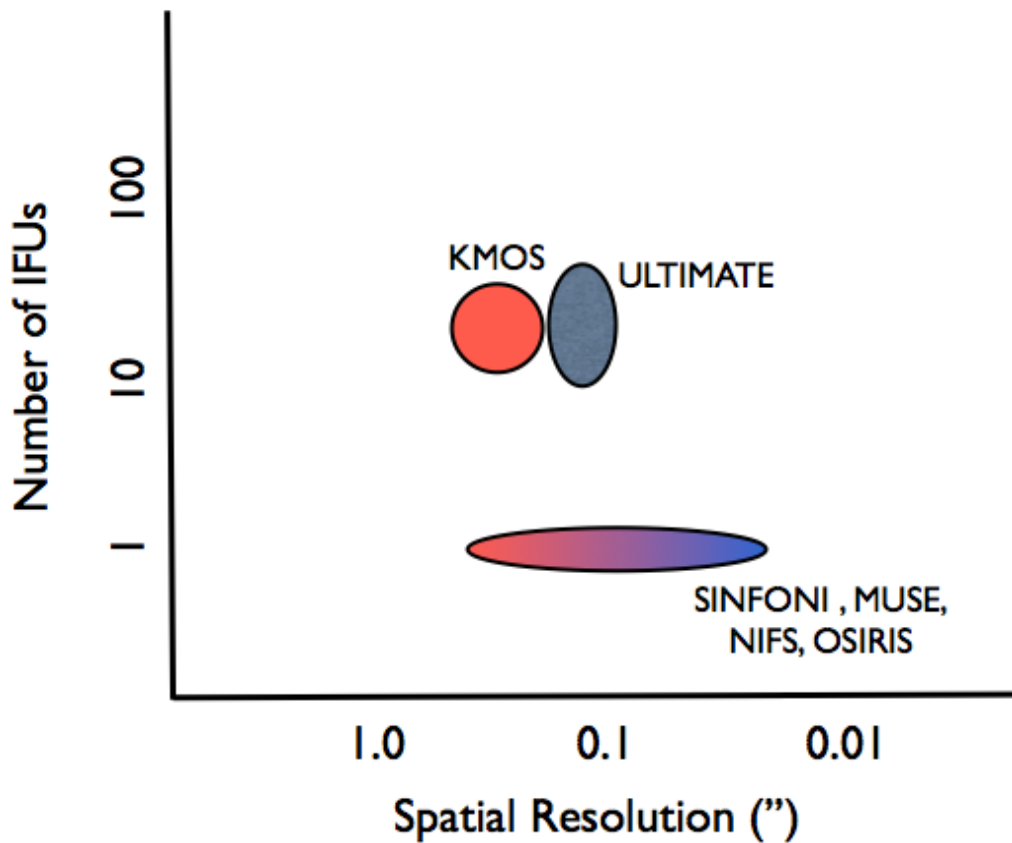
Figure 7. The number of IFUs versus spatial resolution. The preferred location in this plot is the upper right hand corner.

2.4 Feasibility Studies

We now explore the technical feasibility of using ULTIMATE to address the scientific questions raised in this document. We split this into two parts. We first examine the target density of objects that can be targeted by ULTIMATE, and we then compute signal-to-noise ratios.

2.4.1.1 Target Densities

We have used v4.1 of the UltraVISTA catalogue to estimate the likely number of targets one could observe. We consider only star forming galaxies and three redshift ranges: $0.5 < z < 0.7$, $0.8 < z < 1.0$ and $1.3 < z < 1.5$. The three intervals correspond to H-alpha landing in the Y, J and H bands, respectively and to look-back times of 5.9, 7.4 and 9.1 Gyr.

In the following figure, we plot a histogram showing the number of galaxies per 16' x 12' region (the ULTIMATE FoV) with star formation rates exceeding the values listed on the horizontal access. The red lines represent the number of ULTIMATE IFUs, which is 13 in the first phase of ULTIMATE. The intersection of the blue and red lines gives the SFR of the galaxy that is ranked 13th when galaxies are ordered according to star formation rate. We examine the signal-to-noise that one could obtain with ULTIMATE for galaxies forming this many stars in the next section.
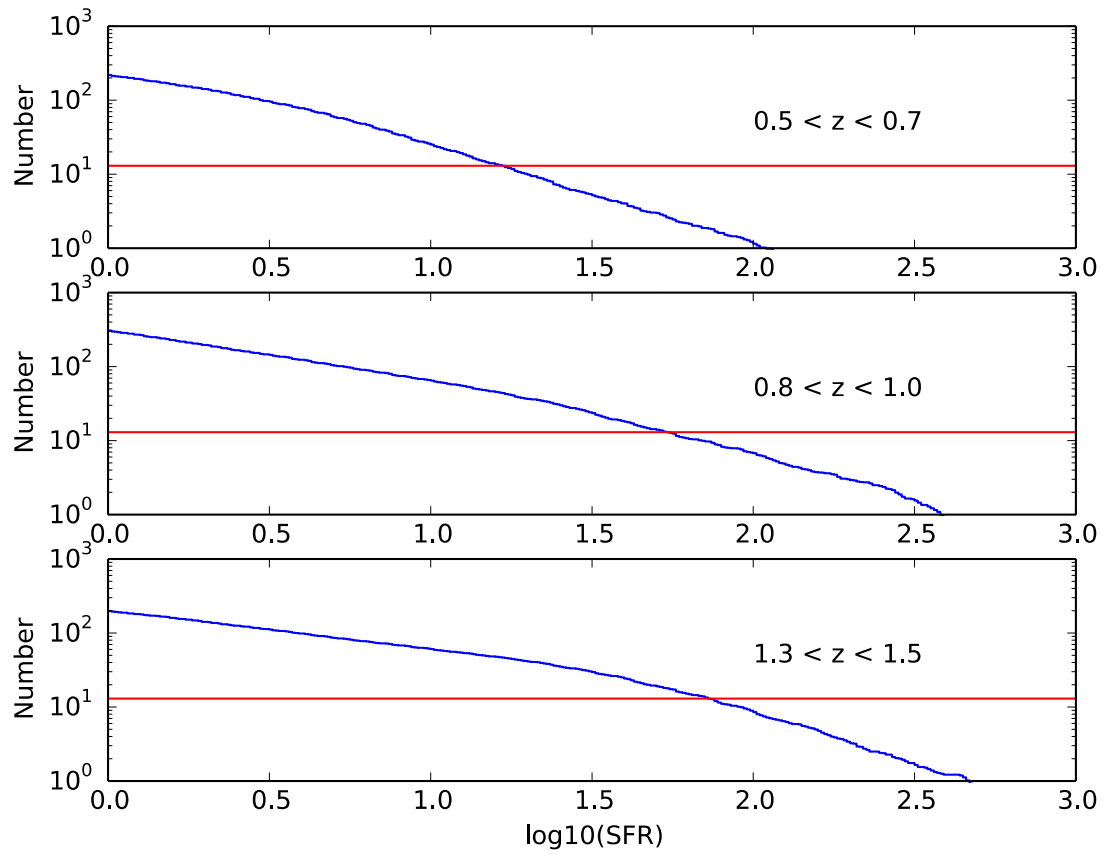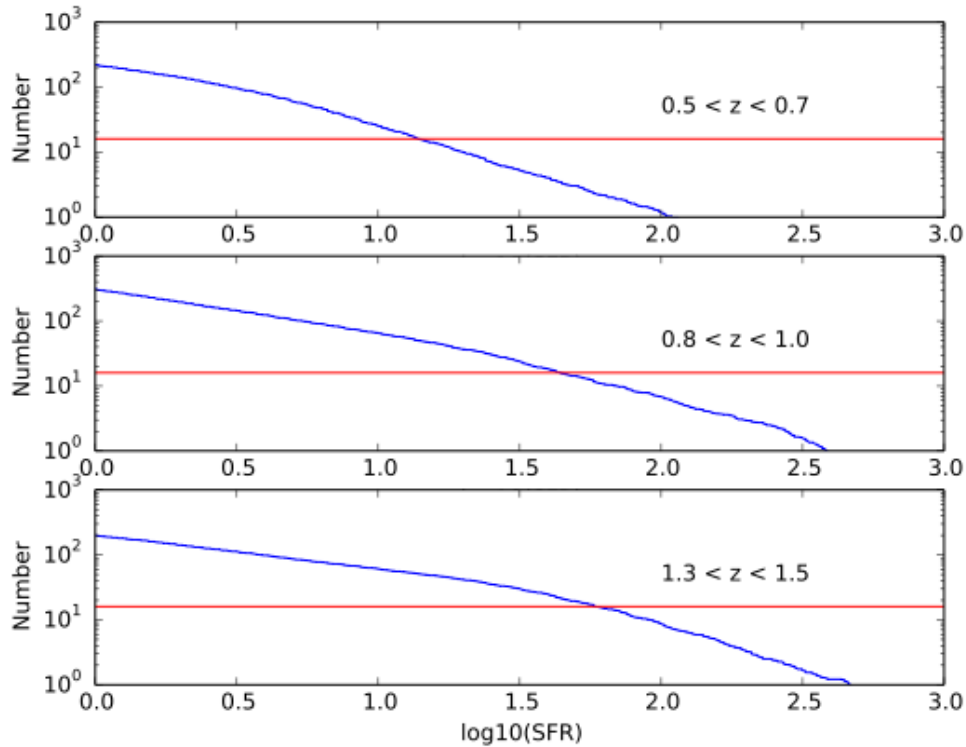
Figure 8. The Cumulative number of objects that exceed the star formation rates (SFR) listed on the horizontal axis. The star formation rates are measured in solar masses per year. The red lines correspond to the number of IFUs in stage I of ULTIMATE. The star formation rate of the Milky Way is ~1 solar mass per year, so it located on the left hand edge of these plots.

Using a SFR threshold of 10 solar masses per year there are approximately 30, 80, and 70 galaxies per ULTIMATE FoV (16' x 12') at z=0.6, 0.9 and 1.4 respectively. Over the 2 sq. degrees of the ULTIMATE galaxy survey, there would be 800, 2200, and 2000 such galaxies, respectively.

There are limitations to this analysis. The SFR is computed from the broad band photometry and there is no information on how it is distributed throughout the galaxy.

2.4.1.2 Signal to noise calculations

The expanding universe affects not only the angular size that an object subtends on the sky but also its surface brightness. Cosmological surface brightness dimming, which goes as 1+z to the 4th power for line fluxes, is especially severe.

In Table 3, we show how surface brightness dimming affects the line flux of three hypothetical SAMI-like surveys, each conducted at a different redshift (z=0.6, 0.9, and 1.4). In computing the amount of dimming, we have also taken into account the different telescope diameters (3.9-m for the AAT and 8.2-m for Subaru), and the different areas covered by the spaxels in the respective IFUs.

Table 3. The surface brightness dimming of galaxies with redshift.

Survey	Factor decrease in line flux per spaxel
ULTIMATE @ z=0.6	130
ULTIMATE @ z=0.9	260
ULTIMATE @ z=1.4	660

The amount of flux received by an ULTIMATE fibre is considerably less than the flux received by a SAMI fibre, if one were to simply place the object at higher redshift. At the same time, as features of interest move into the near-IR, the background from the night sky per unit solid angle becomes higher, as does the read-out noise of the detectors. This has important implications about what kinds of projects will be feasible. As redshifts increase, projects based on continuum measurements or line ratios involving faint lines will become infeasible.

Countering the effects of the Earth's atmosphere, cosmology, and detector technology, is the rapid evolution in the size of objects and the star formation density. Objects at higher redshifts are more compact, more clumpy, and are forming more stars, which can lead to a more extreme inter-stellar medium (Kewley et al. 2013). Hence, assessing the feasibility of a particular science case requires detailed simulations and careful consideration of all the factors.

Such a detailed feasibility study is beyond the scope of this study. Instead, we examine the feasibility using a number of assumptions that simplify the calculation. These are

- The star formation rate is 10 solar masses per year.
- The star formation is uniformly distributed throughout a disk that is 8 kpc in radius.
- The H-alpha line is represented by a Gaussian and has a width (FWHM) of 0.5 nm
- An exposure of 1 hour

Table 4. Signal to noise estimates for 1 hour observations of the H alpha line in a galaxy with a star-formation rate of 10 solar masses per year, uniformly distributed over a galaxy disc of radius 8 kpc.

Survey	S/N over 1 square arc-second	S/N per spaxel (0.15")	KMOS (0.2" by 0.2")
ULTIMATE @ z=0.6	108	15.1	10.0 (0.165 nm bin)
ULTIMATE @ z=0.9	80	11.3	7.4 (0.165 nm bin)
ULTIMATE @ z=1.4	69	9.6	2.8 (0.2 nm bin)

While the signal-to-noise ratios are sufficient for determining the large scale dynamics of the line-emitting gas using the H-alpha line, longer integrations will be necessary for inferring properties of the gas that are derived from weaker lines, such as H-beta, [NII] 6583, [SII] 6717, 6731, [OIII] 4959, 5007, H-beta, and [OII] 3726, 3728. In Table 5 we list typical line ratios. Typical line ratios have been taken from Kewley et al. (2002, 2004, 2013). Other diagnostic lines, such as [OIII] 4363, are expected to be too weak.

Table 5. Typical line strength ratios.

| Line	Ratio with respect to H-alpha	Comments
H-beta	0.3	Lower if due to dust
[OII] 3726,3728	0.5-2.0	Power law dependence on H-alpha flux, sensitive to dust
[OIII] 4959, 5007	0.3-2.0	Sensitive to dust
[NII] 6583	0.1-1.0	
[SII] 6717, 6731	0.03-1.0	

2.5 Risks

2.5.1 Data processing

Data from fibre-fed spectrographs are complex, and processing these data requires specialist software. The two most complex tasks are extraction and sky subtraction.

Accurate extraction of fluxes from fibre spectrographs depends on how well the fibre PSF and the instrumental background, both of which may vary across the array, can be modelled. In turn the accuracy at which the background and PSF can be modelled depends on how closely the fibres are packed. If the fibres are packed too closely, then the accuracy at which the flux can be extracted will be compromised. The current design places the fibres 5 pixels apart. It needs to be established that one can extract flux with sufficient accuracy when the fibres are so closely packed to one another. Examples of other fibre fed spectrographs with tightly packed fibres are the SAMI instrument, which has a fibre spacing of approximately 6 pixels, and the KOALA instrument on the AAT, which has a fibre spacing of approximately 4 pixels. Processing SAMI data has proven to be tractable (Sharp et al. 2015, Allen et al. 2015). Techniques for processing KOALA data are under development.

Accurate sky subtraction requires both accurate extraction and accurate flat-fielding, especially when the signal is faint relative to the night sky. Accurate flat fielding requires a flat field system that mimics as closely as possible a uniformly illuminated source placed at infinity.

2.5.2 IFU field-of-view

The detector area is limited, so there is a limit to the number of IFUs and the number of fibres in each IFU. With two 2x x 2k detectors and 5 pixel between fibres, the first phase of ULTIMATE can contain up to 13 IFUs with 61 fibres. A balance between the two is needed. With 61 fibres, the FoV of each IFU is 1.2 sq. arc-seconds. This may be too small for some of the science cases discussed in the document, as shown in Figure 9. An alternative choice would be to have 9 IFUs with 91 fibres per IFU. The field of each IFU would then be 1.8 sq. arc-seconds.
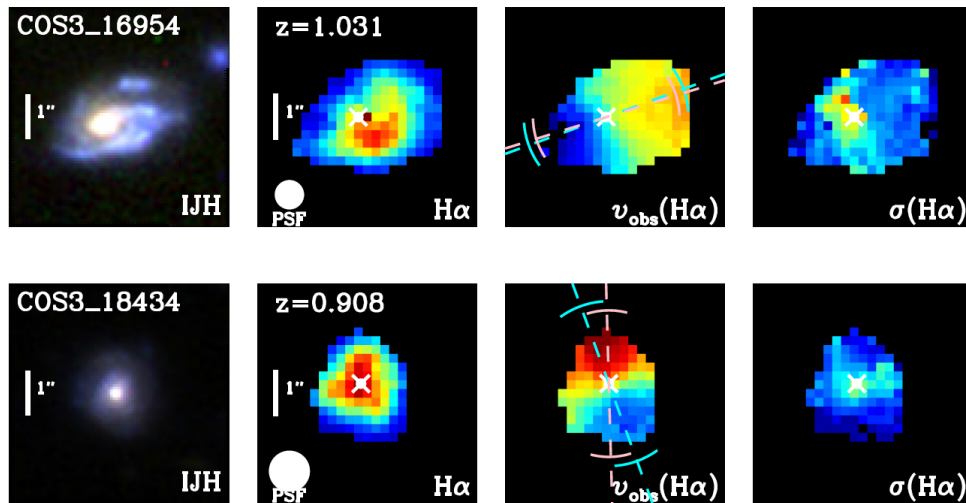
Figure 9. Results from KMOS 3D (Wisnioski et al. 2014). Note how the size of the line emitting region in these galaxies typically of the order of 2" in size. A 91 element IFU will be 1.65" wide along the widest axis. A 61 element IFU will be 1.35" wide along the longs axis

3 PROJECT OUTLINE

The development of the ULTIMATE instrument will take place in 5 stages, as follows.

3.1 Stage 1. Prototyping plan

This is the current stage. The output of this stage will be a document (this document), detailing the science case (§2), the optical design for the IFU and fore-optics (§4), the stray light analysis for the fore-optics, the background and performance model (§5), the plan for prototyping the instrument (§6), and detailed costings and schedule for the next phase and the project as a whole (§7).

3.2 Stage 2. Prototyping and instrument conceptual design

The next stage will consist of prototyping the Starbugs, IFU and fibre cable, as outlined in section 6.

These tests will result in the final concept design, including the optical design, scattered light analysis, mechanical design and a prototyping test report, as well as detailed costings and schedule for the next phase.

3.3 Stage 3. Instrument build and commissioning

This stage will complete the final design, fabrication, assembly and commissioning of the ULTIMATE instrument.

3.4 Stage 4. Spectrograph upgrade

This stage will involve the upgrade of the spectrograph to increase the throughput, support an increased number of IFUs and support OH suppression fibres.

3.5 Stage 5. OH suppression

This stage will involve the introduction of OH suppression fibres to the fibre feed.

The rest of this document deals with Stage 1.

4 INSTRUMENT DESCRIPTION (STAGES 1 - 3)

ULTIMATE is an upgrade to the MOIRCS spectrograph to enable multi-object integral field spectroscopy. It is designed to be compatible with the GLAO system, but can be used independently and prior to this For the purposes of this report the instrument is considered to consist of four main sub-systems, as shown in the block diagram in Figure 10. These are,

1. The wide field corrector,
2. The Starbugs fibre positioners,
3. The integral field units,
4. The fibre cable and slit unit.
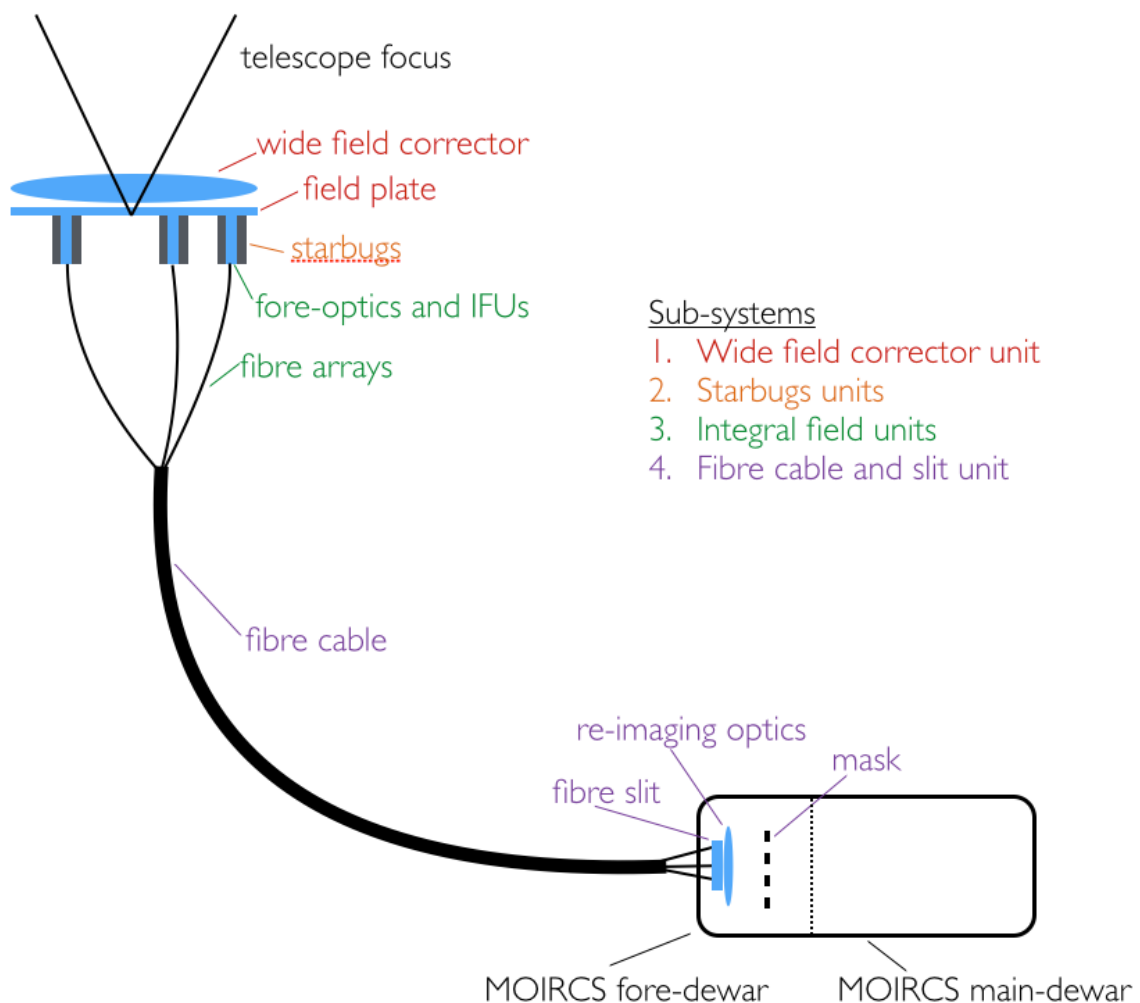
Figure 10. Block diagram of the ULTIMATE instrument, showing the sub-systems.

Each sub-system consists of various sub-components, as described in detail below.

Briefly, the instrument operates as follows. The wide field corrector corrects the astigmatism of the Ritchey-Chrétien telescope, and provides a telecentric input into the IFU optics. Deployable IFUs are positioned on a field plate at the corrected Cassegrain

focal plane of the telescope. The IFUs are positioned using robotic Starbug positioners. These can move independently of one another and over a large patrol distance, enabling efficient and versatile configuration of the IFUs. Each Starbug contains a single IFU, consisting of a hexagonally packed array of 61 hexagonal lenslets. Each lenslet subtends 0.15 arcsec on the sky (from flat-to-flat), giving a total field of view per IFU of 1.18 sq. arcsec. The IFUs image the pupil onto cores of a fibre array, and thereby feed the bench mounted spectrograph via a fibre cable, which terminates in a slit unit, which is housed, and cooled within the MOIRCS fore-dewar.

The main parameters for the instrument design are given in Table 6. Justification for these parameters may be found in the detailed instrument description below and in the science case outlined in section 2.

Table 6. Main instrument parameters

IFUs	
Number of IFUs	8 - 13[2]
Number of elements per IFU	61 Hexagonally packed
Spatial sampling per element	0.15 arcsec
Total field of view per IFU	1.18 square arcsec
Total patrol area	14 x 8' arcmin
Minimum separation between IFUs	20 arcsec
Spectrograph	
Wavelength coverage	0.9 – 1.8 µm
Spectral resolving power	500 – 3000
Dispersion	1.6 Å per pix (J), 2.1 Å per pix (H)
Sampling	2 - 5 pixels FWHM[3]
Combined properties	
Total efficiency	9 % (J), 12 %(H)

---

[2] Depends on fibre cladding and spacing along the slit. To be finalised during prototyping.

[3] Depends on fibre core diameter. The high limit would be for the larger core K band fibres, the lower limit will suit the J band only.

4.1 Wide field corrector unit

The wide field corrector unit consists of the wide field corrector itself and a field plate on which the Starbugs are located, see Figure 11.
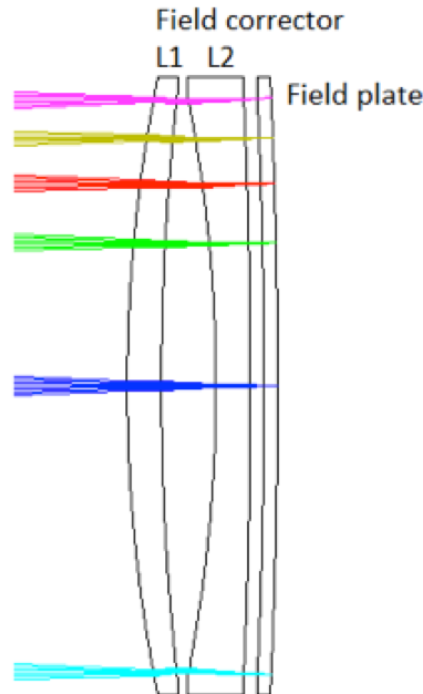
Figure 11. Ray tracing diagram of the wide field corrector optics, including the field plate.

4.1.1 Wide field corrector

The wide field corrector (WFC) has two functions. First, it corrects the astigmatism of the Ritchey-Chrétien focus over a 15 arcmin diameter field-of-view. Secondly, it provides a telecentric input for the IFU optics.

Note that the Ritchey-Chrétien telescope is designed to deliver a wavefront with no spherical aberration or coma, and these properties are preserved by the WFC.

The curvature of the field remains uncorrected, but is accommodated by use of a curved field plate (§4.1.2).

The telecentric injection into the IFU optics ensures that the geometric focal ratio degradation of the fibre injection is minimised, see section 4.3.2.

The WFC does not provide any atmospheric dispersion correction. The atmospheric dispersion in arcsec compared to λ = 0.9 µm at Mauna Kea from Zemax models are:

1.15 µm	0.17 arcsec
1.35 µm	0.24 arcsec
1.8 µm	0.32 arcsec

Thus, for an IFU diameter of ≈1.35 arcsec (see §2) atmospheric dispersion will be negligible, and in principle could be corrected post hoc.

The WFC delivers excellent image quality across the entire field of view across all MOIRCS spectroscopic bands, J, H and K, see Figure 12.
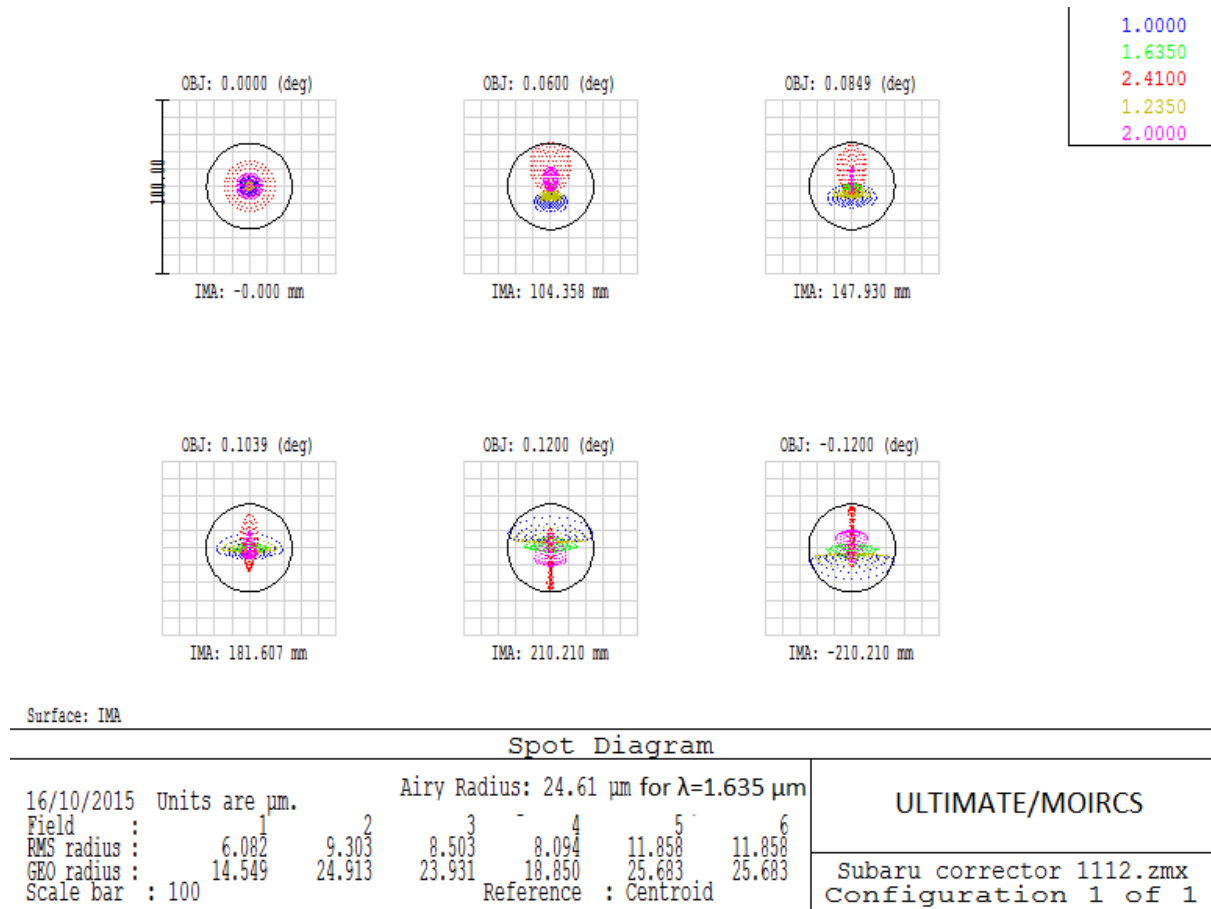
Figure 12. Spot diagrams for the Subaru telescope plus wide-field corrector.

A summary of the optics of the WFC is given in Table 7.

Table 7. Summary of the optical parameters for the wide field corrector.

Field corrector	
Clear aperture diameter	440 mm
Center thickness L1 and L2	25 mm
L1 to L2 separation	40 mm
Material of L1 and L2	Fused silica
Image quality, center/edge of field of view	0.10/0.46 waves PV at 1.0 micron
	0.03/0.23 waves PV at 1.6 micron
	0.10/0.20 waves PV at 2.0 micron
	0.13/0.18 waves PV at 2.5 micron

4.1.2 Field plate

The field plate provides a surface for the Starbugs to move around the focal plane. The field plate is curved to accommodate the Petval curvature of the telescope focus (§4.1.1), ensuring that there is no defocus across the patrol field.

The beam footprint of a point source on the first surface is 0.24 mm, and on the second surface (the Starbug side) it is 0.32 mm. Thus the effect of surface defects, such as dust and scratches, will be negligible, since typical sizes are much smaller than the footprint.

The size of the field plate is comparable to the size of the WFC lenses, see Table 7 and Table 8. Thus the field plate can be manufactured along with the WFC using conventional techniques.

Table 8. Optical parameters for the field plate.

Field plate	
Clear aperture diameter	440 mm
Center thickness	10 mm
Sagitta	5.1 mm
Radius of curvature	~4700 mm, convex on the Starbug side (S2)
Field of View	Ø15' on sky
Beam footprint	S1: Ø0.24 mm
	S2: Ø0.32 mm
Telescope focus	4 mm from S2 in air
Plate scale	0.480 mm per arcsec
Material	Fused silica

4.2 Starbugs unit

The IFUs will be deployed on a field-plate located at the focal plane of the telescope, see Figure 11. The IFUs will be positioned on this field-plate using Starbugs positioners, developed at the AAO. This technology has undergone extensive development for the TAIPAN instrument being built for the UK Schmidt Telescope. The Starbugs for ULTIMATE are based on these designs.

Each Starbug contains one IFU, and is positioned simultaneously and independently from the others. The positional accuracy of Starbugs is better than 5 microns,

corresponding to 10 milli-arcseconds on sky, and typical reconfiguration times are achievable within the time taken to slew the telescope.

4.2.1 Overview

For a Cassegrain instrument such as ULTIMATE, the Starbugs will be located on the underside of the field-plate. The Starbugs adhere to the glass by creating a negative pressure within the Starbug body, which is routed from an external vacuum system.

The principle of operation of a Starbug is illustrated in Figure 13. Each Starbug consists of two coaxial piezo-electric tubes. The fore-optics and IFU are housed within the central tube as discussed below. The Starbug is made to walk by electronically controlling the piezo-tubes such that they extend, contract and bend as shown by the sequence in the middle panel of Figure 13.
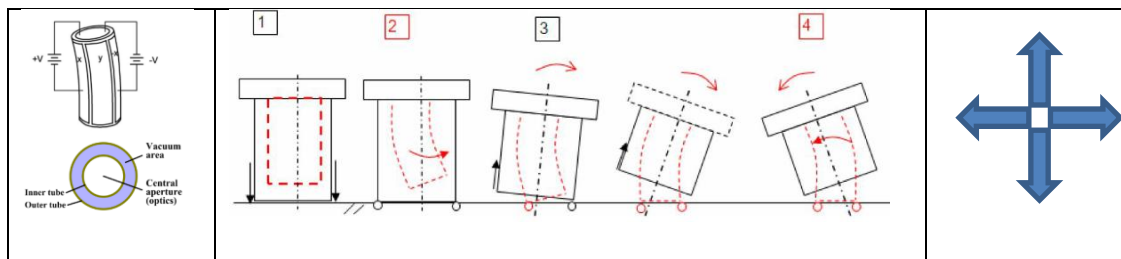
**Figure 13. The principle of operation for a Starbug.**

Precise closed loop control of directional and rotational motion is enabled by an on-axis metrology camera, which observes three backlit metrology fibres (fiducials) on each Starbug, as shown in Figure 14. The IFU axis is defined with respect to these metrology fibres. Additionally there are a number (≈ 16) of circumferential fiducials on the glass-field plate. Thus, fine positioning is then achieved while the telescope is on target by referencing the Starbug fiducials to the field-plate fiducials. Acquisition is then achieved by aligning guide bundles to guide stars.
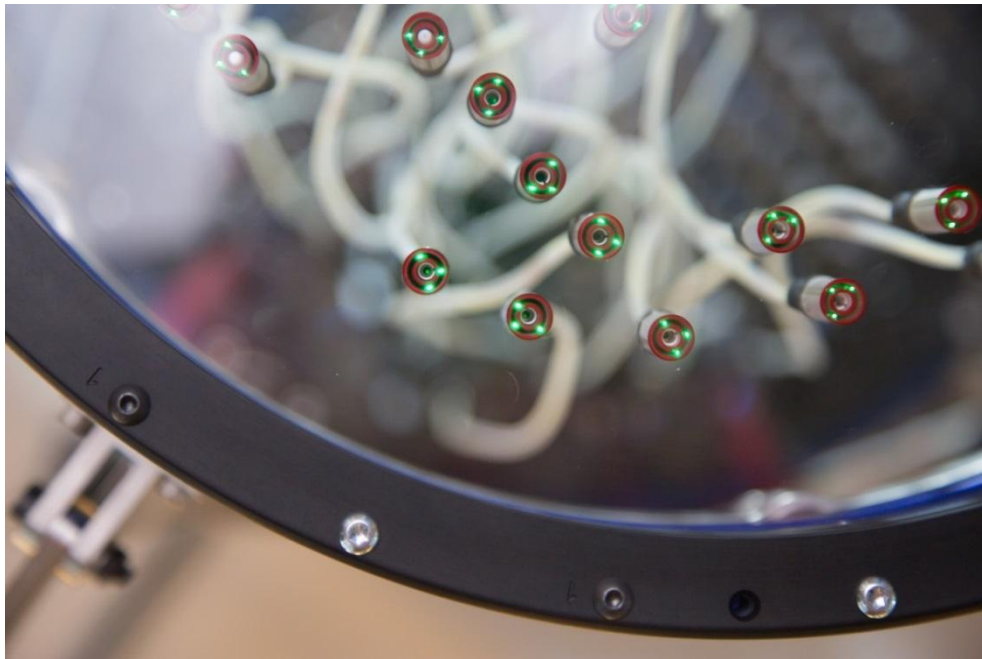
Figure 14. Starbugs on a field-plate, showing the green back-lit metrology fibres, and the red slippers.

### 4.2.2 Starbug design for ULTIMATE

Each ULTIMATE Starbug will contain the fore-optics, microlens array and fibre array for one IFU (see section 4.3). These optics will be aligned and glued into position in a stainless steel tube as shown in Figure
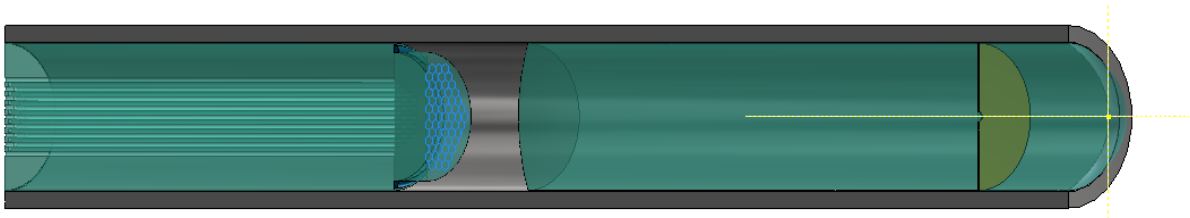
This tube can then be inserted into the Starbug, using a precision fit between the tube and a corresponding payload dock in the Starbug; see Figure 15 and Figure 16. The open top of the Starbug allows the vacuum tube, the three metrology fibres, seven wires and the payload bundle to hang down separately from the inverted Starbug. This concept allows, if necessary, the entire optics tube to be removed and replaced within the payload dock. This design feature allows the rather high value optics of the IFU unit to be seperable from the Starbug itself. It enables the Starbug to be a line replacable unit (LRU). This design feature has also been employed with the TAIPAN Starbug design.
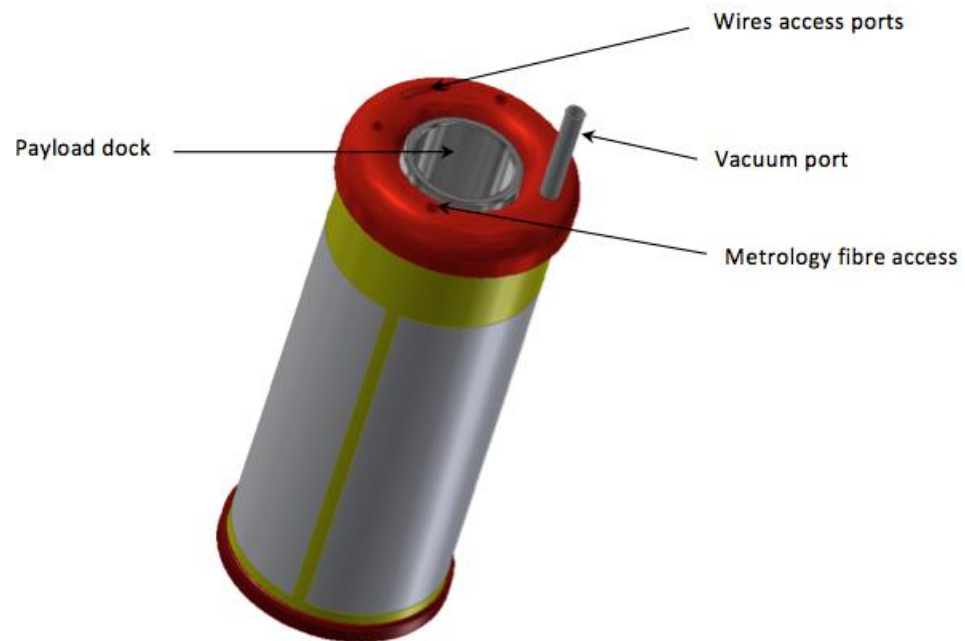
Figure 15. ULTIMATE Starbug, showing the payload dock tube, metrology fibres, vacuum port and wires access ports.
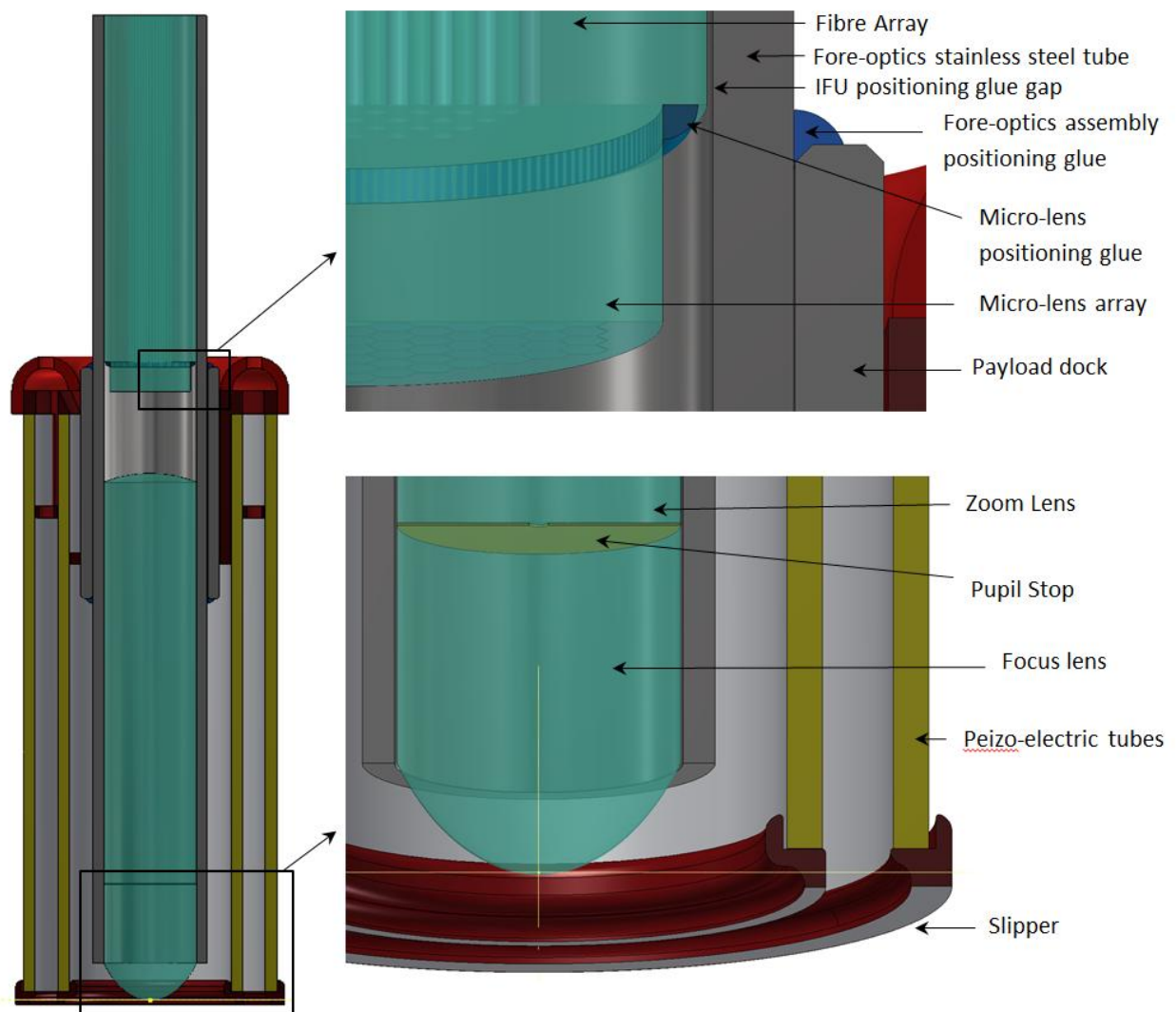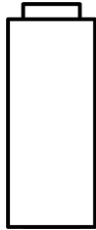
Figure 16. Cross-section of the fore-optics and IFU assembled within a Starbug positioner.

The ends of the Starbug piezo tubes in contact with the field-plate are inserted and glued into "slippers", shown by the red rings in Figure 14 - Figure 16. Slippers are a 3D printed glass-like plastic ring, which provide multiple critical functions for the Starbug. Slippers provide mechanical rigidity and containment for the fragile piezo-electric ceramic (sintered lead zirconate titanate powder). The outer diameter of the slippers matches the outer diameter of the vacuum seal at the top of the Starbug, so when adjacent Starbugs touch they maintain orthogonality to the field plate, which is imperative to maintaining an effective and continuous vacuum seal. The outer diameter also provides sufficient electrical separation for a 400V potential between impinging electrodes on adjacent Starbugs. Slippers provide a sufficient coefficient of friction to provide traction for the Starbug to "walk". Slippers have a hardness property that does not damage the optical coatings on the glass field plate.

The proposed Starbugs for ULTIMATE will require design development for the increased holding force required compared to the existing TAIPAN technology. An increased holding force is required because the payload consisting of fore-optics and

IFU is heavier, than the single fibres used for TAIPAN, and additionally the fibre bundle is more rigid. The holding force is proportional to the cross sectional area between the outer tube and the inner tube, to which the vacuum is applied, and to the pressure differential between the atmospheric pressure and vacuum supplied. The pressure differential available at the altitude of the Subaru telescope is approximately 60% of that available at the UK Schmidt Telescope due to the difference in elevation. A prototype Starbug with a 12 mm diameter will achieve twice the holding force compared to TAIPAN. This defines the baseline design for initial testing. This diameter will be increased or decreased as required during prototyping to ensure sufficient holding force at the simulated altitude. The resulting diameter will determine the final separation between IFUs. A 12mm Starbug results in a separation distance between IFUs of 25 arcsec when implemented on the SUBARU telescope.

Table 9. Results from Starbug size and performance testing. The top row is for an ULTIMATE Starbug; the bottom row gives the parameters for a TAIPAN Starbug for comparision.

Footprint	Length	Dimensions Outer Tube/ Inner Tube (OD x ID x L) (mm)	~Inner Tube step (µm)	~Outer Tube lift (µm)	Vacuum area (mm²)
◎		12 x 11 x 28 Halved Elec.	22	14	45
		8 x 7 x 30 Quartered Elec.			
◎		8 x 7 x 22 Halved Elec. (Quartered OK)	23	10	19
		5 x 4 x 25 Quartered Elec.			

If the separation between IFUs is required to be minimised, there are future design possibilities to mount the payloads externally to the Starbug, thus enabling Starbugs to be positioned contiguously.

4.2.3 Connector plate

The ULTIMATE Starbugs are currently designed as line replaceable unit (e.g. TAIPAN LRU, Figure 17). Each Starbug requires 7 high voltage connections, 1 vacuum connection, 3 metrology optical connections. These are all interfaced at a connector plate, located beneath the field-plate, see Figure 18. There is no connector for the ULTIMATE observing fibres, which will pass unobstructed through holes in the connector plate.

Figure 17. Starbug LRU for TAIPAN. The 15 mm LEMO plug contains 9 wire connections, 1 vacuum connection and an observing fibre in the central optical connection.
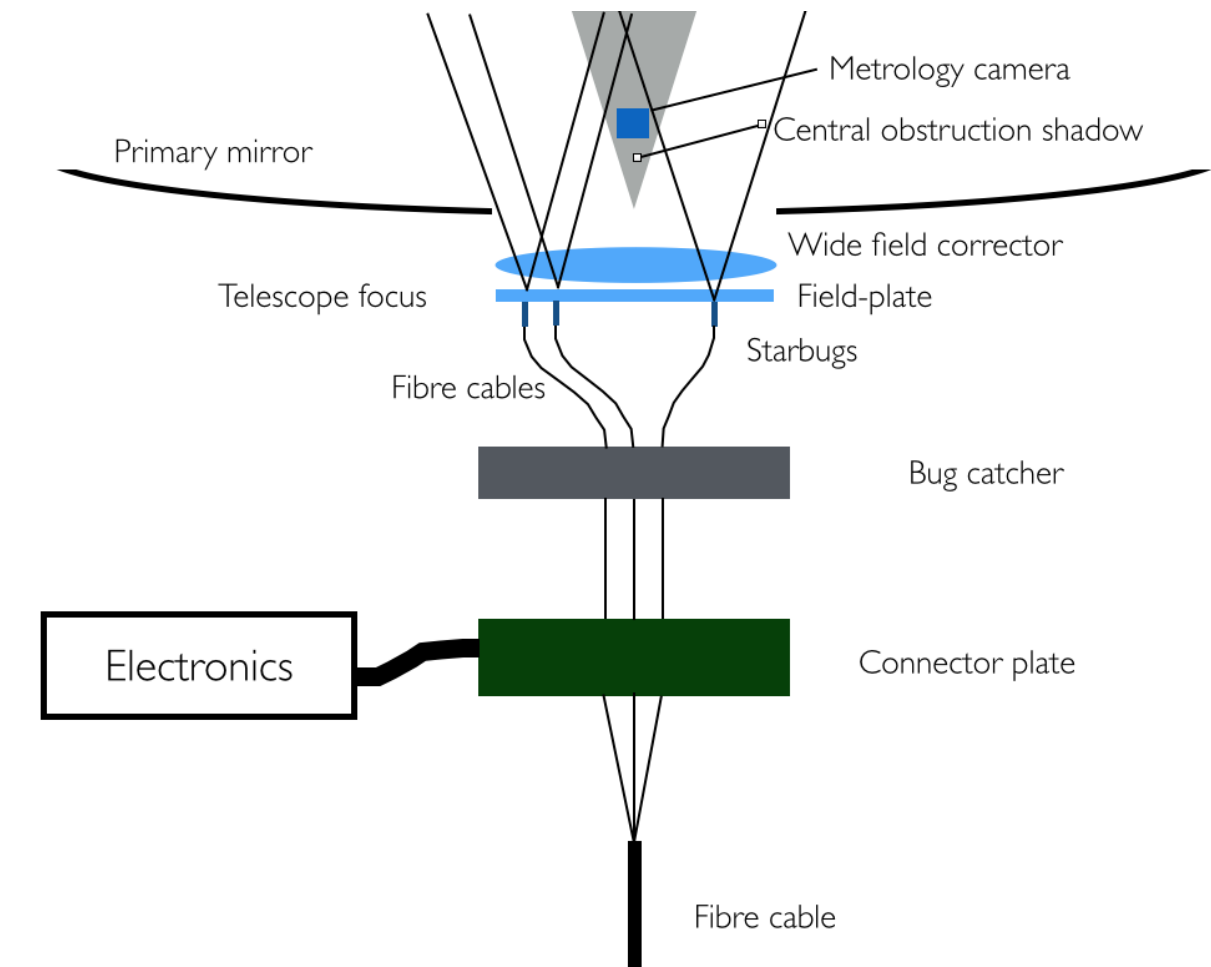
**Figure 18. Schematic diagram of the Starbugs unit.**

4.2.4 Bug catcher

Between the field-plate and the connector plate is the bug-catcher. A photograph of a TAIPAN bug-catcher is shown in Figure 19. For TAIAPN, the Bug Catcher is a 3D printed ABS plastic structure that moves along the axis of the instrument between the connector plate and the glass field plate.

In the event that vacuum is sensed to be reaching a failure condition, the Bug Catcher moves along the Starbug cords to support the piezo electric tubes. It also supports and protects Starbugs during Starbug replacement and glass field plate cleaning. The bug catcher doubles as a positioning device to place and hold the Starbugs against the glass field plate for vacuum adherence.

The LEMO plug shown in Figure 17, would be baseline for ULTIMATE and can be used for all wiring and vacuum with the three metrology fibres terminated into a single central ferrule. The accepting LEMO socket will have a single 0.530 mm acrylic fibre terminating at an LED with a wavelength that matches the metrology camera sensitivity.
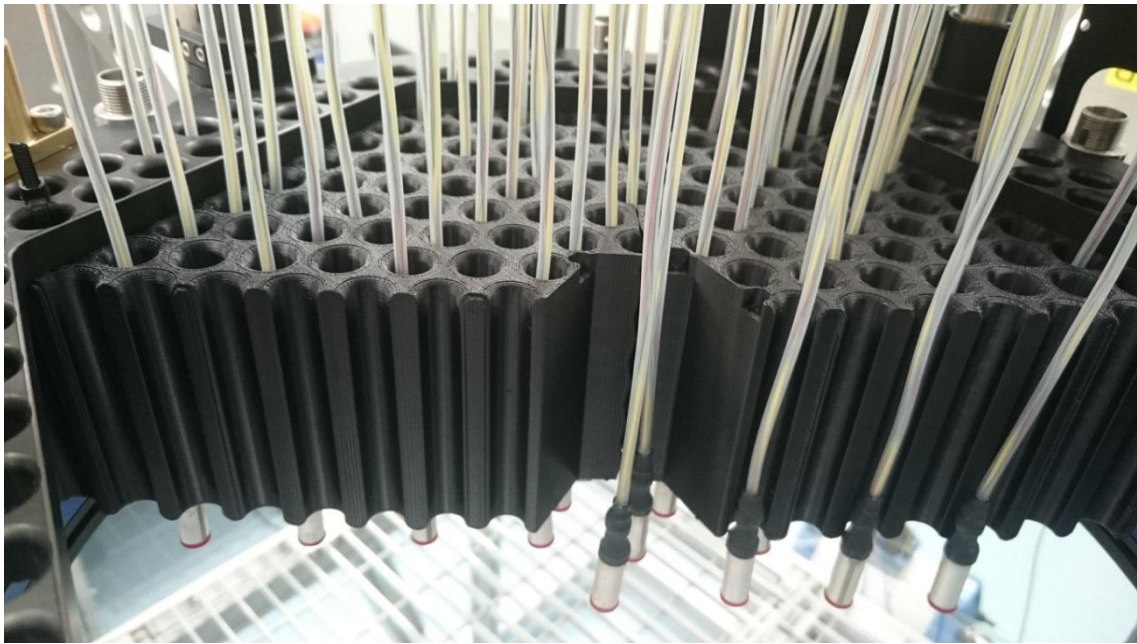
Figure 19. The bug catcher. Half the structure has been removed to show the protective tubes. Note that this prototype is inverted compared to the ULTIMATE device, in which the Starbugs and fibre cables will hang down beneath the field plate, looking up towards the Cassegrain focus.

The bug-catcher for ULTIMATE would require some further development from that developed for TAIPAN. The TAIPAN instrument places Starbugs onto a curved field plate in a downwards position. Placing Starbugs onto a curved and upwards looking field plate presents some challenges, since after positioning the bugs, the bug-catcher must retract without pulling off the bugs, which is not trivial for a curved field plate.

4.2.5 Metrology camera

The metrology camera measures the position of the Starbugs relative to fiducial back-lit metrology fibres on the circumference of the field plate. The camera needs to be on axis facing the Starbugs with consideration for focal length, CCD pixel size, Starbug metrology fibre diameter, positioning precision requirement, light path shadowing, wide-field corrector distortion and telescope geometry. The camera's position can be decided when all this information is available and compromises are agreed. It may be possible to place the camera in the shadow of the central obstruction above the field plate.

4.2.6 Vacuum

Cooling systems may be required for vacuum pumps to function normally at the altitude of the Subaru telescope. Oversized vacuum pumps running at a fraction of their capacity require less cooling. An adhered Starbug still allows a nominal vacuum leakage rate. Pressure is maintained by closed loop control with constant vacuum pumping to maintain system vacuum. TAIPAN uses a 650 kPa pressure differential at the Starbug plus system overhead. Subaru atmospheric pressure is only 614 kPa and the Starbug diameter must be modified to maintain sufficient holding force.

4.2.7 Electronics

The Starbug electronics and most ancillary sensors, motors and solenoids developed for TAIPAN can be used for ULTIMATE without modifications. Temperature dissipation from amplifiers at altitude will require additional cooling.

Figure 20 The ten high voltage switch cards in the foreground drive 80 Starbugs. Only two of these cards are required for 16 Starbugs.

4.3 Integral Field Unit

ULTIMATE will have 13 TBC IFUs, which are housed within and positioned by the Starbugs (§4.2). Each integral field unit consists of three main components, the fore-optics, the lenslet array, and the fibre array.

4.3.1 The fore optics

The fore-optics magnify the beam from the telescope to provide an appropriate plate scale for the lenslet array.

In principle one could place the lenslet array directly at the focal plane of the WFC. For the plate scale at the field plate of 2.083 arcsec/mm this results in a lenslet width of 72 µm for a sampling of 0.15" per lenslet, see Figure 21.
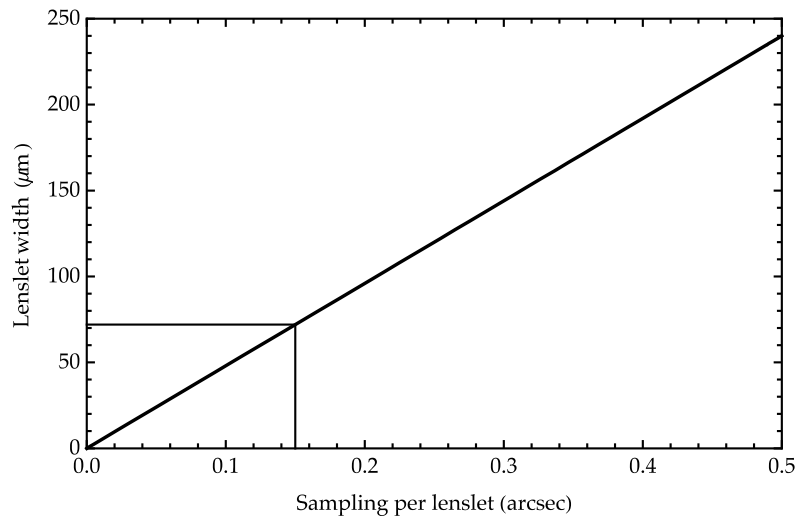
Figure 21. The required lens size as a function of the sampling per lenslet, at the focal plane of the wide field corrector.

However, there are advantages to a larger physical lenslet size. Most fundamentally, a large lenslet size compared to the fibre core diameter minimises shifts in the pupil image and geometric FRD (see §4.3.2).

Secondly, arrays of 72 µm lenslets are not readily available from manufacturers and are likely to be expensive and to pose a significant risk in meeting the required specifications. In particular the fill factor for microlens arrays with a pitch < 100 µm will be < 80%.

Thirdly the AAO has significant experience working with larger lenslets, having used a 40×25 250 µm lenslet array for KOALA, and with similar arrays for PRAXIS and GHOST.

Additionally the use of fore-optics has advantages other than its effect on lenslet size. First, the spatial sampling of the IFUs could be changed by changing the fore-optics, without changing the lenslet array. Secondly, the use of fore optics allows one to incorporate a pupil stop to minimise thermal emission and stray-light.

A ray diagram for the ULTIMATE fore-optics is shown in Figure 22. The fore optics consist of two plano-convex lenses that are bonded together. The planar face of the second lens will be coated in a low emissivity material in order to create a pupil stop at the interface between the two lenses. Additionally the outer surface of the second lens will also be coated in low emissivity material in order to shield thermal and stray light from within the Starbug.
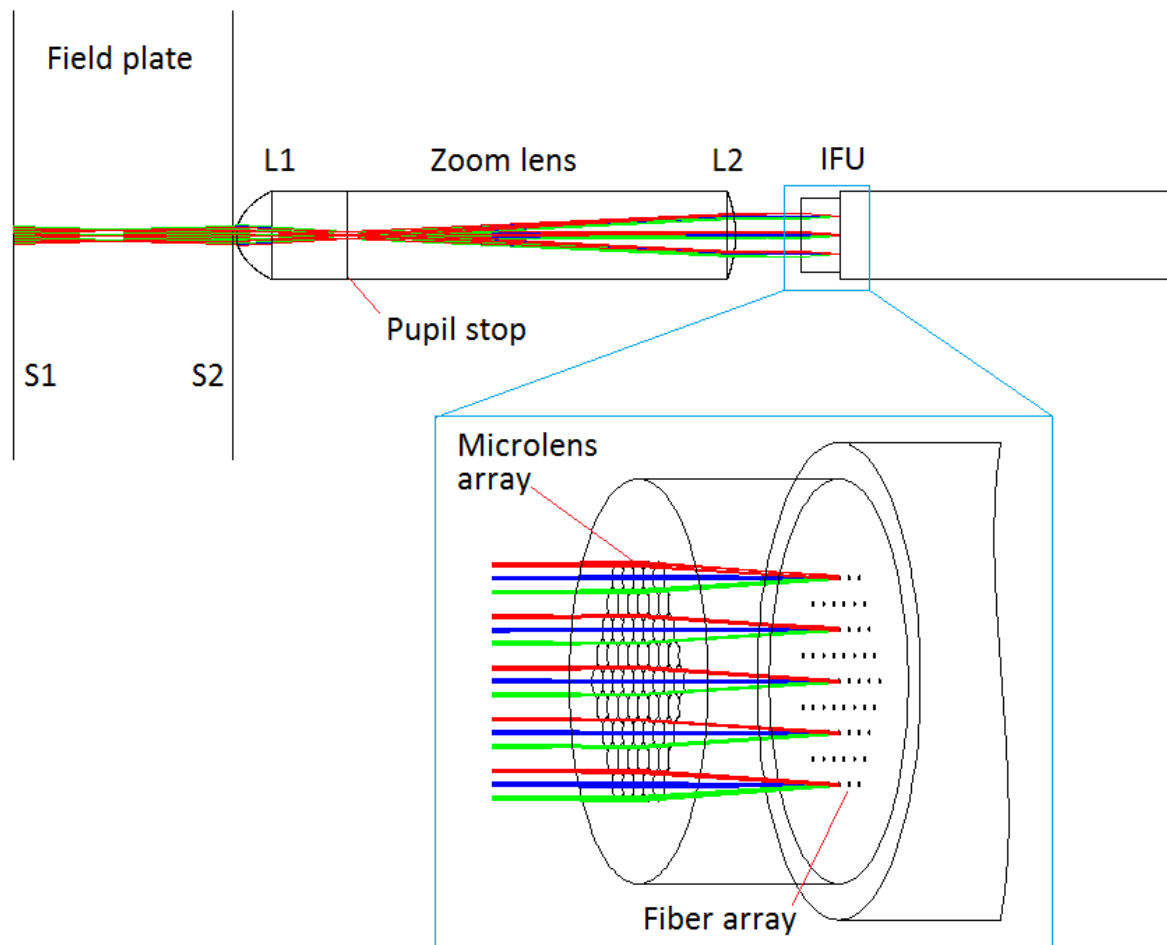
Figure 22. Ray diagram for the ULTIMATE fore optics and lenslet array.

The optical parameters for the fore-optics are given in and the manufacturing and alignment tolerances are given Table 10 and Table 11.

Table 10. Optical parameters for the fore optics

Fore optics	
Axial dimensions	
Telescope focus to lens	4.2 mm in air
Field plate to first lens	0.2 mm
L1 to pupil stop	5.0 mm in fused silica
Pupil stop to L2	17.8 mm in fused silica
Lens to ML array	3.0 mm
ML array thickness	1.8 mm
Fibre multi bore ferrule	~15 mm

Apertures	
Field of view	Ø1.35" on sky
	Ø0.65 mm in telescope focal plane
Lens dimensions	
Outer diameter	4 mm
Clear aperture L1	0.9 mm
Pupil stop	0.28 mm
Clear aperture L2	2.3 mm
Magnification	3.5x
Output f-number	f/43.4
Wavelength range	1.0-2.5 µm
Wavefront quality	0.1 wave peak-to-valley
L1 surface figure	Ellipsoid, convex
Radius of curvature at vertex	1.552 mm
Conic constant	-0.6377
L2 radius of curvature	5.566 mm, convex

Table 11. Manufacturing and alignment tolerance for the fore-optics

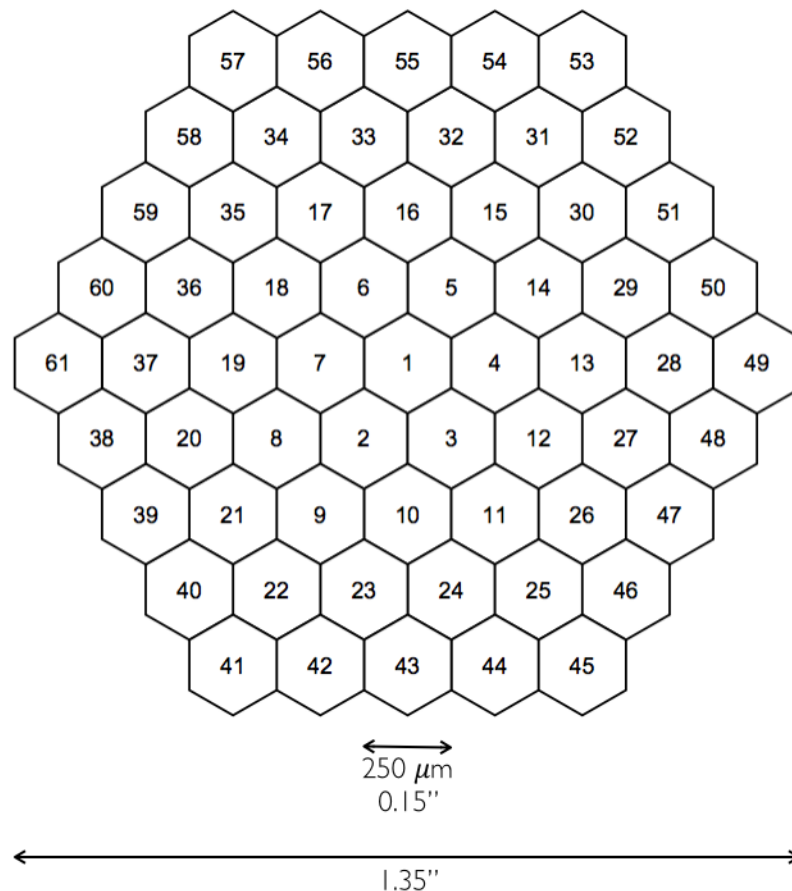| Fore-optics				
Manufacturing tolerances			**Alignment tolerances**	
Radius of curvature S1	0.3%		L2	reference
Radius of curvature S2	1.0%		Decenter S1	0.01 mm
Center thickness L1	0.1 mm		Tilt S1	0.1 deg
Center thickness L2	0.2 mm		Tilt L1 wrt L2	0.1 deg
Irregularity	0.5 wave		Decenter of pupil stop	0.01 mm
Diameter L2 (reference)	+0/-10 µm		Tilt of Starbug	0.1 deg
Diameter of pupil stop	1 µm		Tilt of lens assembly in Starbug	0.1 deg
Decenter S2	0.02 mm			

4.3.2 Lenslet array

The lenslet array samples the image in order to provide spatially resolved spectroscopy. There several advantages to using a lenslet array for the sampling, over using a bare fibre array (e.g. PPAK, MANGA).

A lenslet array provides a contiguous field of view with high fill-factor, as it is unaffected by the cladding of the fibres, which otherwise create dead space in the array.

A lenslet array allows the formation of a pupil on the face of the fibre. Both the size of the pupil, and the focal ratio can then be chosen so as to optimise the coupling efficiency into the fibre.

In the case of ULTIMATE a 250 µm pitch hexagonally packed lenslet array with 61 elements will be used. Each lens subtends an angle of 0.15" on the sky, measured from flat-to-flat, see Figure 23. The design of the fore-optics and microlens array follows from these constraints. These optics have been deisgned and optimised using Zemax, but here we give an approximate treatment to describe the main features of the optics.

250 µm
0.15"

1.35"

Figure 23. Arrangement of the microlens array.

The plate-scale of the Cassegrain focus after the wide field corrector is 2.083 "/mm. The microlenses have a width of 250 µm, and are required to subtend 0.15". Therefore the fore-optics must have a magnification of

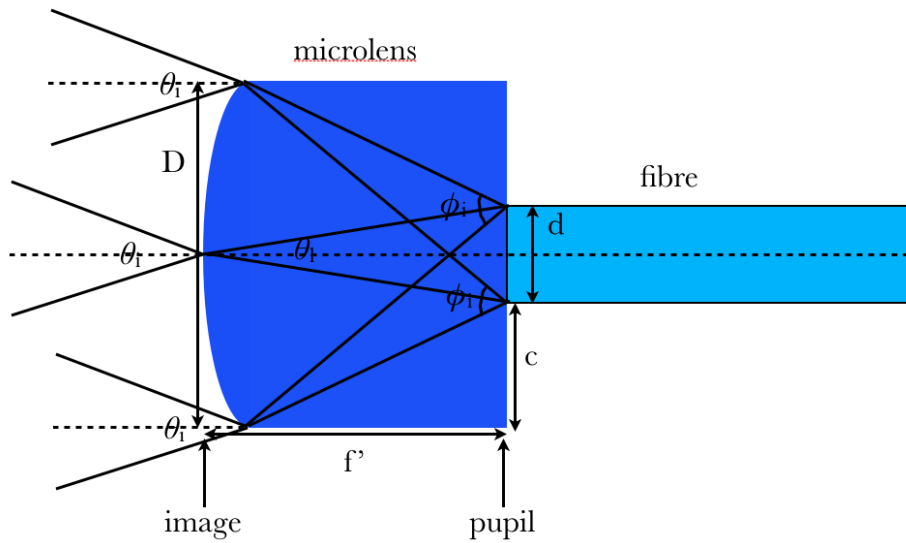$$M = \frac{0.250 \times 2.083}{0.15} \approx 3.5 .$$

The focal ratio on the front face of the microlens is then

$$F_{\text{lens}} = MF_{\text{cass}} \approx 43.3 .$$

Considering Figure 24, the diameter of the pupil image formed on the face of the fibre is given by

$$d = f'q_1 = fq_i = \frac{f}{F_{\text{lens}}} ,$$

where $f = f'/n$ is the focal length of microlens in air.

Figure 24. Schematic diagram of the formation of a pupil image on the face of a fibre using a microlens.

Furthermore, it is required to feed the fibres at a focal ratio $F_{\text{fibre}} = 4$ to minimise the effects of FRD. Considering エラー!参照元が見つかりません。,

$$F_{\text{fibre}} \approx \frac{f}{D_{\text{lens}}} ,$$

and therefore

$$d \gg \frac{D_{lens}F_{fibre}}{F_{lens}} \gg 23.3\,mm.$$

In fact, the full analysis using Zemax gives $d = 29$ µm. Therefore the fibre core diameter must be larger than 29 µm to allow for slight misalignment, and still capture the entire pupil image. However, oversizing the fibres also increases the amount of thermal emission captured by the fibre, see Section 5.2.

N.B. the size of the pupil image formed on the fibre is fixed, and is independent of the microlens diameter.

For a single microlens the off-axis light can have a higher angle of incidence at the fibre face as can be seen in the marginal rays illustrated in Figure 25. This is equivalent to feeding the fibres at a faster focal ratio and is known as geometric focal ratio degradation. As shown below this is not a significant problem for ULTIMATE.
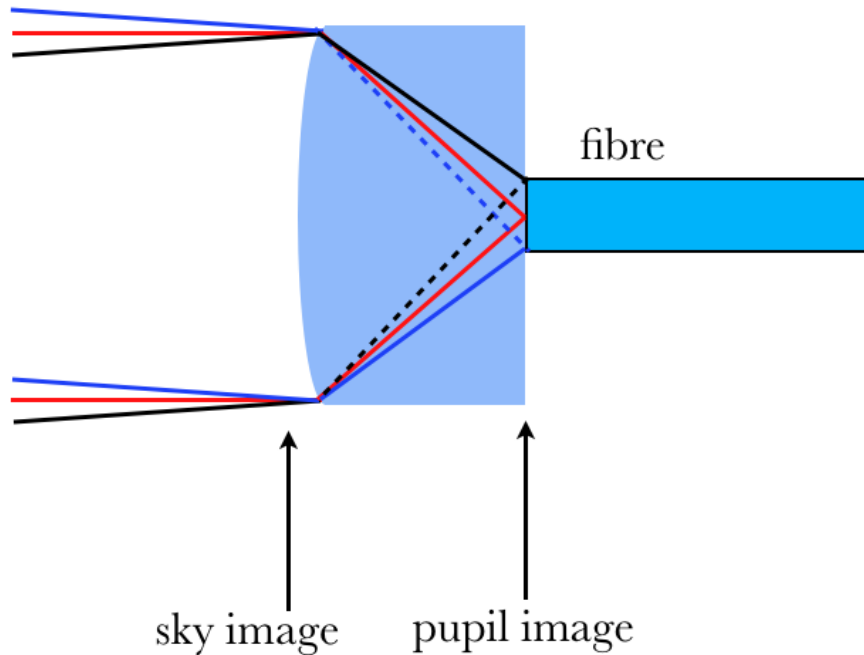
Figure 25. Schematic diagram of a single microlens feeding a fibre. The marginal rays shown by dashed lines have a greater angle of incidence than the chief rays shown in red. This is equivalent to feeding the fibre at a faster focal ratio and is known as geometric FRD.

The maximum angle of incidence which the marginal rays can make is,

$$q_{max} = \frac{D_{lens} + d}{2f},$$

and therefore the minimum focal ratio is,

$$F_{min} = \frac{f}{D_{lens} + d},$$

and thus the ratio of the on-axis focal ratio to the minimum focal ratio is,

$$F = \frac{F_{fibre}}{F_{min}} = \frac{D_{lens} + d}{D_{lens}}.$$

For 250 µm lenses and a 35 µm core, the ratio is Φ=1.14, leading to only a small amount of geometric FRD, due to the fact that the microlens diameter is significantly greater than the fibre core diameter.

4.3.3 Fibre Array

The microlens array will be bonded to a fibre array. The fibre array will consist of multi-bore ferrule at the same pitch (250 µm) as the microlens array, and precisely aligned to it.

The various options for the construction of the fibre array are discussed in the prototyping section 6.4.3.

4.4 Fibre cable

4.4.1 Fibre type

It is necessary to have a fibre core diameter of ≈ 35 µm such that the pupil image formed by the microlens array is wholly within the core, with some room for misalignment (±3 µm) (section 4.3.2).

The cladding should be less than 120 µm if there is to be sufficient space to accommodate the 61 fibres of each of 13 IFUs along the slit, see Table 13. A separation of 80 µm between fibres along the slit is sufficient to ensure the fibre-to-fibre cross-talk is less than 1% (section 4.4.3.1), and thus there is no requirement for cladding less than 80 µm.

For good transmission at λ < 1.8 µm, it is necessary to use a low OH fibre. Figure shows the transmission of Polymicro FI fibre as an example. Another possibility is CeramOptec Optran Ultra WFGE.
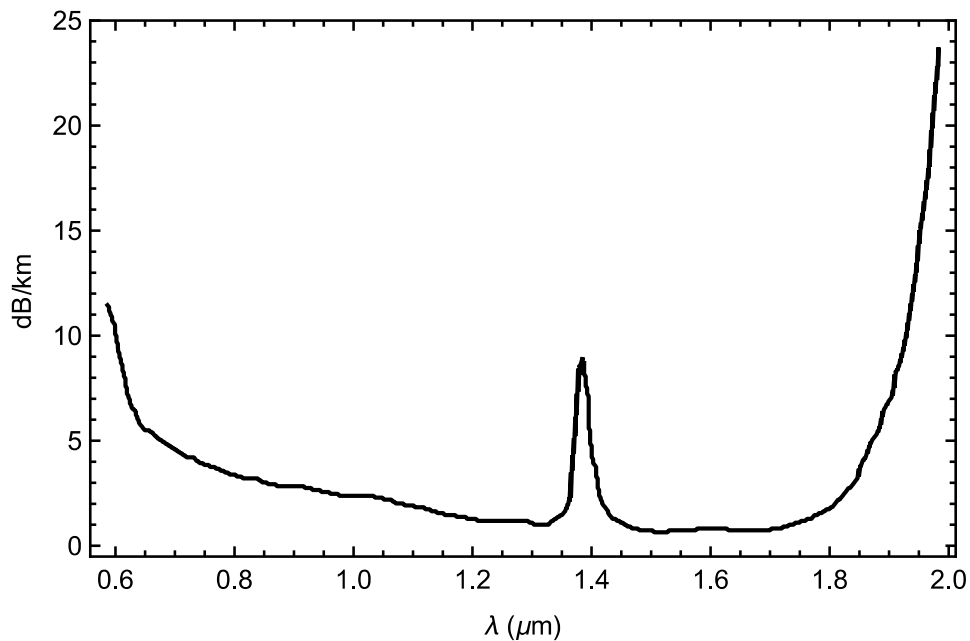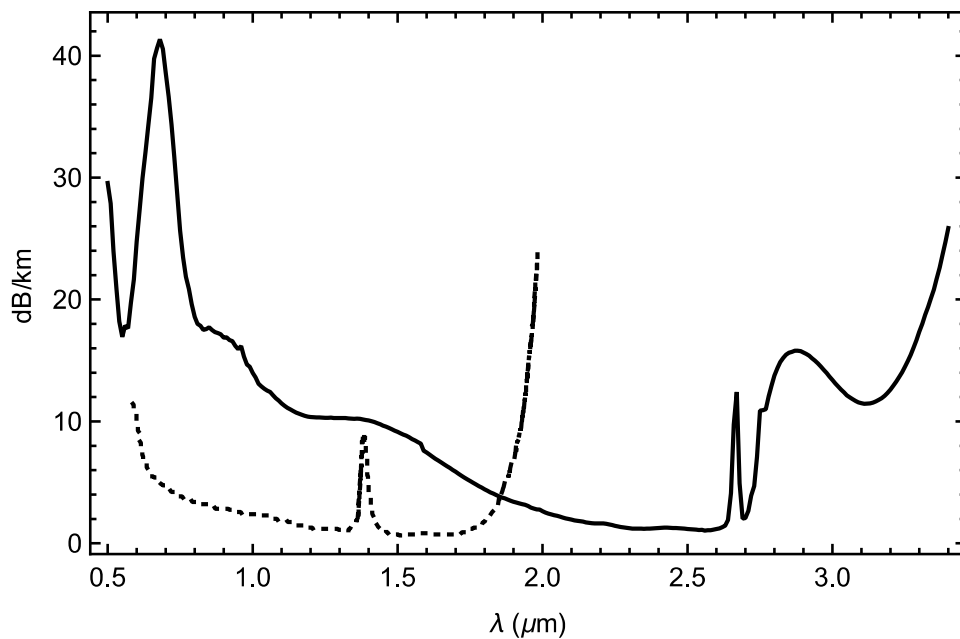
Figure 26. Transmission of low OH Polymicro FI fibre.

4.4.1.1 K band fibres

An alternative to the low OH silica fibres discussed above is to use ZBLAN fluoride fibres to extend the transmission of the fibres into the K band. Historically, K band fibres have seen only limited use in astronomical applications because of poor transmission and fragility of the fibres. However, recent developments now make these fibres a viable option.

ZBLAN fibres consist of a family of fluoride glasses, viz. ZrF_4, BaF_2, LaF_3, NaF, and AlF_3. The cross-over between the Rayleigh scattering losses and the multi-phonon absorption losses occurs at ≈ 2.5 µm; thus ZBLAN fibres have their best transmission in the K band.

Figure 27 shows the measured transmission of a ZrF_4 made by Le Verre Flouré. Le Verre Flouré have over 30 years experience working with ZBLAN glasses and fibres, with astronomy constituting 40 % of their current business. Another manufacturer is Fiberlab, Japan, who make both ZrF_4 and AlF_3 at cheaper rates than Le Verre Flouré, but with higher losses.

Figure 27. Measured transmission of Le Verre Flouré ZrF$_4$ fibre (black) compared to Polymicro FI (dotted).

Bare ZBLAN fibre is more fragile than bare silica fibre. When the fibre is packaged in a acrylate buffer, ZBLAN fibre can be handled just as simply as silica fibre; however, special care may be needed in the handling of the fibre ends, e.g. inserting fibres into ferrules at the fibre array, or into V-grooves at the fibre sit. Lab tests are required to gain experience in handling ZBLAN fibres before this issue can be properly assessed.

The FRD properties of ZBLAN fibre also need to be tested. Differences in the manufacture of the fibre preform mean that that the core/clad diameters of ZBLAN may not be as uniform as those of silica fibres. This may lead to FRD which correlates with fibre length, or which varies with the core/cladding diameters.

Tests made at Le Verre Flouré for the SPirou instrument, using a 90/150 µm fibre, measured losses of ≈15% due to FRD at λ=2.5 µm, when injecting at f/4. Assuming the output of the fibre is a filled top hat this equates to an increase in the beam speed to ≈ f/3.7. At shorter wavelengths the losses due to FRD are smaller, dropping to ≈ 11% at 1 µm.

We note that both the SPirou project and the OHANA project are using ZBLAN fibre from Le Verre Flouré. The former project requires very similar fibres to those needed for ULTIMATE; 30 m length, ≈ 30 µm core diameter.

The cost of ZBLAN fibres is likely to be much more expensive than silica fibres. A single hermetically sealed 30 m patch-cord is 4948 Euro; large quantities will be cheaper, and bare fibre will be cheaper still. Therefore we estimate the total for 13 IFUs, with 61 fibres each, of length 30m to be between $1.3 and $5 million, most probably closer to the lower figure for this quantity of fibre, though this number is highly uncertain. This high cost would probably require a different design, such that smaller lengths of fibre can be used. It is also not clear if Le Verre Flouré have the capabilities for making such large quantities of fibre.

In summary K band fibres appear to be very promising, but laboratory tests are necessary to gain experience and understanding of their properties.

4.4.2   Conduit and Furcation tubes

The fibres will be protected in a series of different housings. The fibres themselves will have a protective acrylate jacket; furcation tubes will protect groups of 30 - 40 fibres; the furcation tubes will be protected in a conduit. Both the individual furcation tubes and the conduit must not be more than ≈50% full, so as not to place unnecessary stress on the fibres during bends etc.

4.4.2.1 Furcation tubes

The ULTIMATE slit will be composed of slitlets with 30- 40 fibres each (see section 4.4.3) We will therefore house each group of 30-40 fibres from an individual slitlet in an individual furcation tube.

The furcation tubes must be large enough that the fibres take up no more than 50% of the cross-sectional area. For a fibre with a buffer of outer diameter 200 μm, the diameter of furcation tubes must be at least 1550 – 1790 μm. FT38 furcation tubing with an inner diameter of 1.8 mm meets this criterion, and can be used for ULTIMATE. This furcation tubing has an outer diameter of 3.8mm on the outer sheathing which is strengthened with Kevlar strands, and was used for the KOALA instrument.

4.4.2.2 Conduit

The furcation tubes will be protected in a conduit. One possibility is a Triflex TRC 60 conduit. The AAO has good experience using this exact type of conduit with the AAOmega and KOALA fibre cables. Figure 28 shows cross-section diagrams of the Triflex TRC series of conduits. A TRC.40 cable with 20 FT38 furcation tubes has a filling ratio of 0.3, meeting the criterion of less than 50%.
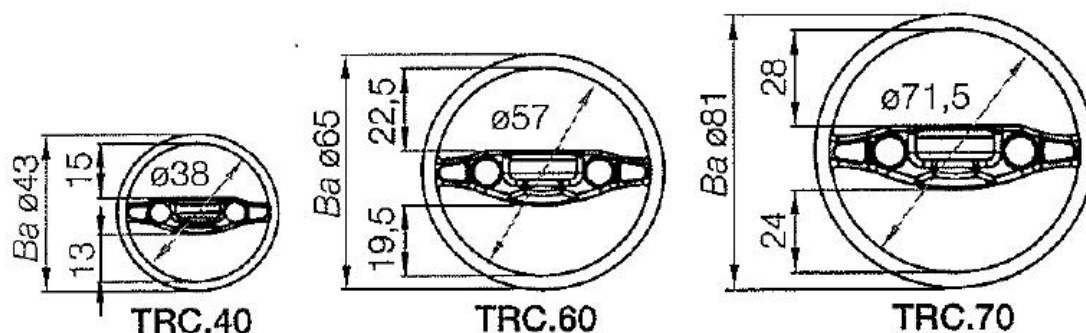

Figure 28. Cross-section diagrams of the Triflex TRC series conduits. KOALA will use TRC 60.

4.4.3   Slit Unit

The purpose of the slit unit is to align the fibres with the MOIRCS entrance slit, and to convert the output back to an f/12.4 telecentric beam.   The slit relay optics magnifies the fibre core from fibre slit to the aperture mask, then the spectrograph optics de-

magnifies the mask image so that each fibre is matched to 2 pixels on the MOIRCS CCD assuming 18 micron square pixels.

The slit unit will consist of a number of identical slitlets, each containing 30 – 40 fibres, each of which feeds its own set of reimaging optics; see Figure 29. Each set of slit lenses is designed for a single spectrograph channel. The entire slit unit will be housed in the MOIRCS fore-dewar, which the fibres enter via a vacuum feed-through. This will minimise thermal emission from the slit blocks and relay optics.
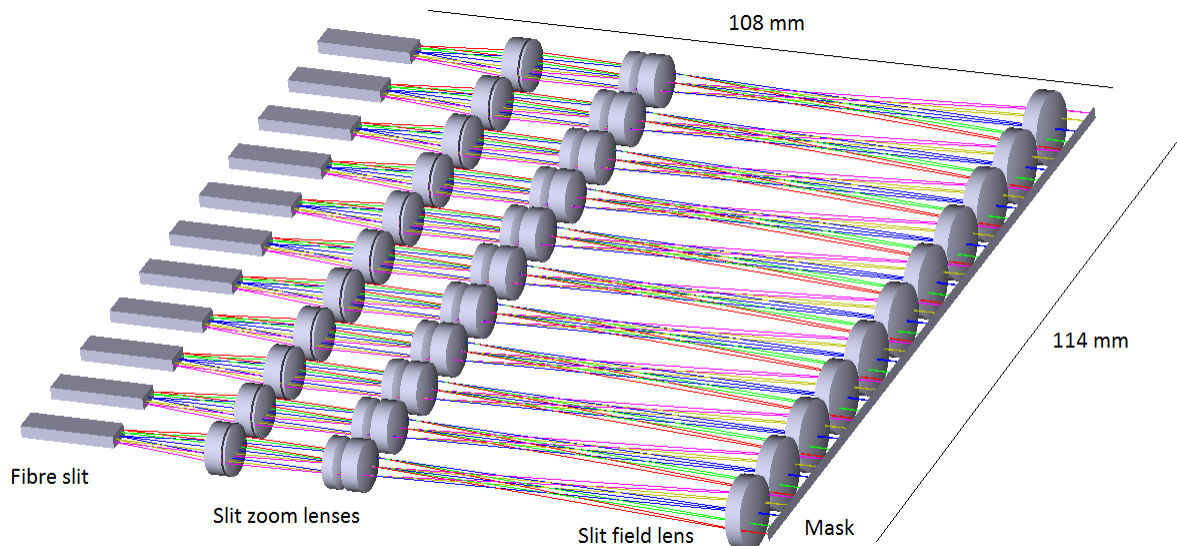
Figure 29. The slit unit.

The slitlet reimaging lenses (zoom lenses and field lens) are mounted into a block of V-grooves. All the fibre slitlets and all lenses will be bonded to the slit block using cryogenic compatible glue.

The output of the fibres is reimaged onto a mask which follows the curvature of the focal surface of the Subaru telescope (~2425 mm convex toward the spectrograph). The mask is then reimaged onto the collimator via two fold mirrors, see Figure 30. The image in the aperture of the mask is oriented along the spatial direction of MOIRCS spectrograph above the roof mirror. The arrangement for the second MOIRCS channel is symmetric with respect to the axis of symmetry (red). Table 12 lists the parameters for the slit relay optics.

Table 12. Parameters for the slit relay optics.

Spectral element at the mask	0.11 mm
Magnification	3.1x
Image quality, center/edge of slitlet	0.04/0.55 waves PV at 1 micron
	0.13/0.38 waves PV at 1.4 micron
	0.13/0.30 waves PV at 1.7 micron

Pupil stop diameter	5 mm
Fibre to fibre cladding clearance	2 micron
Slit optics spatial envelope, excluding lenslets	108 mm x 114 mm x Ø11 mm
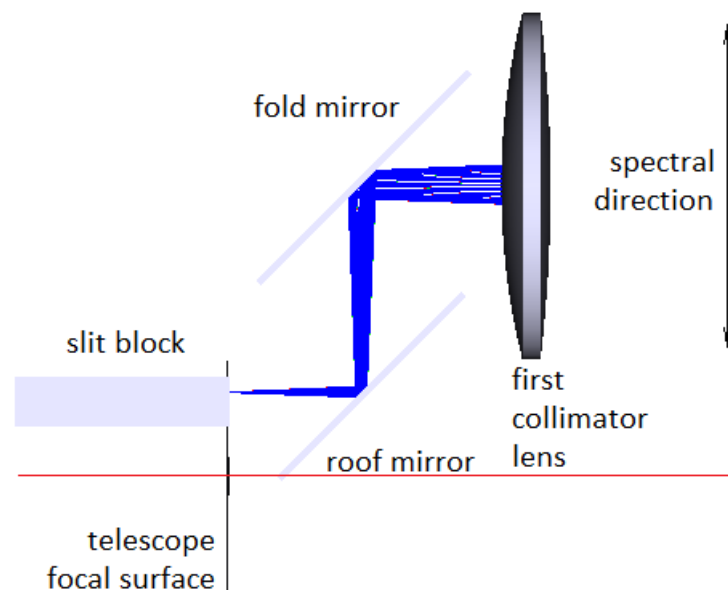
Figure 30. The reimaging mirrors after the slit unit.

Note, that there are different options for the slit relay design. An even more compact layout will result from the use of a linear microlens array over the fibre array in a way similar to injection of light in the Starbugs IFU. However, this approach carries more risk, due to the fact that bonding agent between the fibre array and microlens must maintain optical properties at cryogenic conditions, and shrinkage must be acceptable such that mutual alignment between the two arrays is within tight tolerance (3 microns). The microlens based design would require prototyping the spectrograph slit, which can be undertaken if compactness of the slit block is required. Total throughput gain would be only 2.5%.

A less compact design consists in the use of a custom lens to magnify the entire linear slit by the factor of 3.1 to yield the MOIRCS input F/12.4 beam similar to the proposed V-grooved design. This approach requires longer projection distances and it can be pursued at a later stage with complete opto-mechanical model of MOIRCS spectrograph slit area.

Note that these different slit designs can use either a vacuum feed-through for the fibres, or can image through the existing MOIRCS window, if it is required to leave the current

MOIRCS dewar unchanged. In the latter case prototyping will be required to show that the thermal emission from the slit unit is not significant.

4.4.3.1 Contamination from adjacent fibres

The contamination of adjacent fibre traces depends on the point spread function of the spectrograph. To accurately specify the requirements for the slit of ULTIMATE requires a precise measurement of its PSF. For now we will adopt the measured point spread function of AAOmega. This is well fit by the addition of a Gaussian and a Lorentzian function (Ellis & Bland-Hawthorn, 2008),

$$I(\lambda, \lambda_0, \sigma) = I_0 \left(A \times \frac{e^{-\frac{(\lambda - \lambda_0)^2}{2\sigma^2}}}{\sqrt{2\pi}\sigma} + (1 - A) \times \frac{f\sigma\sqrt{2\ln 2}}{\pi\left((\lambda - \lambda_0)^2 + 2f^2\sigma^2\ln 2\right)} \right),$$

where the power in the Gaussian, $A = 0.97$, and the Lorentzian FWHM is a factor $f = 5.5$ times the FWHM of the Gaussian, see Figure 31.

Using this fit we may estimate the contamination from adjacent spectra. We assume that the PSF of MOIRCS is symmetric, and that the FWHM of the Gaussian is directly proportional to the fibre core size, and the separation between the fibre traces on the detector is directly proportional to the fibre spacing along the slit, with the same constant of proportionality. Thus the contamination from adjacent fibres may be found by integrating over a particular fibres trace, i.e.,

$$\text{cross-talk} = \frac{\int_{-s/2}^{s/2} I(\lambda, 0, \sigma_f)\mathrm{d}\lambda}{\int_{-s/2}^{s/2} I(\lambda, s, \sigma_f)\mathrm{d}\lambda},$$

where s is the fibre spacing on the slit, and σ_f is $d/(2\sqrt{2\ln 2})$, and d is the fibre core size. For a core size of $d = 35$ μm, we show the cross-talk for adjacent fibres as a function of separation along the slit in Figure 32; also shown is the cross-talk between next-nearest neighbours. For fibres spaced more than 80 μm, the cross-talk is below 1%. For next nearest neighbours the cross-talk is always below 0.4%. The signal from each fibre can be de-convolved. Therefore a minimum spacing of 80 μm is adopted. The total possible number of Starbugs as a function of fibre spacing along the slit is given in Table 13. The total number of spectral elements was calculated based on the continuous coverage of the CCD in the spatial direction. There will be some gaps between the slit V-groove channels, to be determined in the next stage of detailed design. We adopt 13 Starbugs as the default number based on these considerations.
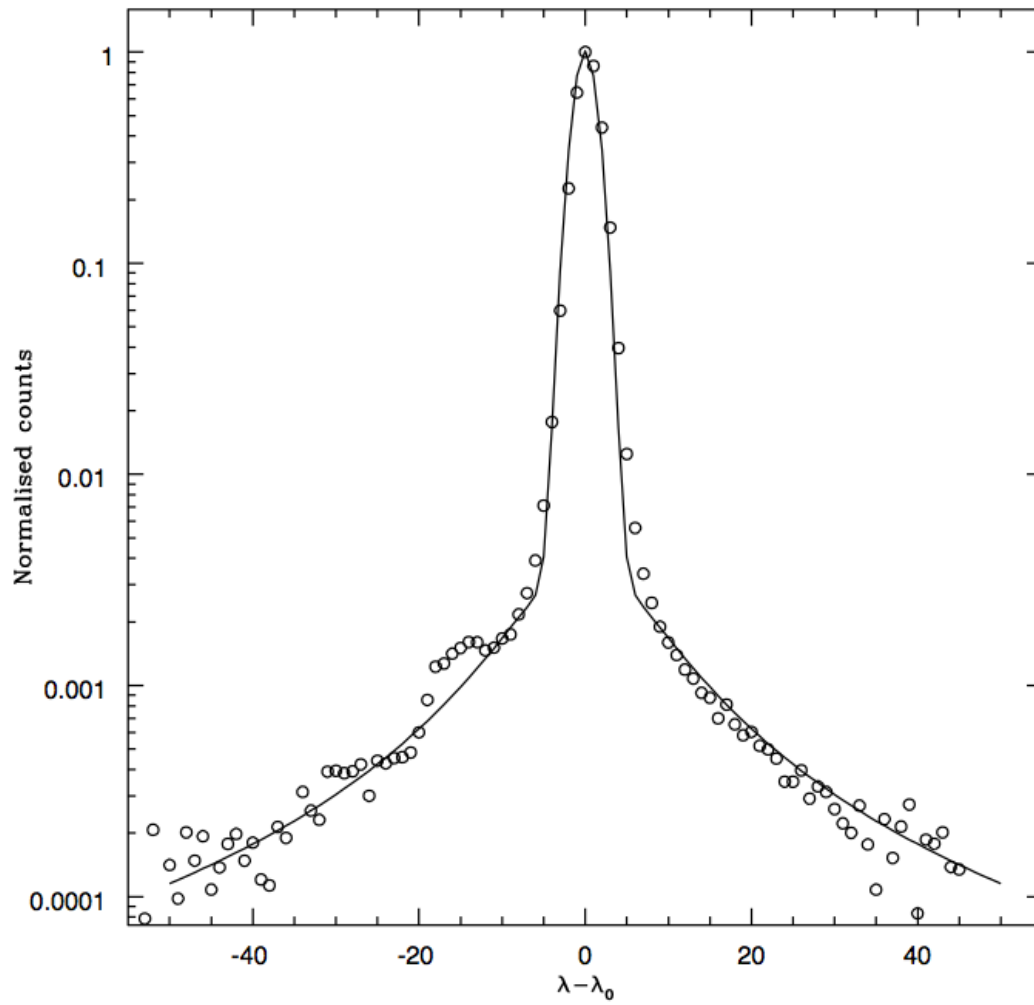
Figure 31. An arc line observed with AAOmega and the best fitting function as given by the equation above, with $A = 0.97$ and $f = 5.5$.
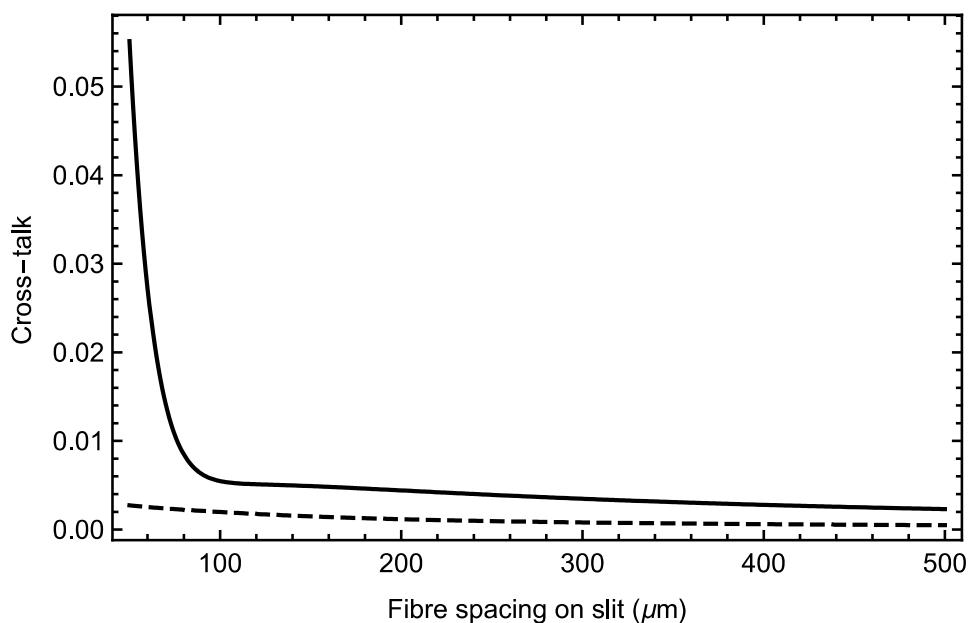
Figure 32. The cross-talk due to adjacent, and next-nearest neighbour fibres of 35 μm core diameter, as a function of spacing along the slit.

Table 13. The separation of fibres along the slit, their spacing across the detector, and the total number of Starbugs possible as a function of fibre cladding diameter.

| Cladding diameter	Spectral element separation		Total amount of spectral elements on both 2K x 2K CCD's	Total amount of 61 element Starbug units
	Mask	CCD		
70 μm	0.223 mm	4 pixels	1024	16
88 μm	0.279 mm	5 pixels	819	13
106 μm	0.335 mm	6 pixels	682	11
124 μm	0.391 mm	7 pixels	585	9
K band fibre 150 μm	0.471 mm	8.4 pixels	488	8

5 PERFORMANCE MODELLING

5.1 Throughput

We have modelled or estimated the throughput from each component of ULTIMATE. Where possible this is done as a function of wavelength. Here we briefly describe our assumptions and give the results.

5.1.1 Primary and secondary mirrors

The primary mirror is coated in Al; the secondary mirror is coated in Ag. The reflectances as functions of wavelength are shown in Figure 33.
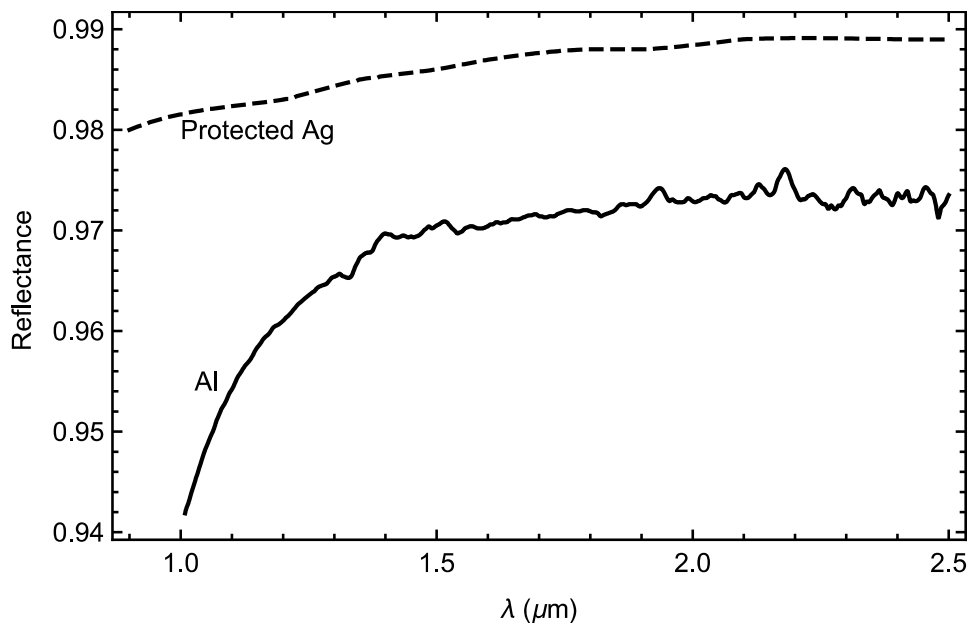
Figure 33. Reflectance of Al and protected Ag mirror coatings as a function of wavelength.

5.1.2 Wide field corrector

The WFC has 6 air-glass surfaces. Each of these will be coated with a broad-band anti-reflection coating, expected to give a reflectance of ≈ 0.3 % across all wavelengths of interest. Therefore the transmission of the WFC will be ≈ 98.2 %.

5.1.3 Fore optics

The fore optics have 2 air-glass surfaces. Each of these will be coated with a broad-band anti-reflection coating, expected to give a reflectance of ≈ 0.3 % across all wavelengths of interest. Therefore the transmission of the fore-optics will be ≈ 99.4 %.

5.1.4 Microlens array

The microlens array has only 1 air-glass surface, coated with a broad-band anti-reflection coating, expected to give a reflectance of ≈ 0.3 % across all wavelengths of interest. The fill factor of the KOALA arrays was measured to be 0.92. Therefore the transmission of the microlens array will be ≈ 99.7 %.

5.1.5 Fibres

The fibres will be approximately 30m in length. The transmission of 30 m of Polymicro FI, and 30 m of Le Verre Flouré ZBLAN fibre is shown in Figure 34.
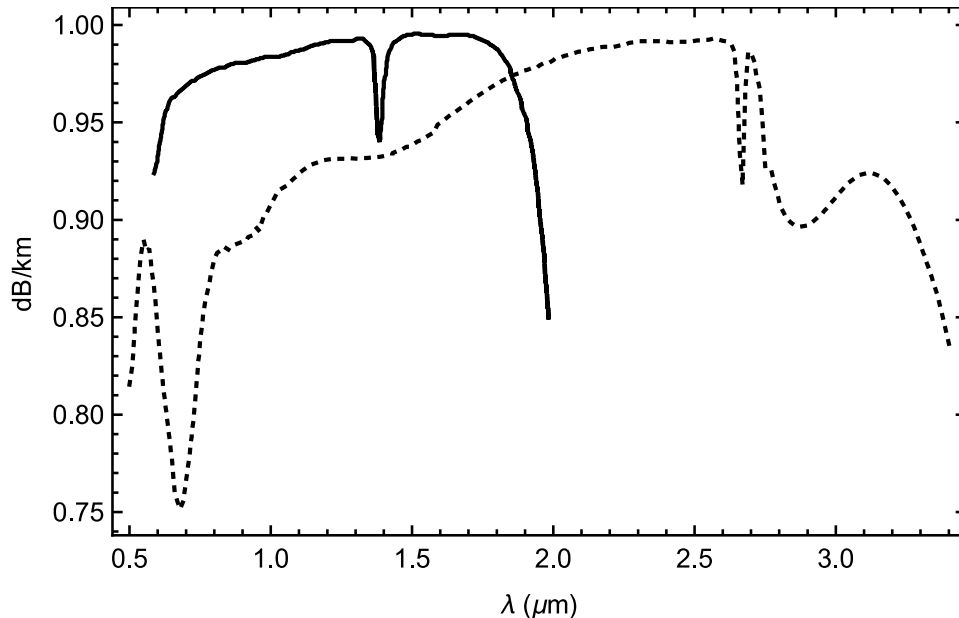

Figure 34. Transmission of 30m of Polymicro FI (black) and 30m of LVF ZBLAN (dotted).

5.1.6 Slit unit

The fibre slit unit has 11 air-glass surfaces, including the ends of the fibres themselves. Each of these surfaces will be coated with a broad-band anti-reflection coating, expected to give a reflectance of $\approx$ 0.3 % across all wavelengths of interest. Therefore the transmission of the fore-optics will be $\approx$ 80.0 %.

5.1.7 Spectrograph

MOIRCS is undergoing an upgrade, called nuMOIRCS, which will replace the grisms with VPH gratings and the detector with a Hawaii-2RG. The VPH gratings should result in a significant improvement of the throughput of the spectrograph. The detector upgrade will result in a significant reduction of the detector noise.

A presentation by Yosuke Minowa gives an estimate of the throughput of nuMOIRCS to be 15%, 20% and 26% in the J, H and K bands respectively.

The QE of the Hawaii-2RG is expected to be approximately 80%.

5.1.8 Total throughput

Figure shows the cumulative throughput after each component as a function of wavelength. The final total throughputs at 1.2, 1.6 and 2.2 μm are given in Table 14. We give the throughputs for both the standard fibre and for the K band fibre.
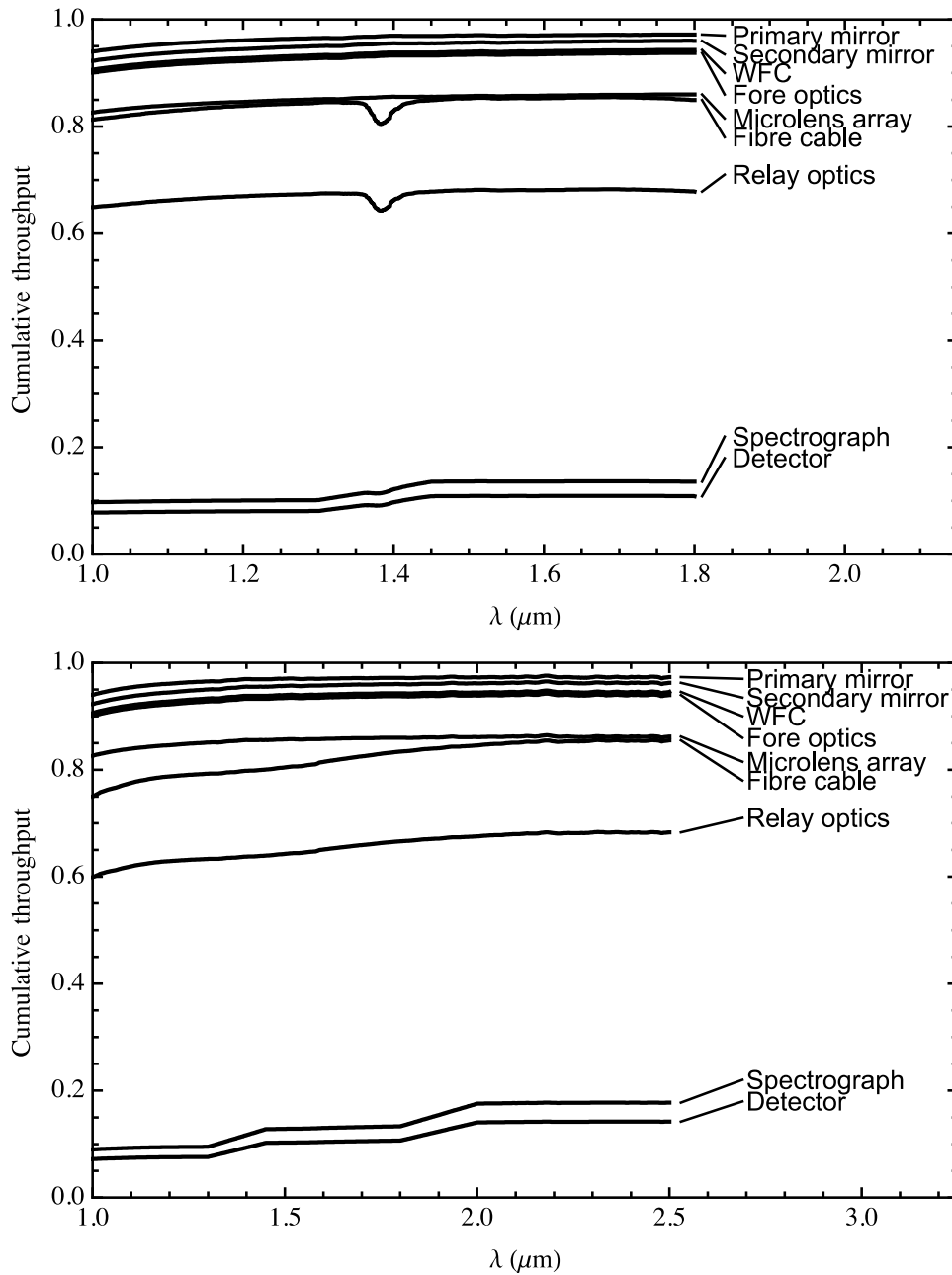
Figure 35. The cumulative throughput after each component of the optical train. The top panel is for the standard silica fibres; the bottom panel shows the throughput using the ZBLAN K band fibres.

Table 14. The total throughput of the telescope + ULTIMATE + nuMOIRCS, for both standard silica fibre and the K band ZBLAN fibre.

Wavelength (μm)	Silica fibre %	ZBLAN fibre %
1.2	9	8
1.6	12	11
2.2	0	15

5.2 Thermal model

ULTIMATE contains many optical elements which are not cooled, including the WFC, the fore-optics, the IFU and the fibre cable. It is important to characterise the thermal emission from these components to enable accurate sensitivity models. In this section we describe the thermal model and the resulting recommendations on the design.

We assume each component of the instrument emits black body radiation, characterised by a temperature, T, and an emissivity, ε; thus the emission in ph s^{-1} m^{-2} arcsec^{-2} μm^{-1} is given by

$$B = \frac{1.41 \times 10^{16} \varepsilon}{\lambda^4 \left(e^{14387.70 / \lambda T} - 1 \right)},$$

where λ is in units of μm, and T is in K.

The emission from each component is multiplied by the throughput of each component down stream, and by the limiting AΩ product of all the down-stream components. The AΩ product is the collecting area of each component multiplied by the solid angle accepted by it, e.g. for an optical fibre the collecting area is determined by the core diameter, and the solid angle by the NA of the fibre. By "limiting AΩ product" we mean the smallest AΩ product of those down stream components which accept the light from the component in question. E.g., the next component after the microlens is the fibre, which accepts a large AΩ from the emission from the microlens; but the AΩ of the emission from the microlenses is actually limited by the pupil stop in the relay optics, hence this is the limiting AΩ product.

In this way the resulting thermal spectrum arriving at the detector, in ph s^{-1} μm^{-1}, of each component is found. Furthermore, dominant components can be identified, and if possible their emissivity or temperature can be controlled to minimise the emission from them.

5.2.1 Emissivities

The emissivity of each component is taken to be

$\varepsilon = 1 - R - \eta,$

where R is the reflectance and η is the throughput of each. Where possible the emissivity is modelled as a function of wavelength. Hence the emissivities are simply one minus the throughputs described in section 5.1. The resulting spectra from each component are shown in
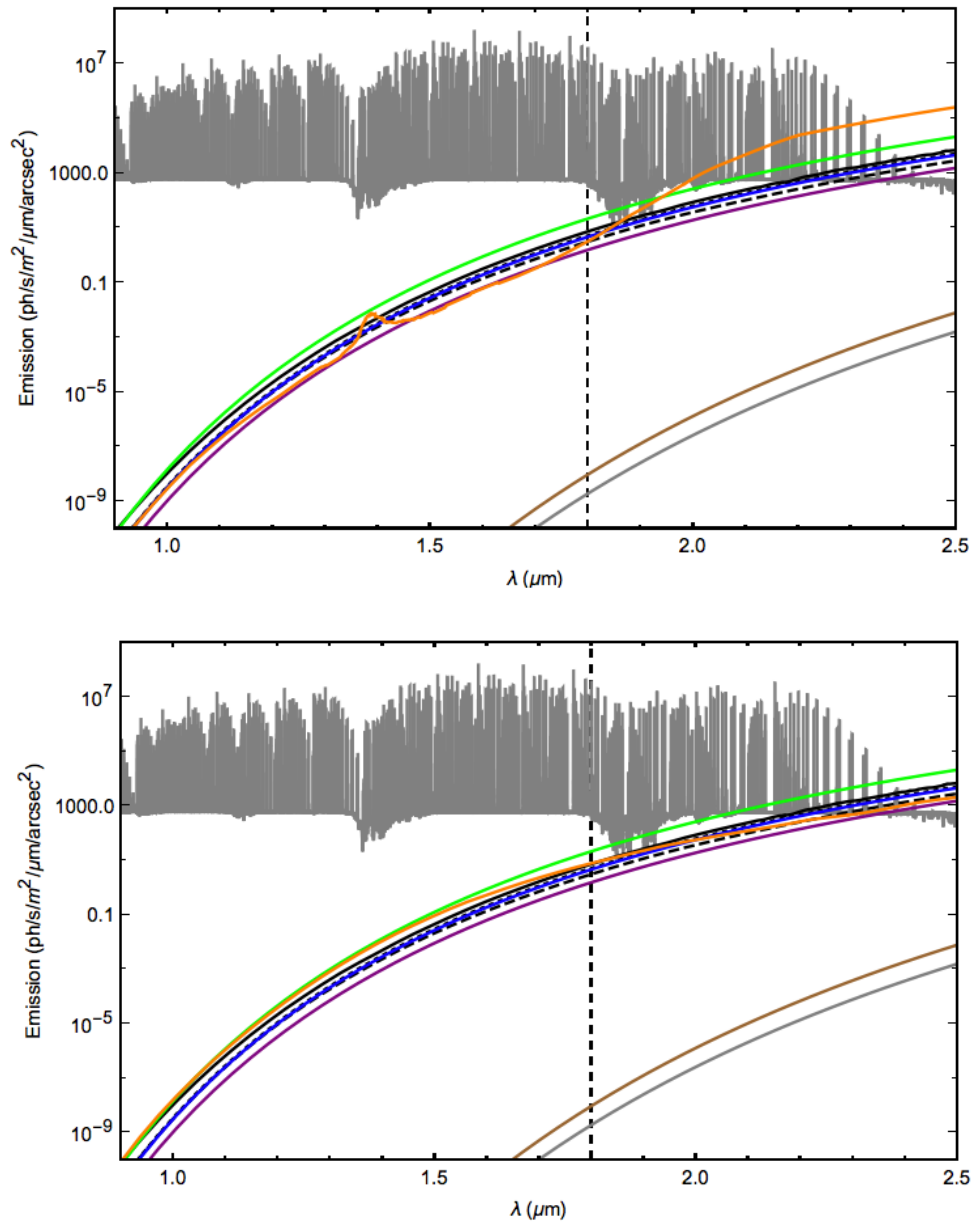
Figure 36. The thermal emission from each component; primary mirror (black), secondary mirror (dashed), cold-stop (dotted), wide-field corrector (blue), fore-optics (purple), IFU (green), fibres (orange), relay optics (grey), mask (brown, this is the emission which will occur out of the beam, between the fibre traces). For comparison the sky emission is shown in grey. The top plot is for standard fibres, the bottom plot is for ZBLAN fibres.

5.2.2 Etendue

Table lists the collecting area of each component and the solid angle which each component sees.

**Table 15. The AΩ product of each component of the optical train**

Component	A (m^2)	Ω(arcsec^2)	AΩ(m^2 arcsec^2)	Notes
Primary	45.5	0.019	0.887	Accounts for central obstruction. Ω is the solid angle on the sky subtended by each element of the IFU.
Central obstruction	7.3	0.019	0.142	Emission from here should be completely blocked by the stop (excluding the spider vanes).
Secondary	52.8	0.019	1.029	
WFC	52.8	0.019	1.029	
Fore optics			0.887	AΩ is defined by a stop which only accepts light from the unobscured mirror.
Cold stop			0.142	AΩ is defined by a stop which blocks the light from the central obstruction.
IFU	5.41×10^{-8}	1.78×10^{7}	0.965	
Fibres	9.62×10^{-10}	2.10×10^{9}	2.018	Fibres are oversized to allow for pupil misalignment.
Relay optics			2.018	AΩ is defined by a stop to limit the output of the fibres to f/4.

Thus emission from all components upstream of the fore-optics is limited by the AΩ of the pupil stop in the fore optics; likewise, emission from all components downstream of the fore-optics all emission is limited by the stop in the relay optics.

5.2.3 Thermal background

Taking into account the AΩ etendue and the throughput of the down-stream components, we have calculated the thermal background at the detector. Figure shows the thermal background for each component.
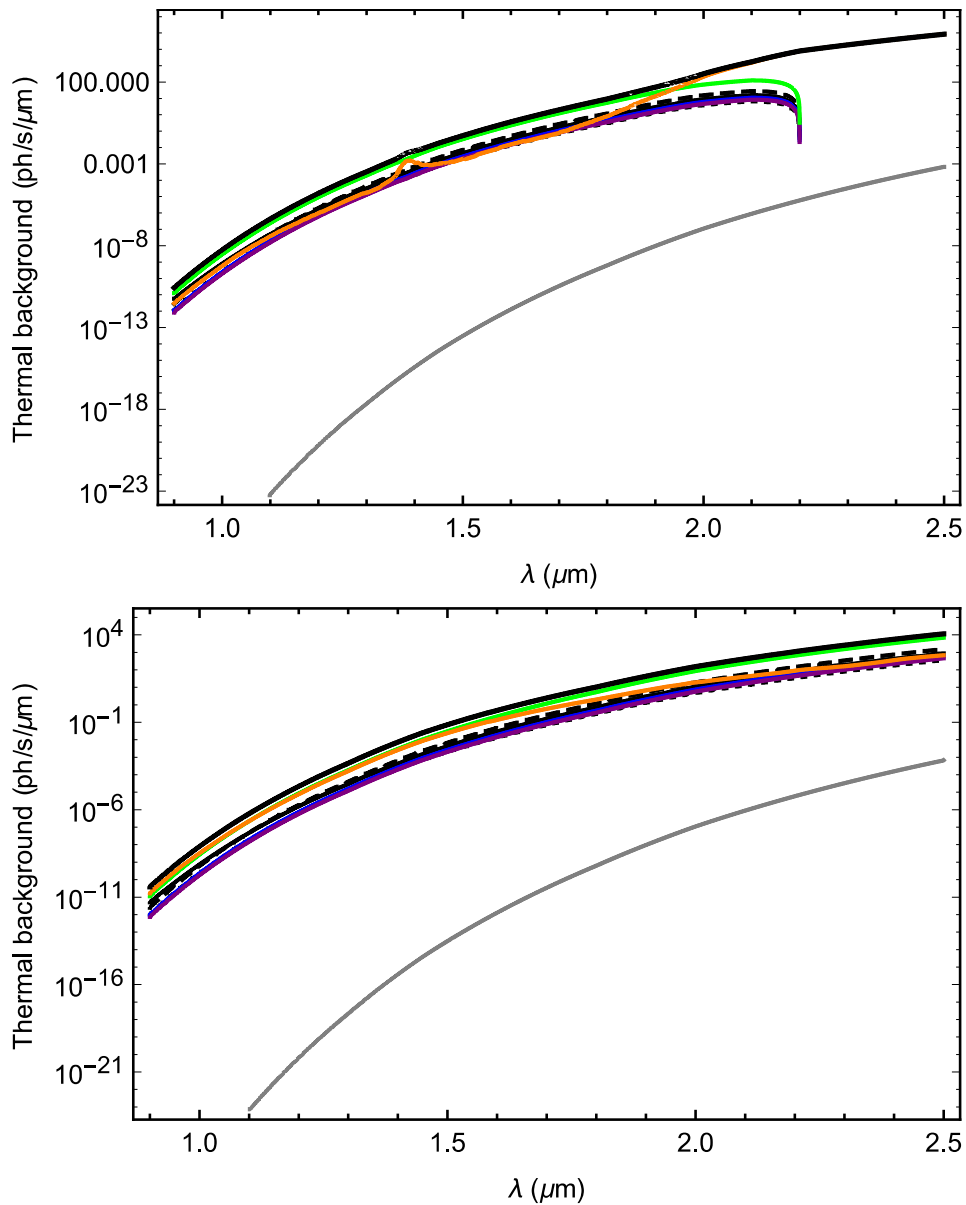
Figure 37. The thermal background at the detector in ph/s/μm from each component; primary mirror (black), secondary mirror (dashed), cold-stop (dotted), wide-field corrector (blue), fore-optics (purple), IFU (green), fibres (orange), relay optics (grey). The total thermal background is shown by the thick black line. The top plot is for standard fibres, the bottom plot is for ZBLAN fibres.

5.3 Stray-light analysis

The low emissivity coating of the fore-optics reduces the thermal background, but may increase the stray-light entering the fibre face, due to the high reflectivity. We have analysed the amount of stray-light entering the face using ray-tracing all all the light emitted in a 2 π steradian hemisphere, as shown Figure 38.

The AΩ product of all light incident on the fibre face is 4.1 m^2 arcsec^2. However, only 0.082 m^2 arcsec^2 is within the acceptance cone of the fibre NA, and only 0.002 m^2 arcsec^2 is within the science beam; the remainder will be rejected by the pupil stop in the fibre slit relay optics. This should be comapared to the science beam from M2, which has an AΩ product of 0.96 m^2 arcsec^2. If we assume that all the stray light is thermal in origin, with an emissivity of 1, then taken together with the M2 thermal light with an emissivity of 0.015, the stray-light contributes 12 % of the thermal emission from M2.
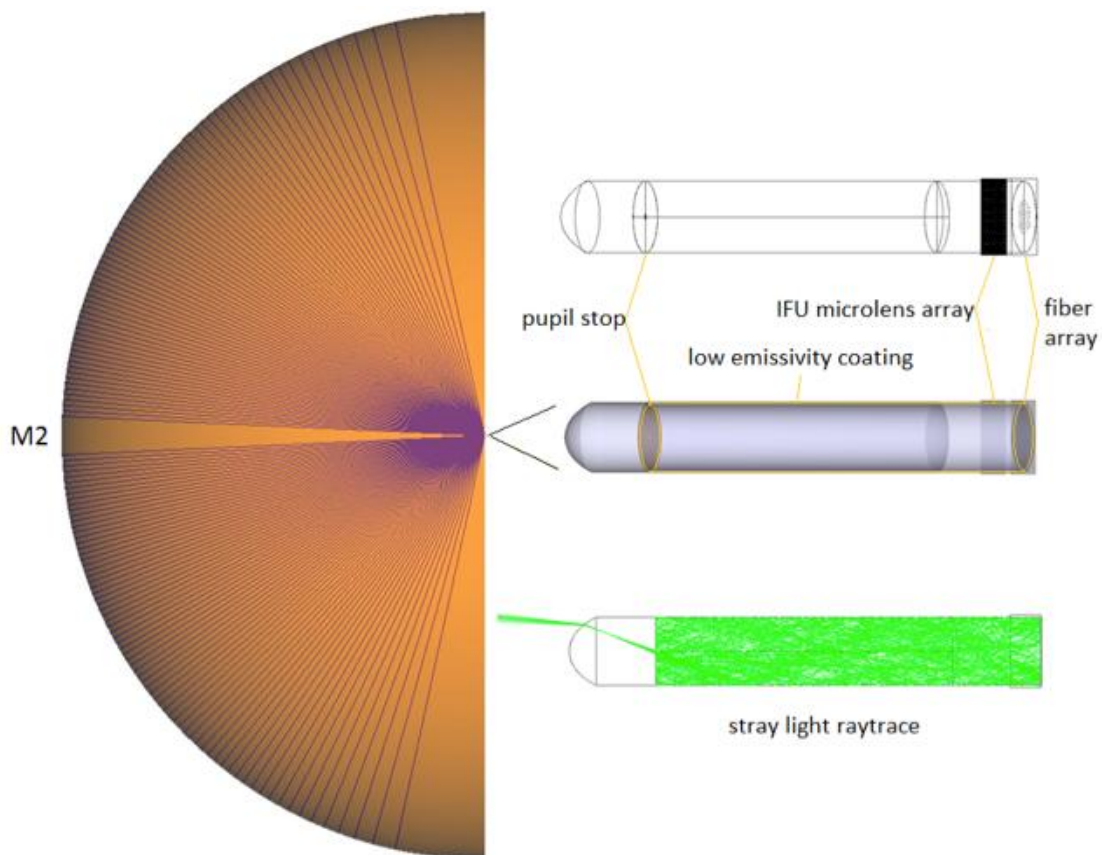
Figure 38. Ray-tracing diagram of the stray-light analysis for all light entering the fibre face.

5.4 Sensitivity

5.4.1 Background

The background emission for ULTIMATE observations will consist of three broad components, viz., the sky (including atmospheric emission and astronomical emission), the thermal emission of the instrument (discussed in section 5.2), and detector noise.

The thermal emission has been discussed in detail above. We will now briefly review our assumptions for the sky emission and the detector emission.

5.4.1.1 Sky background

The sky background consists of the atmospheric emission lines, mainly from OH, the zodiacal scattered light, and an unidentified interline component. Other contributions, e.g., scattered moonlight, are negligible.

We have modelled the OH emission using the atlas of Rousselot (2000), with the line strengths calibrated to the observations of Maihara (1993). The zodiacal scattered light is modelled from the COBE DIRBE observations of Kelsall (1998). For more details see Ellis & Bland-Hawthorn (2008).

In addition to the model of Ellis & Bland-Hawthorn (2008) we include an as yet unidentified interline component of $\approx$ 560 ph/s/m^2/µm/arsec^2 , such that the total interline continuum including the ZSL matches the canonical measurement of Maihara (1993).

5.4.1.2 Detector emission

ULTIMATE will use the upgraded nuMOIRCS incorporating a Hawaii-2RG detector with ASIC sidecar controller. The dark current for such detectors is expected to be < 0.01 e-/pix. The effective readout noise using Fowler or up-the-ramp sampling is expected to be $\approx$ 4 e-/pix.

5.4.1.3 Total background

We have calculated the total background counts per pixel per second for J and H band observations assuming spectral resolving powers of R = 3000 and that the FWHM is sampled by 2.5 pix. Figure 39 shows the components and total background; in addition there will be a read out noise of be $\approx$ 4 e-/pix, assuming Fowler or up-the-ramp sampling.
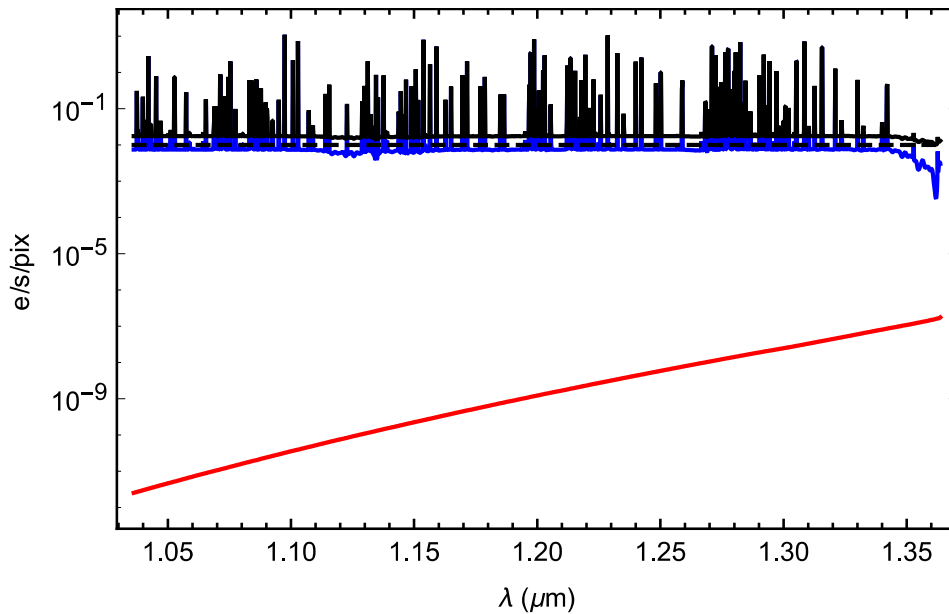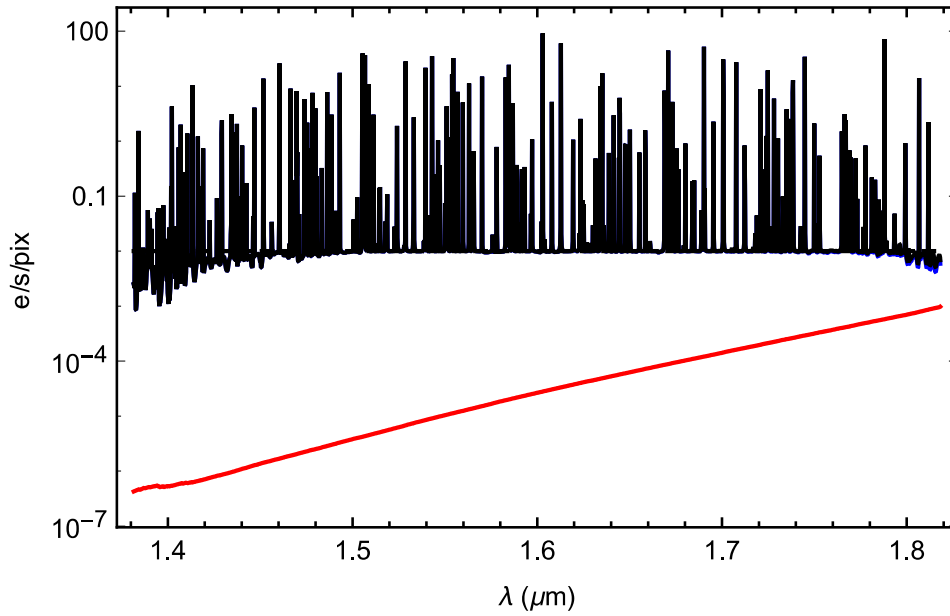
Figure 39. The ULTIMATE background in the J band (top) and H band (bottom). The black line shows the total background; the components are shown by blue for the sky, red for the instrument thermal background, and dashed line for the detector dark current. In addition to these noise sources there will also be a read out noise of 4 e-/ pix for a Fowler (or up-the-ramp) sampled image.

5.4.2 Target surface brightnesses

One of the primary science cases of ULTIMATE requires the detection of emission lines in the discs of galaxies at redshifts $0.4 < z < 1.7$. Assuming the Kennicutt (1998) relations between star-formation rate and Hα luminosity, we have calculated the surface brightness of the Hα line as a function of redshift for star-formations rates of 3, 10 and 30 $M_\odot$ yr^{-1}, assuming that the emission is uniformly distributed over a disc 8 kpc in radius. Figure 40 shows the resulting surface brightnesses.
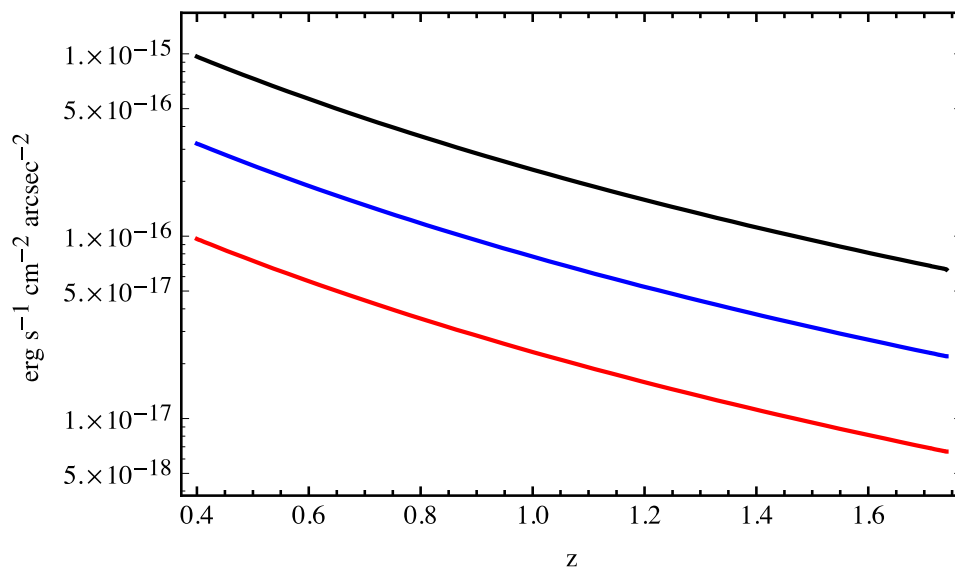
Figure 40. The surface brightness of the Hα line assuming a star-formtion rate of 3 (red), 10 (blue) and 30 (black) $M_{\odot}$ yr^{-1}, and that the emission is uniformly distributed over a disc 8 kpc in radius.

5.4.3 Signal-to-noise

We will assume typical surface brightness of targets of 1×10^{-17}, 1×10^{-16}, and 5×10^{-16}, erg s^{-1} cm^{-2} $arcsec^{-2}$ (N.B. we now use a fixed surface brightness, and not a fixed star-formation rate). Further assuming a typical line width of Gaussian FWHM = 0.5 nm, we have calculated the signal-to-noise as a function of time and wavelength. Figure shows the signal to noise per spaxel integrated over the emission line width for 1 hour on source.
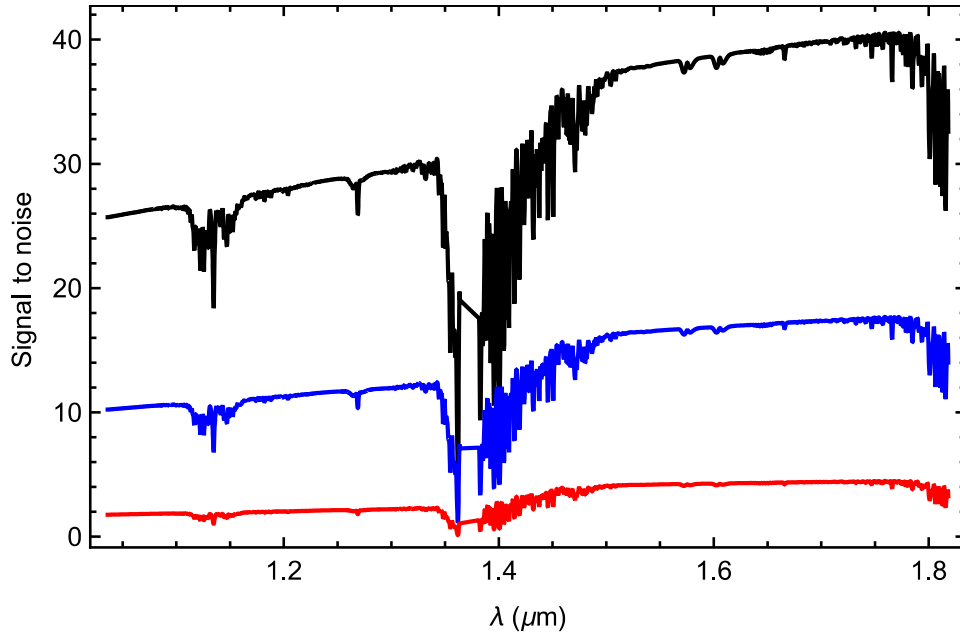
Figure 41. The signal to noise per spaxel in one hour of exposure time on source, integrated over the width of the emission line, for line surface brightnesses of 1×10^{-17} (red), 1×10^{-16} (blue), and 5×10^{-16} (black) erg s^{-1} cm^{-2} $arcsec^{-2}$.

6 CONCEPT DEVELOPMENT AND PROTOTYPING

The next stage of the ULTIMATE project will consist of developing a conceptual design for the whole instrument, and prototyping the critical components of the instrument. Figure 42 shows the preliminary system architecture, within which we have identified the current level of development of each sub-system.

During stage 2 each subsystem will be developed to one of three levels,

1. Conceptual design (C). All sub components will be developed to this level.

2. Test (T). Acceptance tests, and characterisation of components.

3. Prototype (P). One of more prototypes will be built and tested.

Additionally, we will conduct systems engineering, end-to-end modelling and provide documentation for all prototype tests and conceptual designs.

The above tests will all be carried out in the laboratories at AAO. Optional further tests can take place with prototype IFUs on sky,

4. On sky tests at the AAT

5. On sky tests at Subaru.

The level of testing for each subsystem and subcomponent is summarised in Table 16, which also shows an approximate timeline for the completion of the tasks, from when stage 2 begins. The costs associated with the stage 2 developments are given in section 7. In this remainder of this section we describe the tests to be carried out.
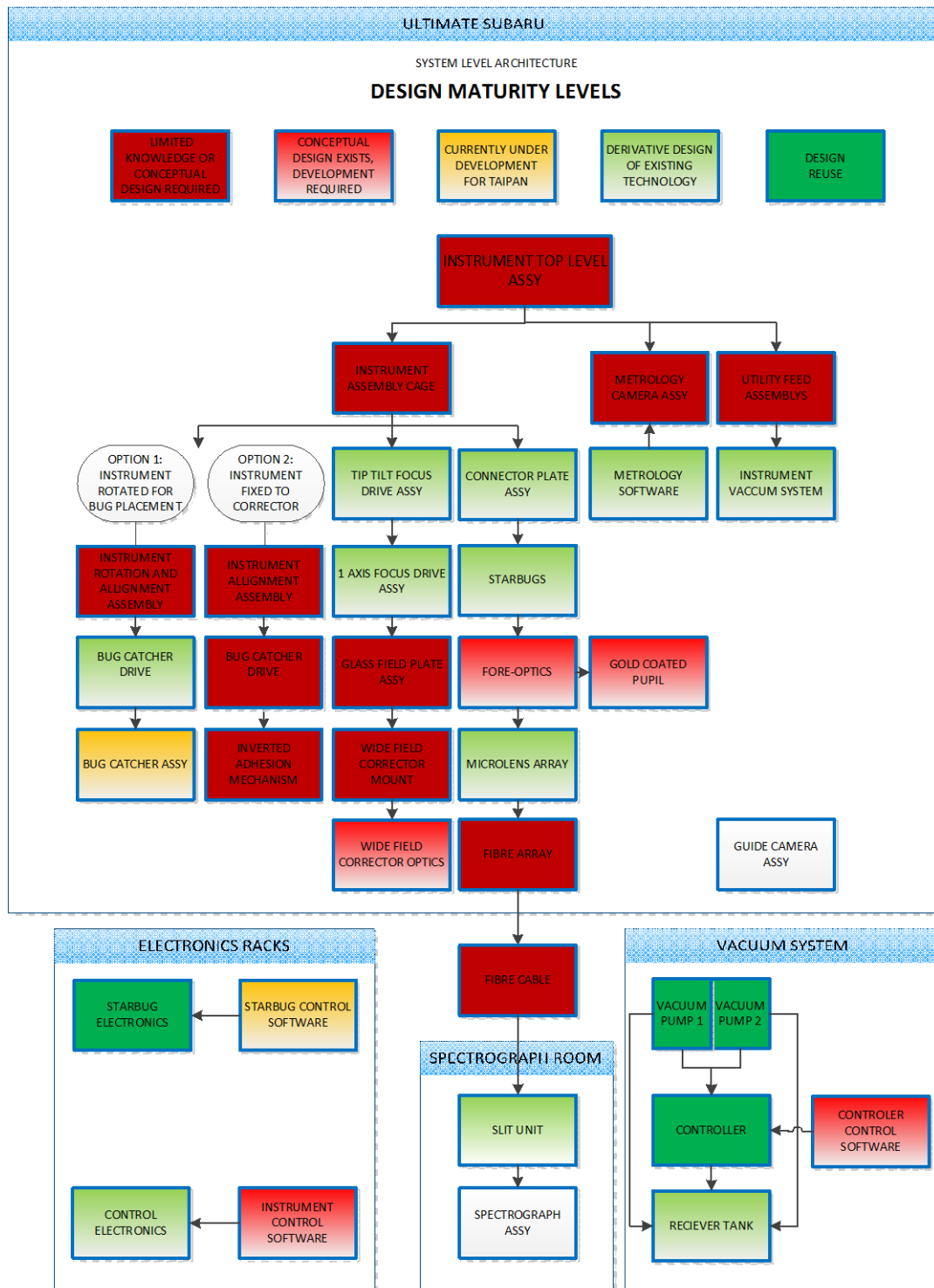
Figure 42. The system architecture and levels of maturity of development of each sub-component.

Table 16. Level of testing for each subsystem and subcomponent, to be carried out during Stage 2, and approximate timeline.

Unit	Sub unit	Level (Concept, Prototype, Test or Write)	Time frame (months) 0	3	6	9	12	15	18	21	24	27
Instrument assembly	Telescope interfaces	C	Concept design									
	Architecture	C	Concept design									
	Possible instrument rotation	C	Concept design									
	Alignment, focus, tip, tilt	C		Concept design								
	Instrument electronics	C			Concept design							
	Instrument control software	C			Concept design							
	Connector plate	C			Concept design							
	Bug catcher	C			Concept design							
	Metrology	C			Concept design							
	Vacuum system	C				Concept design						
WFC	Mount	C				Concept design						
	Corrector optics	C				Concept design						
	Field-plate	C				Concept design						
Starbugs	Starbug assembly	P	Concept design	Procurement		Build	Test					
	Electronics	C				Concept design						
	Control software	C				Concept design						
IFU	Optics	P	Concept design	Procurement		Build	Test		AAT On-Sky To test integrated IFU and fibre cable feeding IRIS2 Separate development needed for IFU mount and slit relay optics		Subaru On-Sky To test integrated IFU and fibre cable feeding MOIRCS Separate development needed for IFU mount and slit relay optics	
	Pupil stop	P	Concept design		Procurement	Build	Test					
	Microlens array	P	Concept design	Procurement		Build	Test					
	Fibre array	P	Concept design	Procurement		Build	Test					
	Integrated IFU and fore-optics assembly	P	Concept design				Build	Test				
Fibre cable	Silica fibres	T	Concept design	Procurement	Test							
	ZBLAN fibres	T	Concept design	Procurement	Test							
	Fibre assembly	C			Concept design							
	Fibre routing	C			Concept design							
	Cabling	C				Concept design						
Slit unit	Spectrograph interface	C	Concept design									
	V-grooves	C				Concept design						
	Relay optics	C				Concept design						
Systems engineering	Modelling	C		Concept design								
	Documentation	W					Write					

6.1 Instrument Assembly

A conceptual design of all components of the instrument assembly will be carried out. No further testing or prototyping of these components will be carried out during stage 2. In particular the concept design will address the following issues.

A conceptual design of the interface between the instrument and the Subaru telescope will be made, including the mechanical housing of the instrument, and the location of the various sub-systems.

The overall system architecture will be concteptualised, building on the outline presented in Figure 42. This will include the concepts for possible rotation of the instrument in order to place the starbugs (see section 6.1.2), the concepts for alignment, focus, and tip/tilt of the instrument, the instrument electronics and the instrument control software.

6.1.1 Connector plate

A conceptual design will be developed for the connector plate. Many aspects of the connector plate can be adopted without change from that of TAIPAN, see section 4.2.3. However, the connector plate for ULTIMATE will require a hole beside each Starbug-plug for the observing fibres to pass through unobstructed. Either the Starbug or the fibre can be changed with the aid of a jig to remove the IFU from the Starbug.

6.1.2 Bug catcher

One of the functions of the bug-catcher is to place the Starbugs onto the field plate when first using the instrument (e.g. after an instrument change). The TAIPAN design places Starbugs onto a curved field plate in a downwards position. Placing Starbugs onto a curved and upwards looking field plate presents some challenges, since after positioning the bugs, the bug-catcher must retract without pulling off the bugs, which is not trivial for a curved field plate.

We will conduct a conceptual design study to determine a solution to this problem. N.B. this problem is also an issue for the MANIFEST instrument, which is currently under development.

Possible solutions include (i) a precisely machined bug catcher which can hold and position the bugs on a curved field plate at the correct angle, and retract without pulling off the bugs, (ii) tumbling the field plate into an inverted position before placing the bugs. This would also require the field plate to be moved away from the wide field corrector prior to tumbling, or to tumble the entire WFC. (iii) Using a flat field plate, such that the bug-catcher can retract without pulling off the bugs, but this would require a new optical design for the WFC. (iv) Placing the bugs onto the field plate by hand; this would only be required to be done once per night.

If possible a prototype for placing a single Starbug onto a curved field plate will be developed during stage 2.

6.1.3 Metrology camera

A concept study will be carried out to determine the metrology system for positioning the Starbugs, including camera type, pixel size, plate-scale etc. This will include the location of the Starbugs metrology camera. If located above the WFC then the camera supports will cause shadowing of the beam, as will the camera itself unless it can be positioned within the secondary mirror shadow. If the camera looks through the WFC, it must be able to correct for the distortions introduced by the WFC. The distance of the camera from the field-plate must be close enough to allow adequate measurement of the Starbugs positions such that they can be positioned accurately. Other options will be determined when sufficient telescope geometry is available.

6.1.4 Vacuum system

A concept design for the vacuum system will be made, concurrently with the prototyping of the Starbugs, the results of which will determine the requirements of the vaccum system (see section 6.3.1).

6.2 Wide field corrector

A conceptual design of all components of the WFC will be carried out. No further testing or prototyping of these components will be carried out during stage 2. In particular the concept design will address the following issues.

The interface of the WFC with the telescope will be conceptualised, along with the mechanical housing. The optical design of the WFC will be developed, if necessary taking into account the sharing of this component between different instruments (see Appendix A).

The interface of the field-plate to the corrector optics will be conceptualised, taking into account the possible need to rotate the field plate into an inverted position to place the Starbugs (section 6.1.2).

6.3 Starbugs

A number of prototype Starbugs will be built and tested as described below. Conceptual designs will be carried out for the Starbugs control electronics and control software.

6.3.1 Vacuum and adherence tests

The ULTIMATE Starbugs differ from the TAIPAN Starbugs in that they have a larger diameter, carry a heavier payload and will operate at a lower atmospheric pressure. Therefore the vacuum necessary to adhere the Starbugs to the field-plate and allow normal operation will be tested.

A Starbug will be loaded with a mass equivalent to that of the ULTIMATE fore-optics and IFU payload and a simulated cable bundle. The vacuum will be reduced so the

pressure differential on the Starbug is always less than 0.5 atm to establish that the Starbug functions satisfactorily for fast movement, rotation and fine positioning. These tests should be repeated for up to eight different prototype bugs, to check for consistency. The tests should be repeated at a range of field plate angles, from fully inverted to horizontal, to simulate different positioning of the telescope. Our existing Starbug test facilities can be used for fully inverted , slewing and horizontal testing, see Figure 43

6.3.2 Payload dock

The mating of the fore-optics and IFU assembly within the payload docking tube will be tested for flexure and movement.
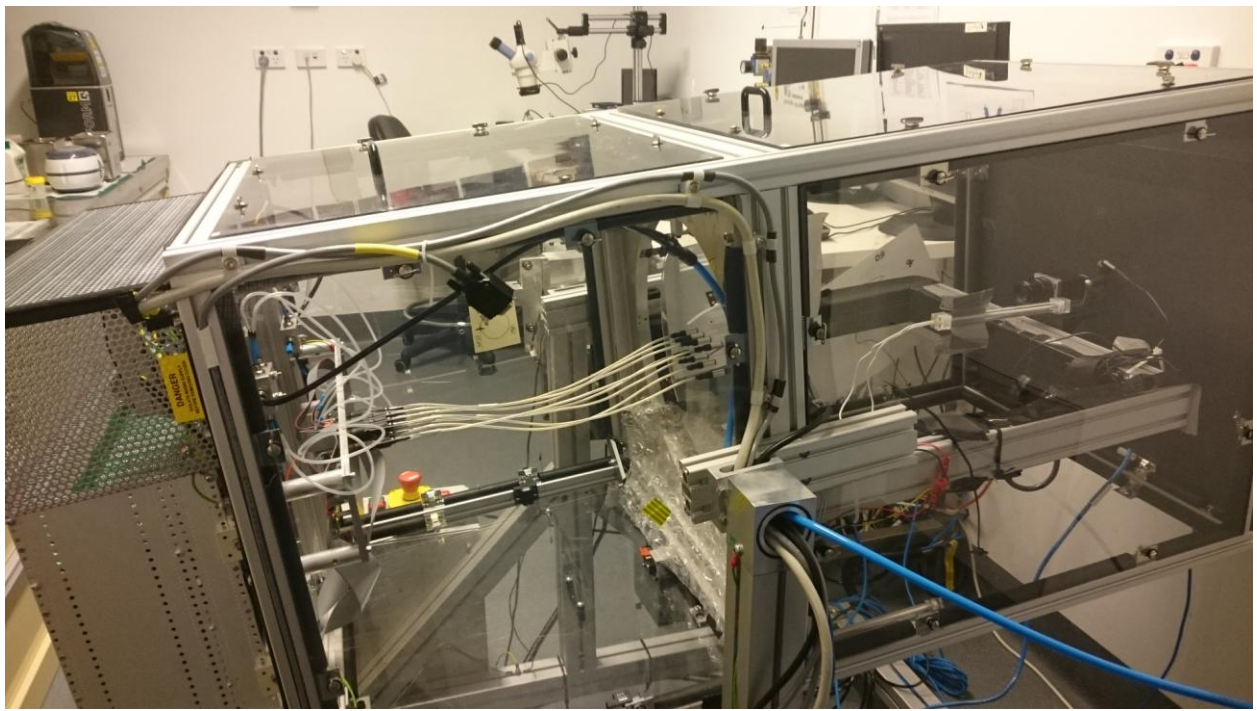

Figure 43. Starbug test facilities at AAO.

6.4 Integral field unit

6.4.1 Fore-optics

The entire fore-optics will be prototyped and assembled with the IFU.

6.4.1.1 Fore-optics tests

The fore-optics lenses will be specified and purchased, and tested for image quality.

6.4.1.2 Assembly

The assembly of the fore-optics within the payload tube will be prototyped to ensure an adequate procedure is found.

6.4.1.3 Pupil stop

The gold-coating of the outside of the fore-optics and the pupil stop will be specified, and prototypes will be made.

The accuracy of the alignment of the pupil stop will be measured.

6.4.1.4 Thermal emission and scattered light

Two sets of fore-optics should be made, one with the gold-coating and one without. The thermal emission and scattered light from both should be measured. It should be ascertained that the gold-coating reduces the overall background of the instrument.

6.4.2 Microlens array

Specifications for the microlens array will be made and prototype arrays will be purchased. The pitch, filling-factor, and pupil coupling from the arrays will be measured. The microlens array will be aligned and assembled with the fibre array to build a prototype IFU.

6.4.3 Fibre array prototype

The IFU is composed a 61 element hexagonally packed microlens array bonded to a fibre array. The fibre array must be precisely matched to the microlens array, and requires accurate fibre to fibre pitch, alignment and tilt.

One option is to subcontract both the manufacture of the fibre array and the assembly of the fibre array to the microlens array to an external company. For example, the IFU for KOALA consisted of a 1000 element hexagonally packed microlens array, for which the fibre array was manufactured and bonded to the microlens array by Fiberguide Industries. Previous experience with the 19 element hexagonal array for GHOST suggests that this option is likely to be expensive (~$30,000 - $50,000 per IFU). Moreover it may be difficult to achieve arrays that are small enough to be housed in a Starbug; the GHOST arrays have only 19 elements, but are physically large, with a sizeable housing surrounding the microlens array; this solution is not acceptable for ULTIMATE, for which the entire package must fit inside the payload tube. Thus, subcontracting the fibre array may also occur significant NRE costs.

During the next phase, specifications will be made, and quotes obtained from manufacturers of fibre arrays to fully explore this option.

A second option is to build the IFU in house. In this case the microlens array and the fibre ferrule would be separate custom orders which would then be aligned and bonded to the fibres at the AAO. The AAO has previous experience aligning and bonding fibres to microlens arrays with GNOSIS and CYCLOPS2.

A solution to the manufacture of the ferrule array is offered by FEMTOprint, who use femtosecond laser printing and chemical etching techniques to make 3D micro-devices in fused silica and other materials. They can manufacture a hexagonally packed array of holes in fused silica at 250 μm pitch to within 1 μm tolerance. However, the depth of the holes can only be 2 - 4 mm long. Therefore either a longer ferrule will be required to

be inserted into each hole, into which the fibres can be inserted afterward, or several 3D printed arrays must be stacked to achieve an adequate depth to hold the fibres. FEMTOprint have provided a quote for a prototype 61 element array at CHF 3650.

Since this particular method of manufacturing a fibre array has not been done before at the AAO, this requires careful prototyping and testing at an early stage. However it offers a potentially cheap and accurate solution.

During the next stage, we will procure prototype arrays, and test the accuracy of the pitch, alignment to the microlens array, and tilt of the fibres within the array.

The pitch of the array will be measured using a Thorlabs 100 μm reference grid overlaid on the array, and imaging the array with a camera. The location of the hole centres can be calibrated using the reference grid. The translation stages of the lithographic equipment used to fabricate the microlens arrays are accurate to 0.1 μm.

The alignment and tilt of the fibres will be tested by backlighting the fibres and testing that the spot falls at the centre of the corresponding microlens.

The procedure for the insertion of the ferrules into the array, and the fibres into ferrules will be tested by building a prototype.

6.4.4 Integrated IFU and fore-optics assembly

The assembly of the IFU with the fore-optics will be prototyped.

The throughput across the full wavelength range will be measured for the Starbug optics assembly taking into account internal transmission, AR coating performance and the filling factor of microlens array.

The magnification lens is design to perform close to diffraction limit. This will be confirmed experimentally. Additionally the method for housing the optics in the docking tube will also be prototyped.

6.5 Fibre cable

6.5.1 Fibre tests

The full fibre cable will not be prototyped, but tests of different fibre types will be carried out in order to determine the best type, in terms of transmission and FRD.

6.5.1.1 Throughput

The transmission of a 30 m length of the fibre cable will be tested as a function of wavelength using the cut-back method.

6.5.1.2 Focal ratio degradation

The FRD losses of a 30m length of fibre fed at f/4 will be measured. Light will injected at f/4. The intensity of the light exiting the fibre will be measured through a wide aperture. The aperture will then be stopped down to f/4 and the intensity re-measured. The resulting losses for an f/4 injection will be calculated from the ratio of the two

measurements. The measurements should be repeated for different wavelengths and different focal ratios.

6.5.1.3 K band fibres

A series of lab tests will be carried out to determine the suitability of the ZBLAN fibres. See section 4.4.1.1 for a discussion of the properties of ZBLAN fibres, and possible issues.

The transmission of the ZBLAN fibres has been measured by LVF. We will repeat these tests ourselves, using the cut-back method. Tests will be carried out on both 90 µm core diameter and 35 µm core diameter fibres.

The FRD of the 90 µm core diameter ZBLAN fibres has been measured by LVF. We will repeat these tests ourselves, using the method outlined in section 6.5.1.2. Tests will be carried out on both 90 µm core diameter and 35 µm core diameter fibres.

The FRD will be measured for the full 30 m length of fibre, and also as a function of length, end face polishing procedures, mounting in ferrules, mounting in V-grooves, temperature. These tests will be repeated for the J, H and K bands.

Throughout these tests we will also determine the suitability of the fibres in terms of their fragility, especially when mounting the fibres into the fibre array and into the slit.

The thermal emission from fibres will be measured, to ascertain the necessary requirements for relaying the slit image to the spectrograph.

6.5.2 Fibre assembly, routing and cabling

Conceptual designs will be carried out for the assembly of the fibre cable, the routing from the instrument to the spectrograph, and the cabling of the fibres. See section 4.4.2 for a discussion of cabling options.

6.6 Slit unit

A concept design will be carried out to determine the interface of the fibre slit with the spectrograph. This will determine whether a vacuum feed-through is necessary to minimise thermal emission from the slit, or whether the fibres can be imaged through the MOIRCS deware window. The necessary relay optics will be designed.

Additionally the concept design will address the packing of the fibres along the V-groove, in order to minimise FRD, minimise fibre-to-fibre contamination, and maximise the number of fibres.

6.7 Systems engineering

In addition to the concept designs and prototype tests described above will we carry out systems engineering to model the end-to-end performance of ULTIMATE. Stage 2 will also include complete documentation of all concept designs and prototyping results.

6.8 On-sky tests

If required, on-sky tests can be carried out to provide a proof-of-concept IFU fibre feed for a NIR spectrograph. These tests would employ a single IFU feeding a spectrograph. These tests would not employ Starbugs positioners; the interfacing of Starbugs on the telescope lie outside the scope and time frame of the stage 2 prototyping tests.

6.8.1 AAT tests

Tests could be carried out at the AAT, feeding either the existing IRIS2 spectrograph, or the PRAXIS spectrograph which is currently under construction. PRAXIS would offer the advantage of a cryogenic vacuum feed through for the slit, an efficient VPH based spectrograph, and a Hawaii-2RG detector, but observations would be limited to wavelengths of 1.47 – 1.7 µm.

Feeding IRIS2 would have the advantage that observations could be made in the J, H or K bands, but would have the disadvantage of a warm slit and a lower efficiency spectrograph.

In either case, custom fore-optics, mount, slit unit, and slit relay optics would need to be made for the on-sky tests, which would not be the same as those used for MOIRCS, since the seeing and plate-scale of the AAT are sufficiently different from those of Suaru.

6.8.2 Subaru tests

Tests could be carried out at Subaru, either after or instead of those at the AAT. These tests would have the advantage that the fore-optics unit would be that proposed for the instrument, and that we could feed MOIRCS itself. A separate slit unit and relay optics would still be required for the prototype tests. These tests would require a longer design phase, since access to the telescope is limited, and many of the interfaces are not currently known.

7 COSTS

(omitted in the public version)

Appendix A Compatibility with Wide Field Imager

ULTIMATE can be made to be compatible with a wide-field GLAO corrected Cassegrain imager, such as that proposed by HIA.

Both instruments could use the same wide-field corrector. This assumes that the image quality achieved by the WFC is sufficient to feed the Starbug IFUs (as for the ULTIMATE WFC), i.e. the WFC cannot rely on the imager to correct any aberrations, if it is also to be used for ULTIMATE.

To enable the same WFC to be employed for both imaging and integral field spectroscopy, none of the ancillary components of ULTIMATE must vignette the beam when ULTIMATE is not in use. The metrology camera is above the WFC located in the shadow of the secondary mirror and will not affect the imager. The Starbug electronics and connector plate can be positioned out of the beam permanently. The bug-catcher must be retractable, such that when ULTIMATE is in use it moves under the field plate to position the Starbugs, and when ULTIMATE is not in use, it houses the Starbugs, and moves out of the beam.

Therefore, the compatibility of ULTIMATE with the wide field imager requires sufficient space between the field plate and the imager to position the Starbugs and bug-catcher, and sufficient space at the Cassegrain focus to locate the electronics and connector plate out of the beam.

Appendix B Feeding PFS

The instrument concept presented in this document assumes that Starbugs feed the nuMOIRCS spectrograph. However, as outlined in the science case (§2) Starbugs could also feed the Prime Focus Spectrographs.

Although details of the instrument design have not been developed, the concept would be much the same as that presented for feeding MOIRCS, differing in details such as the fibre type and the relay optics; the Starbug and IFU components would be very similar.

Note that a galaxy survey which focusses on intermediate redshift galaxies up to redshifts of z ≈ 0.4 could still be a bright time survey, since observations would be at wavelengths red enough to be relatively unaffected by scattered moonlight.

8 DRAFT REVISION HISTORY

Revision	Date	Author	Comments
0.1	11 December	AIS	Initial draft